Exploring Molecule-Metal and Molecule-Topological Insulator Interface at Atomic Scale

A thesis

submitted in partial fulfilment of the requirements
for the degree of Doctor of Philosophy

by

Sk Rejaul
(Reg ID: 20123223)

IISER PUNE

INDIAN INSTITUTE OF SCIENCE EDUCATION AND
RESEARCH, PUNE

CERTIFICATE

Certified that the work incorporated in the thesis entitled ("Exploring Molecule-Metal and Molecule-Topological insulator Interface at Atomic Scale") submitted by **Sk Rejaul** was carried out by the candidate, under my supervision. The work presented here or any part of it has not been included in any other thesis submitted previously for the award of any degree or diploma from any other University or institution.
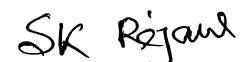
Date: December 21, 2018

(Supervisor)

<u>Declaration</u>

I declare that this written submission represents my research work in my own words and where others' ideas or works have been included, I have adequately cited and referenced the original sources. I also declare that I have adhered to all principles of academic honesty and integrity and have not misrepresented or fabricated or falsified any idea/data/fact/source in my submission. I understand that violation of the above will be cause for disciplinary action by the Institute and can also evoke penal action from the sources which have thus not been properly cited or from whom proper permission has not been taken when needed.

Date:December 21, 2018

(Signature)

Sk Rejaul

Reg. No: 20123223

Abstract

The silicon revolution in 1970s and 1980s made technology accessible to everyone in the form of personal computers. It also propelled the information revolution that connected the world with rapid advances in internet and wireless communication, also known today as the internet of things (IoT). A natural progression in this course was the miniaturization of devices aiming for high speed and low power consumption in all designs. In 1965, Gordon Moore, the co-founder of Intel, said that the number of transistors would double every 18 months, an observation referred to as the "Moore's law". The fabrication and miniaturization in silicon devices has reached the spatial limits calling out for paradigm shifts in designing new technologies. One such candidate on this frontier has been organic molecules. Using them for designing electronic devices, a pathbreaking idea first proposed by Aviram and Ratner in 1974, sowed the seeds of 'molecular electronics'. Since then there have been efforts worldwide to harness the electronic properties of molecules towards this goal.

The advantage of using molecules is their stability, small size, and extensive structural and electronic tunability for desired functionalities. Self-assembled molecules (SAM) supported by a substrate are an excellent platform to explore device functionalities in molecules. However, before converging upon a realistic application, fundamental questions like how do single molecules behave? how do their energy levels align with the substrate, what happens at the interface, how do molecules self-assemble? how does electron transport occur between the molecules and substrate? and so on need, to be addressed. This thesis has attempted to answer some of these questions using Scanning Tunneling Microscopy (STM) and Scanning Tunneling Spectroscopy (STS) at Low Temperature (LT) of 77 K and in Ultra High Vacuum (UHV). The spatial high resolution of STM gives a direct, real space information of the molecules, and the high energy resolution of STS offers a direct probe for their local electronic properties – for their measurement and for their manipulation at the molecular scale.

Metal Phthalocyanine (MPc) molecules have been explored here over noble metal and topological insulator substrates. MPcs are planar π-conjugated systems capable

of self-assembly and can act as versatile, robust, and tunable templates for surface functionalization. Their vast tunability engineered by substituting the central metal ion and the functional groups at the periphery makes them model systems to study the evolution of self-assembly, growth of self-assembled layers, and interface properties over a variety of surfaces.

In the first part of this thesis, adsorption characteristics of copper phthalocyanine (CuPc) and copperoctacyano phthalocyanine ($CuPc(CN)_8$) have been investigated on Au(111) using low-temperature scanning tunneling microscopy (STM) and density functional theory (DFT) calculations. At very low coverage, the adsorption of CuPc and $CuPc(CN)_8$ leads to the formation of one-dimensional chains along the mono atomic (MA) step edge. At higher coverage, both CuPc and $CuPc(CN)_8$, guided by tetramer unit cell formation self-assemble on flat terraces and cross over the step edge of Au(111). CuPc adsorption along the MA step edge shows only one geometric configuration, whereas two different geometric configurations occur for $CuPc(CN)_8$. The spectroscopic signature of these two configurations, probed using STS, manifests in a shift of the peak position of the highest occupied molecular orbital(HOMO) for the $CuPc(CN)_8$ molecule at the MA step edge with respect to the molecule over the flat terrace of Au(111). STM imaging on a flat terrace reveals a tetramer unit cell to be the hallmark of each assembly. The periodicity of herringbone reconstruction of Au(111) is unchanged upon $CuPc(CN)_8$ adsorption, whereas for CuPc adsorption this periodicity changes. STM imaging shows adsorption-induced organizational chirality for both assemblies. STS measurements show an increment in the highest occupied–lowest unoccupied molecular orbital (HOMO–LUMO) gap from CuPc to $CuPc(CN)_8$. For $CuPc(CN)_8$ at LUMO energy, the individual molecule exhibits an orbital-energy-dependent chirality on top of the existing organizational chirality. It remains achiral at HOMO energy and within the HOMO–LUMO gap. No such peculiarity is seen in the CuPc assembly. This energy-selective chiral picture of $CuPc(CN)_8$ is ascribed to the cyano groups that participate in antiparallel dipolar coupling, thereby enhancing intermolecular interaction in the $CuPc(CN)_8$ assembly. The density of state calculations for different molecular orbitals and the STM images simulated with DFT calculations for specific configurations agree with the experimental results. These findings advance our understanding of the role played by the pendant groups of the Pc molecules in step-edge and flat terrace and demonstrate that pendant group substitution is an effective strategy for tweaking intermolecular interactions and for surface functionalization.

In the second part of this thesis, different MPcs (M=Fe,Co,Cu) were investigated on Bi_2Se_3, a topological insulator(TI) substrate, to explore the molecule-TI interface properties using STM and STS. TIs are a new class of materials, insulating in the bulk

but conducting on the surface. The TI surface states exhibit Dirac cone-like dispersion that is protected by time-reversal symmetry due to the strong spin-orbit coupling in these materials. Bare Bi_2Se_3 substrate was well characterized by STM and STS. The MPcs were chosen based on the aim of each investigation and vapor-deposited on Bi_2Se_3. Each MPc resulted in a distinctive finding. For FePc no self-assembled layers were seen on the Bi_2Se_3 substrate. The molecules exhibited two distinct site-specific configurations. In STS measurements there was no shift of the Dirac point either, indicating a weak molecule-substrate interaction. For CuPc no self-assembly could form at a lower coverage. However STS data revealed a change in the Dirac point indicating a charge transfer from CuPc molecule to Bi_2Se_3 substrate. In case of $F_{16}CoPc$ the self-assembly was characterized by nanometer sized rotational domains in a complete monolayer coverage. The highlight of $F_{16}CoPc$ investigation was the STS measurement unveiling a robust signature of negative differential resistance (NDR). $F_{16}CoPc$ deposited on the noble metal Ag(111) substrate showed no spectroscopic signature of NDR, thereby making $F_{16}CoPc/Bi_2Se_3$ interface to be an emergent molecule-TI hybrid interface property. Thus, depending on the central metal ion, the self-assembly, and the local electronic properties at the molecule-TI interface, interface properties take shape and open up avenues for molecular engineering.

To summarize, this thesis has examined some MPcs on different substrates using STM and STS at UHV and LT focusing in detail on their topography, spectroscopy, and local electronic behavior at a single molecule level. The new findings have led to a better molecular scale picture of the influence of pendant groups and of different metals on the adsorption, self-assembly, and electronic properties along with emergent properties specific to molecule-TI hybrid interfaces, thus furthering a microscopic understanding of systems that is indispensable for technological advances.

List of Publications

- Emergent properties of organic molecule-topological insulator hybrid interface: Cu-Phthalocyanine on Bi_2Se_3; **Sk Rejaul**, Imrankhan Mulani, and Aparna Deshpande, *Accepted in Journal of Physical chemistry C (Publication Date (Web): September 19, 2018).*

- Effect of Cyano Substitution on the Step-edge Adsorption of Copper Phthalocyanine on Au(111); **Sk Rejual** SrilathaArra, Barun Dhara, Joel S. Miller, Mukul Kabir, and Aparna Deshpande, *The Journal of Physical Chemistry C* ,122, 11848-11854 (2018).

- Enhancing the Intermolecular Interaction by Cyano Substitution in CuPc; **Sk Rejaul**,, Barun Dhara, Joel S. Miller, Mukul Kabir, and Aparna Deshpande, *The Journal of Physical Chemistry C* , 122, 429-437 (2018).

- Preserving the topological surface state:FePc on Bi_2Se_3; **Sk Rejaul**, Imrankhan Mulani, and Aparna Deshpande, *arXiv:1709.06277 (2017).*

- Enhancing the thermopower and tuning the resistivity in Bi2Se3 with Fe-doping; **Sk Rejaul**, M. Shirolkar, Barun Dhara, Sulabha Kulkarni, and Aparna Deshpande. *Chemical Physics Letters* 638, 94-98 (2015).

- Negative differential resistance in organic molecule-topological insulator hybrid interface; **Sk Rejaul**, Imrankhan Mulani, and Aparna Deshpande, *Manuscript under preparation.*

Acknowledgements

This thesis with its ups and downs would not have been possible without the continuous help and support from some great, intelligent, and perspicacious people throughout five years of my PhD. During these years with the help of these people, as a researcher, I mastered diverse skills including, giving scientific presentations, designing crazy ideas to overcome experiment obstacles, writing scientific papers, and making critical discussions among collaborators. I would like to express my sincere gratitude to all of them.

At the very outset, I would like to start by conveying my deepest regards to my research supervisor Dr. Aparna Deshpande for providing me the opportunity to work in her laboratory, her trust and freedom she gave me for designing experiments. I firmly believe that her inspiring guidance has been a key factor behind a wholesome learning process. More than that she, always used to bring me back from my negativity, and motivate me to aim for achieving noble goals which were much beyond my capability of achieving. During the early phase of my PhD when the laboratory was at its beginning stage, her guidance and confidence made us accomplish our goal even with the very finite resources. It has been a great pleasure to be a part of the journey to make the lab evolve from an empty room to a full-fledged laboratory today.

I wish to thank my research advisory committee (RAC) Dr, Mukul Kabir and Dr. Surjeet Singh from IISER-Pune for their invaluable advice and helpful suggestions to improve my research work at the annual RAC meetings. I take the opportunity to thank our collaborator, Dr. Mukul Kabir and his co-workers Srilatha Arra and Chandan Kumar Singh for all the theoretical calculations to support our experimental results. It was an excellent experience to work with them, and they were beneficial and very quick to respond whenever we needed them. I wish to thank Dr. Surjeet Singh again for allowing me to grow single crystals in his laboratory. I like to thank Dr. Nirmalya Ballav (Department of Chemistry, IISER Pune) for installing the molecular evaporator in the preparation chamber, which was an essential requirement for all experiment in this thesis. It was an excellent opportunity for me to discuss with him about the STM experiment designing and explaining the STM results from the beginning of my PhD.

It was almost impossible to run an experiment smoothly and quickly without the contributions from lab mates. It is my immense pleasure to thank all past and present lab members of Scanning Tunneling Microscopy laboratory. Specially I would like to thank Sadhu Kolekar for sharing his experience of working in ultra-high vacuum laboratory and helping me to build STM tip etching unit. I am grateful to my junior Imran for helping me with each experiment after his arrival at the lab. Soon after

Dedicated to my Father. . .

Contents

List of Figures

List of Abbreviations

1D	**O**ne **D**imension
2D	**T**wo **D**imension
3D	**T**hree **D**imension
STM	**S**canning **T**unneling **M**microscope
LT-STM	**L**ow-**T**emperature **S**canning **T**unneling **M**microscope
STS	**S**canning **T**unneling **S**pectroscopy
Pc	**P**hthalocyanine
MPc	**M**etal **P**hthalocyanine
UHV	**U**ltra **H**igh **V**acuum
MA	**M**ono-**A**tomic
DFT	**D**ensity **F**unctional **T**heory
DOS	**D**ensity **O**f **S**tates
PDOS	**P**rojected **D**ensity **O**f **S**tates
HOMO	**H**ighest **O**ccupied **M**olecular **O**bital
LUMO	**L**owhest **U**noccupied **M**olecular **O**bital
NDR	**N**egative **D**ifferential **R**esistance

Chapter 1

Introduction

1.1   Introduction

The era of silicon-based semiconductor technology started with the invention of the transistor in 1947[1]. Seventy years later we are now surrounded by electronic devices made by using a transistor as a fundamental building block,and we rely on them in our everyday lives. The concept of integrated circuits(ICs) was developed after a decade of the invention of the transistor by integrating more than one transistor on a silicon chip and was experimentally implemented in the instrument by Jack Kilby in 1958[2]. That was the time when the downscaling of electronic device components started. One year later Richard Feynman introduced the concept of "miniaturization" in the field of science and technology in his famous talk "There is plenty of room at the bottom"[3]. In this talk, he also mentioned the idea of "manipulating and controlling things on a smaller scale." The performance of silicon-based devices has improved rapidly by miniaturizing the device components in the last few decades. Intel co-founder Gordon Moore in 1965 predicted that the number of transistors would double every 18 months to improve the device performance, which is known as Moore's law [4]. Precise nanostructuring below 100 nm was successfully achieved using e-beam lithography[5], hard X-ray lithography ($\sim$70nm) [6] and extreme ultra-violet(70-30 nm) [7] to make devices from bulk materials via top down fabrication [6, 8].But fabrication of nanostructures in this method is limited by the wavelength of the incident beam used for making a pattern [6]. The situation is more problematic in the gate region of a field effect transistor (FET) in the current integrated circuit, the gate remains insulated from the current channel but the oxide layer is of thickness 3 nm. The minimum thickness of an oxide layer should be more than 1.2 nm to remain as an insulator otherwise quantum mechanical tunneling will lead to the leakage current [9]. Thus the fabrication and miniaturization of silicon devices have reached the size limits due to the limitation of the lithography technique. The other reason is that at dimensions lower than 10 nm the physics is dominated by quantum effects which can interfere with the desired functioning of the devices. So

the big question is "what are the alternatives for further miniaturization or to replace the silicon-based electronics?"

Recent developments in materials science and engineering have introduced new avenues for future electronics. The enormous research is going on in the following fields either for replacing the silicon-based technology with further improved processing speed or by finding alternative smaller devices which can be scaled down further.

1. 2D electronics: This field got a major boost after the successful isolation of two dimensional (2D) single atomic thick sheet "graphene" from the bulk graphite in 2004 [10] by Andre Geim and Konstantin Novoselov. Later they were awarded Nobel Prize in 2010 for their "groundbreaking experiment". 2D graphene has emerged as the most promising material to replace silicon due to its intrinsic properties like very high electrical and thermal conductivity, mechanical tensile strength, and very high flexibility [11]. Graphene has started the 2D revolution and immediately after that the discovery of silicene, stanene, phosphorene,and transition metal dichalcogenides has attracted a lot of attention for possible technological applications [12, 13].

2. Organic electronics: Organic materials commonly known are insulating in nature due to their large band gap. In 1977, Alan J. Heeger, Alan G. MacDiarmid, and Hideki Shirakawa proved that polyacetylene a pure carbon-based organic material can conduct electricity [14] and they were awarded Nobel prize in 2000 [15]. The first electroluminescence in an organic semiconductor was observed in 1987 [16]. Since then the device fabrication of organic light emitting diode (OLED) [17], organic field effect transistor (OFET) [18] and organic printable solar cells with good enough performance started to be commercialized in new and exciting applications [19]. There are certain advantages of using organic semiconductors over conventional silicon. Organic semiconductors can be soluble and turned into ink which makes printing of electronic circuits possible. Low material production costs, flexibility, ease of synthesis and biocompatibility make organic electronics a desirable choice for certain applications. It is expected that organic electronics market will grow rapidly in coming years.

3. Spintronics: Spintronics is one emerging field which uses the electron's spin as the fundamental unit, and has a great impact in enhancing the efficiency of electronic devices and for upgrading them with additional functionalities [20]. It has emerged in the last two decades with the aim of studying the fundamental aspects of

spin degrees of freedom and offers great diversity of functionalities in device applications [21]. The two orientations up and down of electron's spin provide an additional two binary states similar to the high and low value of the conventional system. In 1988 Albert Fert and Peter Grunberg independently discovered the giant magnetoresistance(GMR) effect,and they were awarded Nobel prize in 2007 [22, 23]. Utilizing this effect the spintronic technology has already developed the information storage devices in the form of hard drive, spin injected field effect transistor [24], and spin torque oscillators[25]. Though this technology is at the early stage of development, it is expected that spin transport electronic devices will be smaller, more versatile, and more robust compared to their silicon counterparts.

4. Molecular electronics: One of the ultimate device miniaturization is expected to be a device made from a single molecule or a device made from an assembly of a few molecules at nanoscale dimension. The branch of nanotechnology which uses a single molecule or a molecular nanostructure to make devices is known as "Molecular Electronics" [26]. Molecular electronics and organic electronics have some common aspects like both use a molecule as a fundamental building block. To clarify, organic electronics refers to bulk applications and its collective response, while molecular-scale electronics refers to nanoscale, single-molecule applications. From the basic science point of view, molecular electronics renders the possibility of investigating the carrier transport properties at the smallest imaginable scale (single molecule) where the physics is mostly dominated by the quantum effects.

There are certain potential advantages of molecular electronics over the others. First, the small features and dimensions, and the variety of electrical and optical properties of the molecule may enable faster device performance, high integration density, and less heat dissipation. Second, molecules possess the unique potential to self-assemble spontaneously and form thermodynamically stable well-defined nanoscale structures via non-covalent interaction which may reduce the production cost. Third, extreme stability and broad tunability of chemical and physical properties via simple chemical synthesis and diversity of chemical structure may lead to the emergence of diverse functionalities which are not accessible using traditional materials. Fourth, the device fabrication with desired size and atomic precision can be done by using a bottom-up approach rather than a cost-effective top-down technique. Electronic devices based on a single molecule or a nanostructure of molecules has the potential to meet the challenge of ultimate downscaling. Moreover, the spin-dependent effects seen in single molecular magnet [27], giant magnetoresistance (GMR) [28], the molecular spin-photovoltaic device [29] can also be realized in metal-organic

molecules for molecular spintronics [30]. Hence, to extend Moore's law beyond the predicted limits, these inherent attributes of molecules described above can be exploited to mould the molecules as fundamental building blocks of the field of molecular electronics as promising candidates for alternative electronics.

Molecular electronics as we understand it today was started at the beginning of 1970s when Kuhn and Bernhard studied the conductivity of cadmium salt fatty acid monolayer [31]. The monolayer was prepared using the Langmuir-Blodgett(LB) technique, and they sandwiched it between two metal electrodes for conductivity measurement. The idea of using a molecule as an electric circuit element was started from this type of experimental results which can be considered as the birth of molecular electronics. The idea of molecular electronics was boosted after Aviram and Ratner published their scheme of constructing "Molecular rectifier" [32] by considering σ-bridge donor-acceptor molecules. In their theoretical analogy, they considered charge-transfer salt by combining the electron-rich tetrathiafulvalene (TTF) molecule and electron-poor tetracyanoquinodimethane (TCNQ) molecule and the first molecular diode was predicted. The monolayer of hexadecyl quinolinium tricyano quinodimethanide was the first experimental system detected as a molecular rectifier in 1990, using as the active molecular monolayer between Mg and Pt electrodes [33] and even between Al electrodes on both sides [34].
The field of molecular electronics went through a rapid growth after the invention of the Scanning Tunneling Microscope (STM) in 1983 by Binnig and Rohrer from IBM lab [35]. It was quickly realized that STM can be used to not only visualize a single molecule on the surface but also to measure the electrical conduction through the molecule. Moreover, it can also be used to study the discrete energy levels of a single molecule and the interface properties when molecules are in contact with a substrate. Joachim, Gimzewski,and coworkers performed the first STM measurement on a single molecule in 1995 [36]. They successfully imaged C60 using STM at room temperature and in ultra-high vacuum. Since then enormous effort has been devoted to using various experimental tools to discover and understand molecules as a functional unit for electronic application. Progress has been already made resulting in organic single molecule magnet [27], giant magnetoresistance in single molecule [28], Coulomb blockade [37], vibronic coupling [38], negative differential resistance [39], and Kondo effect [39–41], single electronic gating [42] using single molecules or molecular thin films.

In case of charge transport, the physical picture of the molecule and semiconductor are identical to each other. The highest occupied molecular orbital (HOMO)

is equivalent to the valence band of the semiconductor while lowest unoccupied molecular orbital (LUMO) is analogous to the conduction band of the semiconductor. Doping effect similar to semiconductors can also be observed in the molecule by substituting electron withdrawing or electron donating groups to tailor the energy levels of molecular orbitals (HOMO and LUMO). Such doping can be engineered in a very controlled way. There is also uncontrolled tailorability which appears when the molecule is placed in between two metal electrodes or over any solid substrate [43, 44] which entirely depends on the molecule and substrate interactions due to the orbital energy mismatch [45], surface dipole formation [46], charge transfer [47] or hybridization with the surface band [42, 48]. Under such interactions, both the individual properties of the molecule and the substrate get modified. Sometimes exciting properties may get destroyed or emerge as interface properties which can also be applied in device application with a detailed understanding [42, 49]. This molecule-substrate interaction along with the intermolecular interaction plays a crucial role in determining the properties and the performance of materials and devices.

Thus to design a molecular device a detailed knowledge about the influence of molecule-substrate interaction, chemical bond formation, charge transfer, geometrical orientation, geometrical structure, energy level alignment, electronic properties of the molecule in contact with a substrate need to be probed systematically. A detailed study of the energy level alignment with the substrate and the molecular HOMO and LUMO is also necessary because the HOMO and LUMO energy orbitals are mainly involved in charge transfer process through the molecule and they get perturbed by the interaction with the substrate after adsorption.

Phthalocyanines are a class of aromatic, macrocyclic molecules, composed of four isoindole units linked with four nitrogen atoms. It has two dimensional geometry and the whole system consists of 18π electrons. A pure organic phthalocyanine without metal was first synthesized in 1907 [50]. Initially due to the excessive tenability in adsorption and emission by the easy modification of the substituent attached at a peripheral ring made phthalocyanines prominently interesting to be used as dyes and pigments [51]. The first metal phthalocyanine (MPc) with copper at its center was prepared in 1927 [52]. A couple of years later several other MPcs with iron and nickel were also reported [52](ref52). Till now there are total 70 MPcs [53]. The inclusion of metal at the center of the phthalocyanine has broadened the application of MPcs into a wide range in photovoltaic [54] organic solar cell [55], a thin film organic light emitting diode [56], single-molecule magnet [27, 57] and several other electronic components [58]. Due to the extreme stability, simple planar structure metal phthalocyanine is seen to be adsorbed flat over the surface where the central

metal and the ligand both take part in interacting with the surface. For such rich adsorption geometry and excessive tunability, metal phthalocyanine is now a model system to study for the interface properties over metal, semiconductor, or topological insulator surface for molecular electronics.

Here we present an extensive study of metal phthalocyanine molecules with three different metals (M=Fe, Co, Cu) at its center and electron withdrawing groups (cyano, fluorine) substituted metal phthalocyanine molecules on noble metal surfaces Au(111), Ag(111) and Bi_2Se_3 topological insulator surface. The effect of molecule-substrate and intermolecular interaction on the structural growth and interfacial electronic properties were probed in each system using the very local STM and STS in UHV at 77 K systematically from single molecule studies to molecular self-assembly exploration. The interplay of these two interactions in case of the electron withdrawing group substitution in a selected position of outer periphery was investigated starting from the single molecule to the one-dimensional chain (1D) and then two-dimensional (2D) assembly. The effect of such substitution in molecular orbitals was also investigated using STS technique. In another system, emergent interface properties of MPc (M=Fe, Co, Cu) molecules with topological insulator Bi_2Se_3 surface were examined when the molecules were deposited over Bi_2Se_3. The adsorption geometry was studied by high-resolution STM images by imaging molecules along with surface Se atoms in background. The interfacial charge transfer, manipulation of topological surface state, symmetry reduction of molecular geometry, and negative differential resistance (NDR) were observed in the STS measurement.

We have advanced the understanding of the structural growth of molecular nanostructures and the changes in the local electronic properties both in the MPc molecules and the substrate. The central metal ion, the ligand, the substituent group, and the underneath surface plays a crucial role to determine the local electronic properties of the interface. The understanding of the charge carrier transport mechanism through the interface is very crucial to any electronic and optoelectronic device made from a single molecule, monolayer, or thin organic film. Thus, the hybridization, charge transfer, and the energy level alignment were understood in detail at the molecular scale to utilize the emerging interface properties for device applications.

1.2   Adsorption of Molecules on Solid Surface

The key parameter which has the most impact over the adsorption geometry and stability of organic molecules on solid surfaces is the molecule-substrate interaction. This interaction determines the emergent properties of the molecule-substrate interface[59]. So a comprehensive understanding of this interaction is essential. Through-
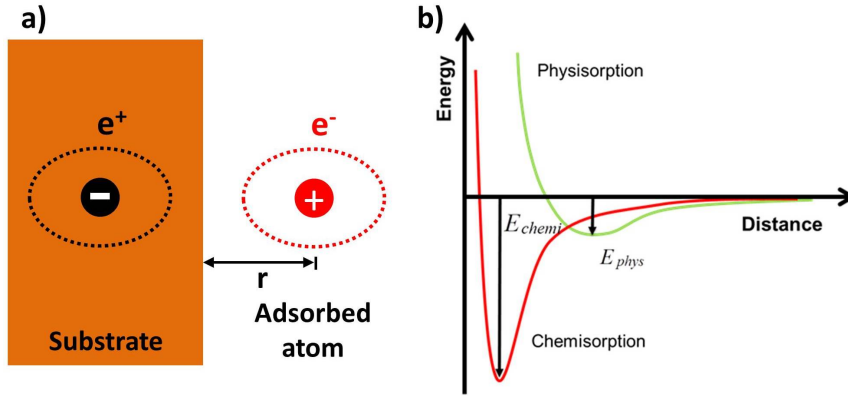
FIGURE 1.1: a) Schematic of image dipole formation in metal due to the positive nucleus and negative charge of electron. b) Potential energy diagram for physisorption and chemisorption. Source reference [60]

out this thesis we have probed this interaction and the intermolecular interaction for molecule-metal and molecule-topological insulator interface. There are several parameters which contribute to the molecule-substrate interaction. Based on the type and strength of the interaction the adsorption process can be divided in two categories *chemisorption* and *physisorption*[59].

Physisorption

In physisorption the interactions involved are very weak. The typical example of physisorption is adsorption of rare gas atoms or closed shell chemically inert molecules. Such adsorption does not involve charge transfer or any chemical bond formation. The interactions are mainly governed by the weak van der Waals interaction which includes the attractive dipole-dipole interaction due to the image dipole formation at the metal surface and London force due to the fluctuating electron inside the molecule.

A schematic of interface dipole formation is represented in Figure 1.1 a. The attractive van-der Waals interaction is due to the dipole-dipole interaction which depends on the distance (r) of the adsorbed atom or molecule from the surface[59].

$$E_{att} \approx -r^{-3} \tag{1.1}$$

Repulsive force due to Pauli exclusion principle at very close distance appears from the interaction of the overlapping filled orbitals. Such repulsion can be written as[59].

$$E_{rep} \approx e^{-cr} \tag{1.2}$$

The combined potential is shown in Figure 1.1 b (green curve). The typical value of binding energy for such interaction is less than 0.3 eV[60]. The electronic structure or orbital energy does not change much in such adsorption.
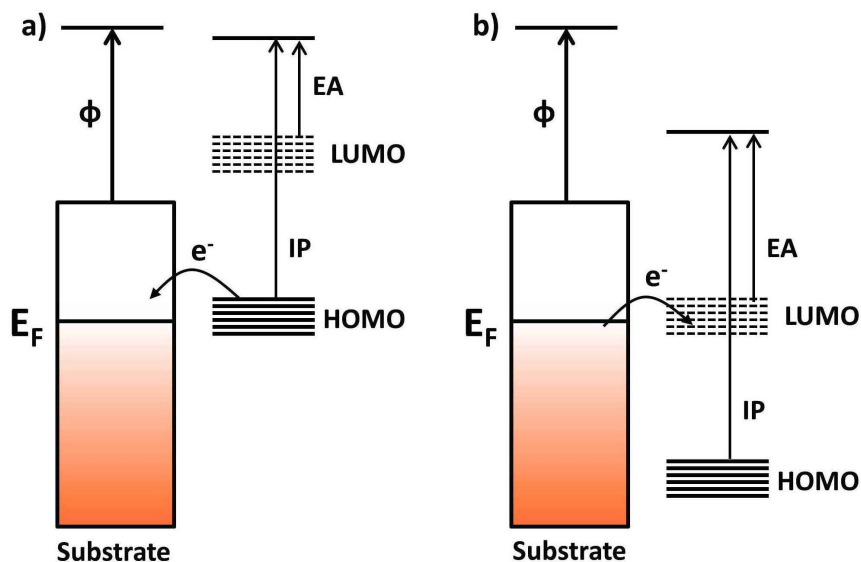
FIGURE 1.2: Schematic of of charge transfer from molecule to the substrate and vice versa is shown. When the HOMO orbital crosses the Fermi level of the substrate electron transfered to the substrate and the reverse transfer happen when LUMO allign with the Fermi level.

Chemisorption

In chemisorption process, the interaction is governed by formation of a strong chemical bond, like metallic, ionic, or covalent[61].The interaction involves direct orbital overlap or charge transfer. Thus it is a strong interaction and the electronic structure and orbital energy get perturbed due to such adsorption. A schematic for charge transfer process is demonstrated in Figure 1.2. Electrons transfer from the molecule to the substrate when the HOMO energy level crosses the Fermi energy of the substrate. The reverse mechanism happens when the LUMO energy level aligns with the Fermi energy. The other type of interaction involved in chemisorption process is orbital overlap or hybridization as described in reference [63]. The interaction between the molecular orbital with s-band and partially filled d-band is considered. The schematic is shown in Figure 1.3. Interaction with the filled s-band gives rise to a shift and broadening in the molecular orbital. Coupling to the partially filled d-band splits the energy level and forms bonding and anti bonding orbital. This type of interaction is very strong [62]. The typical interaction strength is about 1 eV which is much higher than the physisorption value. The potential for chemisorption
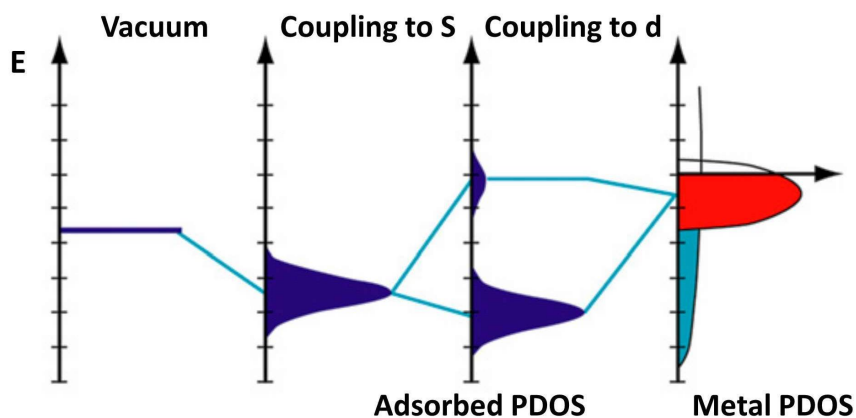
FIGURE 1.3: Schematic of hybridization with the surface band. Hybridization with the broad s-band leads to broadening of the molecular orbital and can shift the orbital. Coupling with sharp d-band induces a split in the energy level and forms bonding and anti-bonding orbital. (Picture adapted from ref [62])

is plotted in Figure 1.1 b. In this adsorption molecules adsorb relatively close to the surface. Another important interaction which has a great impact on formation of self-assembled structures is intermolecular interaction.

1.3 Basic Principle of Molecular Self-assembly

With the detailed knowledge of adsorption process the next logical step is to understand the self-assembly mechanism to gain precise control over designing wide range of molecular nanostructures on the surface[60, 64]. The fabrication technique used for nanostructure growth is bottom-up [65]. In this approach atoms or molecules are deposited over the surface in vacuum to form the nanostructure. The spontaneous assembly of molecules into a stable structure under thermodynamic equilibrium is known as molecular self-assembly [66]. This process involves diffusion of molecules from one adsorption site to another adsorption site on the surface until thermodynamic equilibrium is reached. But if the bond formation over a particular adsorption site is stronger than the diffusion energy the molecule will never achieve equilibrium resulting in an unstable self -organized state. When the molecules are deposited over the surface the two key parameters which decide the kind of growth are flux (F) from the source and the diffusivity (D) of molecules over the surface. To understand the mechanism a schematic illustration is shown in Figure 1.4. If the D/F ratio is very low then the molecules do not get enough time to diffuse to the thermodynamic equilibrium and they form a metastable self organized structure. If the D/F ratio is high enough the molecules can diffuse to the equilibrium site against the bond strength at

a particular site. Then the molecules form a spontaneous self-assembled structure. Diffusivity(D) can be enhanced by increasing the temperature of the substrate. The
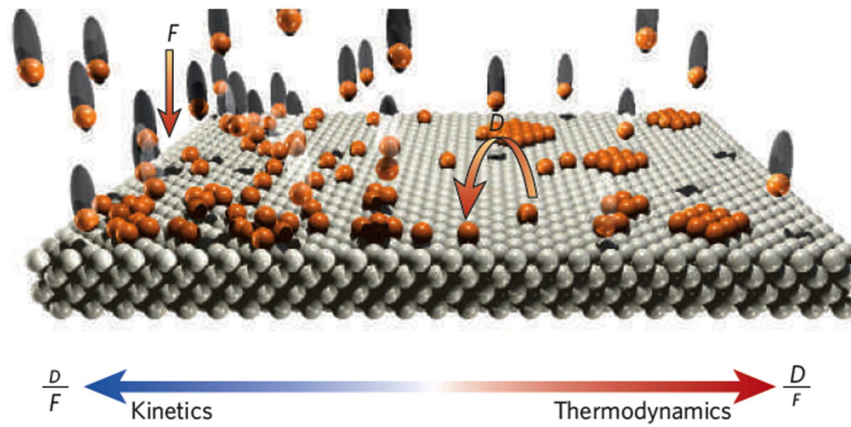
FIGURE 1.4: Schematic illustrating for self-organisation and self-assembly growth (adapted from [64]). Selforganised structures or self-assembled structures depend on the relative strength of flux(F) of incoming molecules and the diffusivity(D) of the molecules on the surface. Metastable selforganised structures form when D/F is low (toward left). When D/F is high, selfassembled structures at the thermodynamic equilibrium are formed (toward right).

thermal energy is transferred to the molecule which increases the kinetic energy(E_k) to overcome the diffusion potential barrier(E_d). There is a certain limit for increasing the substrate temperature, the kinetic energy should not cross the binding(E_b) energy otherwise the molecules may get desorbed from the surface. In order to get an ordered equilibrium structure intermolecular interaction energy(E_{inter}) should be comparable to the kinetic energy. If it is very strong then molecules will get attached to each other strongly and the system will not reach the equilibrium. So the energy order for self-assembly is

$$E_b > E_{inter} \geq E_k > E_d$$

A system should follow this energy order to get a self-assembled molecular nanostructure.

So the self-assembled monolayer or thin film growth depends critically on the strength of two interactions molecule-surface and the intermolecular interactions. Depending on the strength of these two interactions the principle growth modes are distinguished into three categories.

(a)**Frank–van der Merwe(FM)** growth refers to the case when the molecule-surface interaction is stronger than the intermolecular interaction and molecule are more

strongly bound to the surface than with each other. The molecules first cover the surface prior to growth of a second layer.

(b)**Volmer–Weber (VW)** growth refers to the case when the intermolecular interaction is much stronger than the molecule-surface interaction. This means molecules like to stick together rather than binding strongly with the surface. In this case, molecules form three dimensional cluster or island.

(c)**Stranski-Krastanov (SK)** growth refers to the intermediate case of FM and VW where the molecule-substrate and intermolecular interaction strength are comparable. Both two-dimensional layers and three-dimensional islands characterize the growth in this process. The transition from the FM to VW growth occurs at a critical layer thickness which is strongly dependent on the chemical and physical properties, such as surface energies and lattice mismatch between substrate and film.

1.4   Outline of The Thesis

The aim of this thesis was to understand the effect of electron withdrawing group substitution in structural growth and electronic properties of metal phthalocyanine molecule by using the local STM and STS probe. The study presents a detailed investigation on structural growth and electronic properties of cyano (CN) functional group substituted and unsubstituted CuPc molecule on Au(111). The second goal of this thesis was to investigate for the interface properties of three MPc (M=Fe, Co, Cu) molecules on topological insulator surface from single molecule to assembly. This part mainly focused on the surface functionalization by on-surface molecular doping to tune the energetic position of Dirac point and to explore the resulting emergent properties due to hybridization with the surface.

This thesis is organized as follows: the first chapter describes the motivation behind investigating molecules on surface and the adsorption kinetics of atoms or molecules over atomically clean surface. Rest of chapters report following

Chapter 2 discusses the theoretical background starting from 1D step potential model to 3D Tersoff and Hamann model of scanning tunneling microscopy. The operational mode for STM imaging and STS data acquisition method using lock in amplifier are also described. Different parts of sample preparation chamber and actual ultra-high vacuum(UHV) low temperature STM system also are described using schematic diagrams. Atomically cleaned substrate preparation and their basic characteristics also reported in this chapter.

Chapter 3 reports a comparative study of the site-specific and orientation selective adsorption of CuPc and CN-functionalized $CuPc(CN)_8$ at the mono-atomic (MA) step of the Au(111) substrate carried out using low-temperature scanning tunneling microscopy (LT-STM) at 77 K. Based on the experimental observation $CuPc(CN)_8$ forms 1D chains along the step edge. STS measurements probe the orbital energy levels mainly HOMO and LUMO.

Chapter 4 presents the extended experimental results for the same system in chapter 3. Here 2D assembly of both CuPc and $CuPc(CN)_8$ on Au(111) were investigated using STM and STS at 77 K. STS measurements on the 2D assembly of $CuPc(CN)_8$ show energy specific chirality at the LUMO energy. An energy independent organizational chirality was reported for both the molecules.

Chapter 5 first introduces the topological insulator material and the Bi_2Se_3 crystal structure that was used as the substrate. Different adsorption sites and the structural changes due to the molecule-substrate interaction for FePc and CuPc were demonstrated. The tuning of Dirac surface state was reported due to the on-surface molecular doping. STS measurement was also reported for HOMO and LUMO for both the molecules.

Chapter 6 is about an extensive study of self-assembly of $F_{16}CoPc$ on Bi_2Se_3 and Ag(111) substrate was reported. In STS measurement, negative differential resistance (NDR) was observed for $F_{16}CoPc$ on Bi_2Se_3 whereas no NDR was observed on Ag(111). NDR mechanism was explained using the concept of resonant tunneling between the specific molecular orbitals and the substrate. Speculations were made for the NDR observations for $F_{16}CoPc$ on Bi_2Se_3

Chapter 7 concludes this thesis with a summary and an outlook for future work.

Chapter 2

Experimental Setup and Methods

This chapter provides a brief introduction to the scanning tunneling microscopy (STM) principle, experimental setup, and the methods used for sample preparation and data acquisition. In particular, the general working, data , and theoretical insight are discussed in section 2.1.2 then the low temperature scannign tunneling microscope (LT-STM) used for the imaging and spectroscopy is introduced in section 2.2. A detailed description of the ultra high vacuum (UHV) sample preparation chamber and molecular evaporator is given in section 2.3. In section 2.4 we have discussed the sample preparation methods and measurement techniques in detail. The computational details for density functional theory calculations(DFT) are given in section 2.5. The sample preparation and measurements were performed in two ultra high vacuum chambers(UHV) with a base pressure $< 10^{-10}$ mB. Among the two UHV chambers, one contains the main instrument used to acquire data, low temperature scanning tunneling microscope(LT-STM) and the other one contains the equipments for sample preparation . These two chambers are connected via a gate valve. After sample preparation the sample can be directly transfered to the STM chamber for the LT-STM measurement.

2.1 Scanning Tunneling Microscopy and Spectroscopy

Feynman's dream of "manipulating things at a smaller scale" as he mentioned in his talk "There is plenty of room at the bottom" [67] was realized after the invention of Scanning Tunneling Microscope(STM) by Binnig and Rohrer at IBM lab in 1982 [68]. The creation of STM was the major breakthrough not only in the field of surface science to image the atoms on a metal or a semiconductor surface but also to make nanostructures using bottom up approach from the single atoms or molecules with the STM tip based manipulation techniques, and probe their electronic properties using the very local spectroscopic technique to build nanoscale devices. The STM is based on the principle of quantum mechanical tunneling effect. In this effect a particle can tunnel from one metal electrode to another metal electrode if the electrodes

are placed very closed to each other so that the gap is < 10 Å. The whole system is actually a metal-vacuum-metal junction where the a potential barrier is formed due to the difference in work function of the two sides. The wave function of an electron decays exponentially in vacuum, so does the tunneling current. To record an STM image a very sharp metallic tip is scanned over the surface(operating principle is discussed in section 2.1.2) using a piezoelectric scanner. The first STM image of Si(7 × 7) reconstruction was reported by Binnig et al. in 1983 [69]. Apart from imaging the conducting and semiconducting surfaces, organic/inorganic molecules were also imaged using STM by depositing them over metallic substrates [70–72]. In comparison with other technique like x-ray diffraction(XRD) and low energy electron diffraction(LEED) STM provides a real space image. Scanning electron microscope(SEM) also provide a real space image but the resolution of SEM is limited by the incident electron beam diameter and cannot resolve atoms or molecules. STM also probes the electronic properties of the surface and the adsorbate. The probe technique is very local and highly energy sensitive. The first scanning tunneling spectroscopy of a single molecule was reported in 1993 on C_{60} [73] and ethylene[74] by measuring differential conductance. STS can probe the surface states [75], surface potential [76, 77], the Kondo effect[78], Dirac cone like dispersion in graphene [79] and topological insulator[80] , molecular HOMO-LUMO [81] and the vibrational evergy levels[82] as well as electron spin[83]. The spin-polarized STM can also probe the surface magnetic properties[84].

Several advances in surface science [85], materials science, and physics[86] has established without a doubt that the STM is a very powerful tool to investigate the topography and the local electronic properties with atomic scale precision. It is a very unique technique which provides the structural properties and the corresponding electronic properties around the Fermi energy of the surface and adsorbate on the surface.

2.1.1   Theory of Scanning Tunneling Microscopy and Spectroscopy

Here we will discuss the basics of STM. The fundamental principle of STM is the quantum mechanical tunneling of electrons through a thin vacuum barrier. There are several theoretical models to explain this tunneling effect. For ease of understanding we consider in the following the simple one dimensional(1D) model to understand the key mechanism behind the very high special resolution in STM imaging. Then we will discuss the second model by including the three dimensional (3D) structure and the electronic structure of the tip.
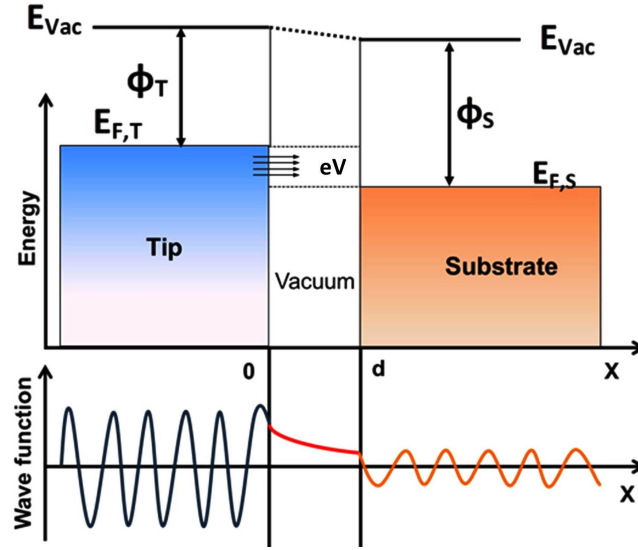
FIGURE 2.1: Schematic energy level diagram of a 1D of tip(metal)-vacuum-sample(metal) tunnel junction where d is the vacuum barrier width and V is the bias applied between tip and sample. $E_{F,T}$ and $E_{F,S}$ are the Fermi energy of the tip and the sample. E_{Vac} is the vacuum energy level. Φ_T and Φ_S are the work function of tip and sample respectively.

One dimensional model

In the 1D model the STM tunnel junction(tip-vacuum-sample) is considered as a finite step potential(as shown in Figure 2.1) for an electron with energy E < V_0, where V_0 is the potential barrier height formed due to the different work function on two sides.

$$V(x) = \begin{cases} 0, \text{ for x} \notin \text{[0,d]}, \\ V_0, \text{for x} \in \text{[0,d]} \end{cases} \quad (2.1)$$

The 1D Schrodinger stationary equation for an electron in such step potential is

$$[-\frac{\hbar^2}{2m}\frac{\partial^2}{\partial x^2} + V(x)]\Psi = E\Psi \quad (2.2)$$

where $\hbar$ is the plank constant devided by 2π and $\Psi(x)$ is the electron wave function. Solutions of equation 2.2 are

$$\Psi(x) = \begin{cases} e^{\pm iKx}, if\, x \notin [0,d] \\ e^{\pm kx}, if\, x \in [0,d] \end{cases} \quad (2.3)$$

where

$$K = \sqrt{\frac{2m(V_0 - E)}{\hbar^2}} \quad (2.4)$$

and

$$k = \sqrt{\frac{2mE}{\hbar^2}} \tag{2.5}$$

Using the boundary condition at the different regions of the finite step potential one can obtain the coefficient of solution in equation 2.3 [87]

The Transmission coefficient can be determined by calculating the ratio of the transmitted wave amplitude and the incident wave amplitude which is given as

$$T = \frac{1}{1 + \frac{(K^2 + k^2)^2 Sinh^2(kd)}{4K^2 k^2}} \tag{2.6}$$

For $V_0 \gg E$ means for a very high potential barrier kd»1, so the transmission coefficient bacomes

$$T \approx \frac{16K^2 k^2}{(K^2 + k^2)^2} \times e^{-2kd} \tag{2.7}$$

The transmission coefficient T is exponentially dependent on the barrier width(d). Now the tunneling current is directly proportional to the T which implies that the tunneling current (I) also depends exponentially on the barrier width(d)

$$I \approx T \approx e^{-2kd} \tag{2.8}$$

This exponetial dependence of tunneling current is the key meachnism of STM and provide a high spatial resolution, as a small change in d implies a huge change in I.

Tersoff-Hamann model

A more realistic model for metal-insulator-metal in three dimension was developed by Bardeen in 1961,[88] long before the invention of STM. He considered the weak coupling between two metal electrodes and solved the time dependent first order perturbation theory. Later in 1983 Tersoff and Hamann extended the Bardeen model to make it more realistic to the actual STM tunnel junction by considering the electronic structure of both the tip and sample [89, 90]. In this model the overlap of electronic wave of tip (Ψ_μ) and the tunneling matrix $M_{\mu,\nu}$ was described by the sample (Ψ_ν which was introduced by Bardeen[88] Using the Fermi distribution function and if E_μ and E_ν are the corresponding energy eigenvalues respectively then the tunneling can be written as

$$I = \frac{2\pi e}{\hbar} \sum_{\mu,\nu} f(E_\mu)[1 - f(E_\nu + eV)]|M_{\mu,\nu}|^2 \delta(E_\mu - E_\nu) \tag{2.9}$$

where $M_{\mu,\nu}$ was calculated by Bardeen [88]

$$M_{\mu,\nu} = -\frac{\hbar^2}{2m}\int(\Psi_\mu^*\nabla\Psi_\nu - \Psi_\nu\nabla\Psi_\mu^*)dS \tag{2.10}$$

In case of $V_0 \gg eV$ which means a very low applied bias and at low temperature the Fermi distribution function can be treated as a step function, f(E)=1, then the expression for tunneling current becomes as follow (see ref[90] for details of approximation)

$$I = \frac{2\pi e^2}{\hbar}V\sum_{\mu,\nu}|M_{\mu,\nu}|^2\delta(E_\mu - E_F)\delta(E_\nu - E_F) \tag{2.11}$$

Now considering the tip wave function as a spherical s-wave, and at low temperature and finite bias the tunneling current can be written as

$$I \approx \int_{E_F}^{E_F=eV}\rho_t(E - eV)\rho_s(E)T(d, eV, E)dE \tag{2.12}$$

where T(d, eV, E) includes the dependence of barrier width d. The local density of states of the tip and the sample were defined as:

$$\rho_t(E) = \frac{1}{V}\sum_\mu\delta(E_\mu - E) \tag{2.13}$$

and

$$\rho_s(E, r_0) = \sum_\nu|\Psi_\nu(r_0)|^2\delta(E_\mu - E) \tag{2.14}$$

Mainly there are total three factors which contribute to the tunneling current- the local density of states of the tip, sample and the transmission coefficient. So the STM image is not only a measure of the roughness of the surface along the z direction. It actually the outcome of the combination of both the topography and the density of states of the sample.

Now at very low applied bias ρ_t and T remain constant. The first derivative of the tunneling current in 2.12 can be written as

$$\frac{dI}{dV} \approx \rho_t(E_F)\rho_s(E_F + eV)T(d, eV, E_F + eV) \tag{2.15}$$

It can be easily identified that for a constant density of states of the tip the first derivative of tunneling current is directily proportional to the local density of the sample.

$$\frac{dI}{dV} \approx \textbf{LDOS of Sample}$$

Lock-in Technique

To measured the dI/dV signal we have used the standard lock-in amplifier. In this technique a small sinusoidal voltage was superimposed with the DC applied bias. As the tunneling current is a function of applied bias this superimposed signal also causes a sinusoidal modulation in the tunneling current. The amplitude of the modulation is very sensitive to the change in the slope of the tunneling current with bias voltage. So for a small sinusoidal modulation the applied bias becomes

$$V = V_b + V_{mod} sin\omega t$$

The Taylor expansion of the modulated current is

$$I(V_b + V_{mod}sin\omega t) \sim I(V_b) + \frac{dI(V_b)}{dV}V_{mod}sin\omega t + \frac{d^2I(V_b)}{dV^2}V_{mod}^2 sin^2\omega t + \cdots\cdots$$

The coefficient of the second term is the first derivative of the tunneling current. Now by using lock-in amplifier one can easily measure the first harmonic which probes the local density of states of the sample. Similarly the coefficient of second harmonic is the measure of d^2I/dV^2 which can be a measure of the vibrational energy levels. There are two basic tunneling processes for electrons to transport from the tip to the sample and vice-versa. One is elastic tunneling, in this process electron tunnel without any energy loss. It reflects an intense peak in dI/dV. The other one is inelastic tunneling, which involves electron's energy loss. In case of a molecule in between the tip and the substrate, electrons injected into the molecule may lose their energy by exciting the vibrational mode level before tunneling into the surface. These modes can be detected as an extra small peak in dI/dV curve. The intensity of such peak is minimal and can be identified in the d^2I/dV^2 curve.

2.1.2   Operating principle

As discussed earlier the main part of a STM is the metal-vacuum- metal quantum mechanical tunnel junction where two metals represent the tip and the sample. A schematic to understand the basic working principle is shown in Figure 2.2. To achieve very high spatial resolution of Å order a very sharp tip which has approximately a single atom at its end is used to scan the sample. Such high spatial resolution can only be achieved if the tunneling occurs through a single atom. The STM tunnel junction is shown in the red square in Figure 2.2. The STM image is acquired by applying a DC bias between the atomically sharp tip and sample. Then the tip moves laterally in xy plane by a piezoelectric scanner simultaneously detecting the variation

in the tunneling current. A feedback loop is in place to maintain the tip height. STM
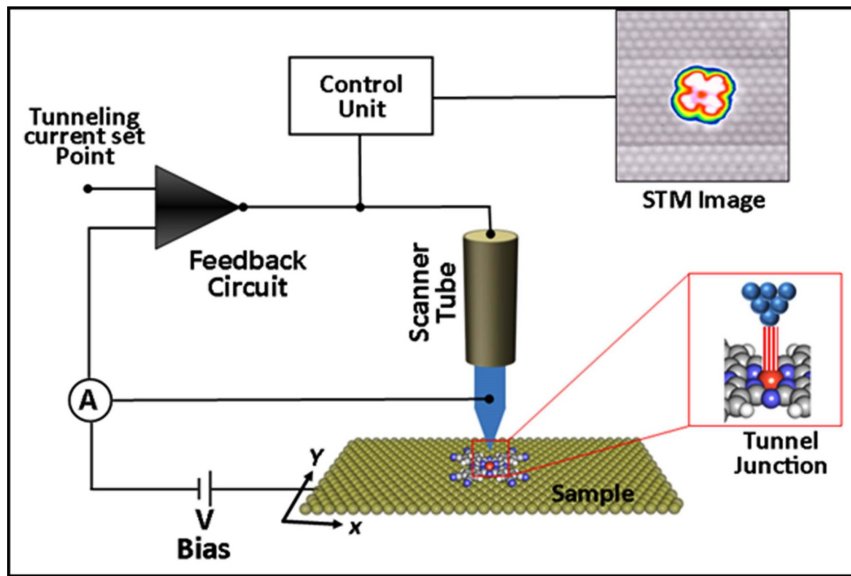
FIGURE 2.2: Operation principle of STM. A DC bias is applied be-
tween tip and sample, feedback loop is used to maintain the barrier
width in the tunnel junction. The tip can be moved in x,y and z direc-
tion by the piezoelectric scanner.

topographic image can be recorded in two basic operational modes, constant height
mode and constant current mode as shown in Figure 2.3. In constant height mode
STM tip scan the conducting surface by maintaining a constant height within tunnel-
ing range. Therefore plotting the change in the tunneling current in the xy plane give
the real space topographic image. The main disadvantage of performing experiment
in this mode is that if the surface roughness is more than the fixed gap between the
tip and surface then tip will crash against the surface. The tip needs to be very stable
in z direction against the thermal noise and external mechanical vibration. The other
operation mode which is the mostly used mode for STM imaging is the constant
current mode. In this case a feedback loop is used to maintain the constant current
by moving the tip up and down in z direction. Which means effectively varying the
barrier width. The real space STM image in this mode is recorded by plotting the
variation in the height with respect to the lateral displacement during scanning. The
advantage of this mode is that the tip follows the surface and there is no chance of tip
crashing over the surface as the feedback loop is there to ensure the stability. Con-
stant current mode is most commonly used mode for STM study. In this thesis we
have used the same operation mode and only during spectroscopy the feedback loop
was turned off.

Figure 2.4 represents the energy level diagram of the tunnel junction and electron
tunneling mechanism under applied bias. When the tip and sample are far away there
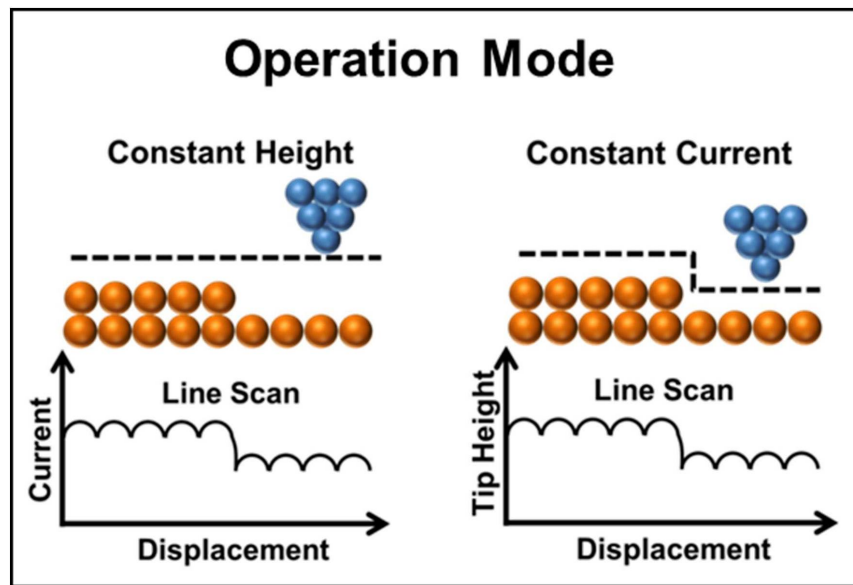
FIGURE 2.3: Two basic operational modes of a STM, constant height and constant current mode.
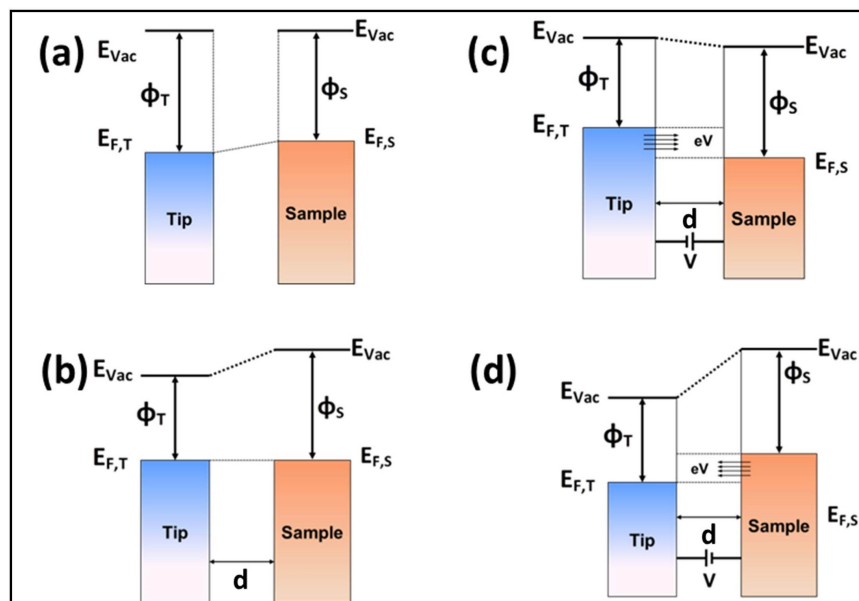
FIGURE 2.4: Schematic energy level diagram of STM tunnel junction under applied bias. a) tip is far away from the sample, no tunneling. b) Tip is in the tunneling range random tunneling between tip and sample, no net tunneling current.c) Positive applied bias, electron tunneling from tip to the sample. d) negative applied bias electron tunneling from sample to the tip.

is no effective tunneling as shown in Figure 2.4 a. Figure 2.4 b represent the energy level alignment when tip and sample are in tunneling range. The random tunneling between tip and sample starts and there will not be any net tunneling current. To have a net tunneling current a bias is applied between tip and the sample. When a positive bias is applied to the sample as shown in Figure 2.4 c, electron starts to tunnel from tip to the sample and the tunneling current actually probes the unoccupied states in the sample, which is the conduction band. Alternatively, when negative bias is applied to the sample, the electron tunnels from the sample to the tip and probes the valence band of the sample. In this explanation the density of states of the tip is considered to be constant. This is typically realized by using a metallic tip.

2.2 Low Temperature Scanning Tunneling Microscope

All the work reported in this thesis has been done by LT-STM manufactured by Omicron (now ScientaOmicron) Nanotechnology. In this system STM measurement can be done at three different operating temperatures liquid helium (LHe) temperature (4.2 K), liquid nitrogen(LN_2) temperature (77 K), and room temperature (300 K). The entire system is shown in Figure 2.5. There are two parts of the system- left side is the main LT-STM chamber for performing the measurements while all the procedures regarding substrate preparation and molecule deposition were done in the preparation chamber -right side. The cooling occurs by thermal contact using a bath cryostat and it allows a simultaneous cooling of both the STM tip and the sample. This means the tip and the sample remain at the same temperature during measurement lowering the thermal noise which is very important for spectroscopy measurement. Very low temperature of the tip is very useful for obtaining stable STM images as the thermal diffusion of the apex atom is minimized at low temperature. The average time that the system can be at 77K with one filling of liquid nitrogen(LN_2) is about 60 hrs which aids in performing long term experiments without any interruption.

To have a clear picture of the LT-STM, the schematic design of the same is shown in Figure 2.6 a. The cryostat as shown in Figure 2.5 consists of two concentric dewars. The outer one is for LN_2 and inner one for LN_2/LHe filling. The inlet of liquid and the gas outlet are shown in the inset of Figure 2.6 a along with the LHe sensor. The STM is placed at the base of this cryostat and is in direct contact with the inner LHe dewar. If inner dewar is filled with LHe than the STM will be at 4.2 K. But if both the inner and outer dewar are filled with LN_2 then the STM will be at 77 K. A low temperature sensor is placed at the STM stage to measure the temperature. The position of STM is marked with red rectangle in Figure 2.6 a. The STM tip and
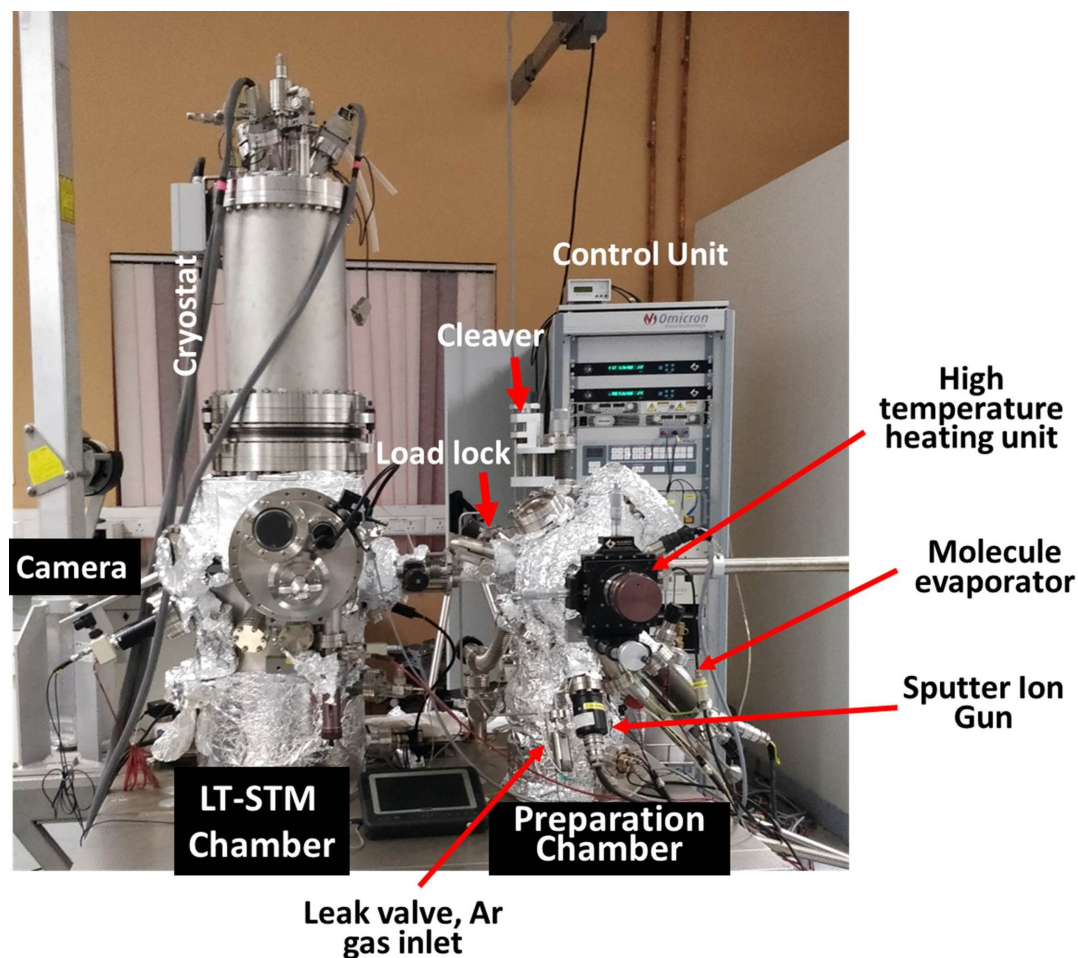
FIGURE 2.5: Picture of UHV LT-STM(letf side) and the preparation
chamber(right side)

sample can be viewed on the screen from outside using a CCD camera by focusing
through one of the view ports. The actual STM is shown in Figure 2.6 b. The whole
STM stage can be moved up and down using the knob at the top of the cryostat. The
stage is raised up and made to be in direct contact with the LHe dewar for cooling.
During tunneling measurement the stage is released to hang freely via three springs
to isolate from the external vibration. The LT-STM specially the tip and sample unit
further illustrated in Figure 2.7. The sample stage is held by three suspension spring
(6,7 and one(8) in the back). The whole stage is held in such a way that it can hang
freely without making any contact with LHe dewar and the side wall to minimize
the mechanical vibrations and also to reduce the thermal loss due to any contact with
the room temperature. The noise is further reduced by the eddy current damping
unit(marked by (1) in Figure 2.7 a. The Scanner(2), tip holder reception(3), Sample
holder (4) unit are marked. The sample is facing down with tip approaching from the
bottom. Figure 2.7 b represent the STM sample plate. The maximum scanning area
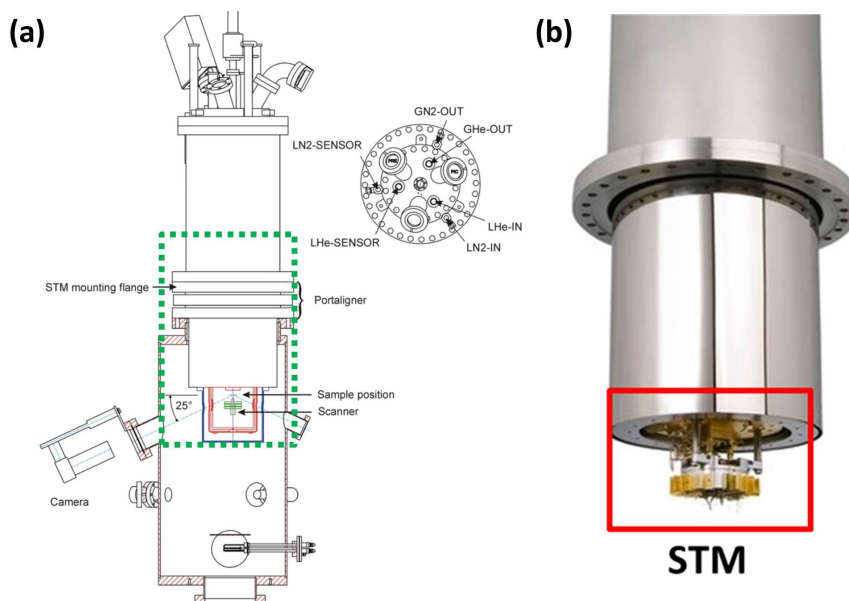
FIGURE 2.6: a) schematic design of LT-STM chamber and location of STM inside the chamber. b) Picture of actual STM at the base of cryostat marked by red rectangle. Picture source Omicron manual.
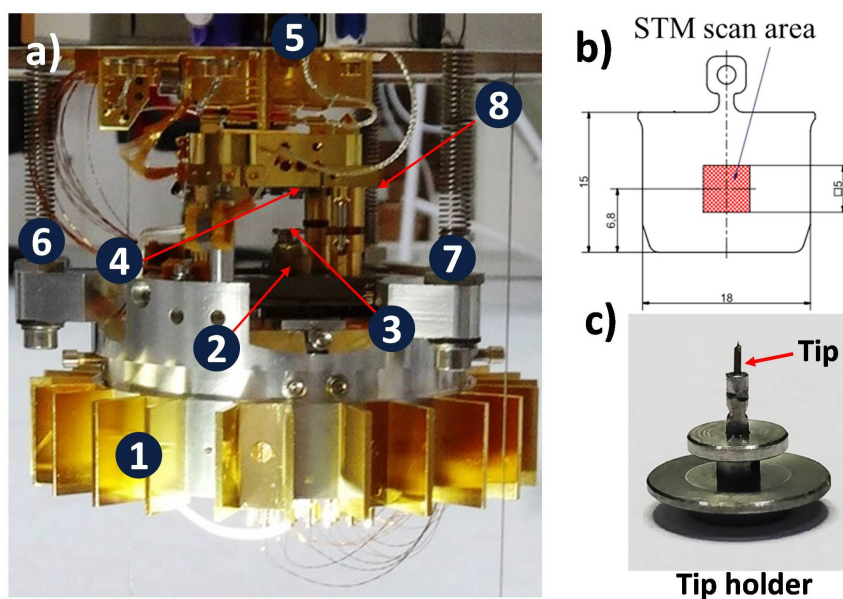
FIGURE 2.7: a) Actual picture of LT-STM, STM is hanging from the LHe cryostat by three springs (marked as 6,7,and 8) . (1) Eddy current damping. (2) Scanner. (3) tip holder reception. (4) Sample holder. Tip approaches from bottom to the sample surface. b) Picture of a STM sample plate and the scan area is marked with red square. c) Picture of a tip holder while a tip is loaded and marked by red arrow. The tip holder rests on top of the scanner during scanning, marked by (3) in (a).

is marked with a red square. Actual picture of a tip holder along with a tungsten tip is shown on 2.7 c. Prior to STM data collections this whole set up was placed very carefully over the scanner.

2.3   Preparation Chamber and Molecule Evaporator

The preparation chamber shown in Figure 2.5 has a base pressure of the order 10^{-10} mB. The available equipments for substrate preparation in the preparation chamber are (i) high temperature heating unit with two type of heating methods- resistive and direct,(ii) Ar^+ ion sputtering ,(iii) in-situ crystal cleaver and (iv) molecule evaporator. The highest temperature achievable for resistive and direct heating are $1000°$ C and $1600°$ C respectively. The in-situ crystal cleaver can be used to cleave single crystals in UHV to avoid contamination. The molecule evaporator attached to the preparation chamber is shown in Figure 2.8 a. The length of the evaporator can be adjusted to vary the distance from the source to the substrate. Three crucibles are housed in the evaporator. Three different molecules can be loaded at time and heated separately. It also has water or LN_2 cooling facility.

FIGURE 2.8: a) Actual picture of the molecule evaporator. b) Inside view of the crucibles. Three crucibles are marked with red arrow. They are thermally isolated from each other.

2.4   Sample Preparation Methods

The sample preparation for investigating MPcs(M= Fe,Cu,Co) is a two-step process. The first step to achieve highly reproducible sample is to start from preparing a flat and atomically clean substrate and check the surface with STM to ensure that there are no obscure impurities left to disturb the adsorption process over the surface. The second step is depositing MPc molecules over the clean substrate in a very controlled way to observe individual molecules or self-assembly. Two noble metal substrates Au(111), Ag(111), and one topological insulator Bi_2Se_3 were used to investigate MPcs(M= Fe,Cu,Co).

2.4.1 Metallic Au(111) substrate

The substrate used to investigate CuPc and $CuPc(CN)_8$ in chapter 3 and chapter 4 is Au(111). 300 nm thick Au thin film on mica was purchased from Sigma Aldrich. A 5mm × 5mm size film then mounted on a STM plate by spot welding two small tantalum foil. After inserting the sample in UHV in the preparation chamber, the Au(111) surface was prepared by subsequent Ar+ ion sputtering annealing cycles with 1 KeV beam voltage, current 1 μA and annealing at 750 K. The surface quality was checked by STM at 77 K. The atomically clean Au(111) surface showed herringbone reconstructions and atomic resolution in the STM images as shown in Figure 2.9 a and b. The atomic resolution image in Figure 2.9 b revealed hexagonal lattice
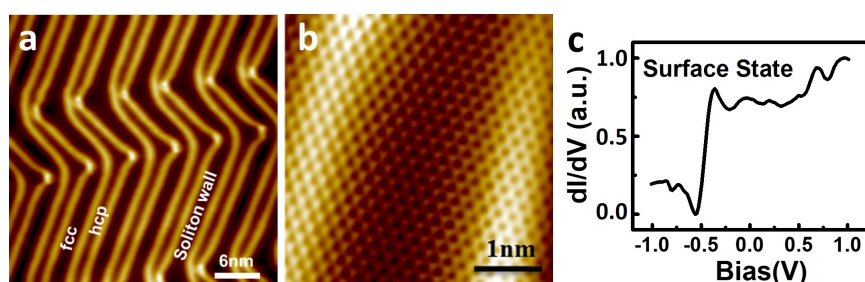
FIGURE 2.9: a) Cleaned Au(111) surface showing herringbone reconstruction. b) Atomically resolved Au(111) surface. (c) STS measurement on Au(111) showing Shockley-type surface state at -0.5 V . Imaging condition: V=0.6 V, I= 1 nA

with lattice parameter of 2.84 Å . The surface electronic property further characterized by a Shockley-type surface state at -0.5 V as shown in Figure 2.9 c. Such a surface state is unique for each metal surface [91].

2.4.2 Metallic Ag(111) substrate

In the experiment described in Chapter 6 the substrate used to investigate is Ag(111). First 500 nm thick Ag thin film was prepared on mica using standard sputter coating technique. Thin film was then placed at the center of the STM sample plate by spot welding technique. Similar to Au(111), before any deposition the Ag(111) surface was prepared by subsequent Ar+ ion sputtering annealing cycles with 1 keV beam voltage, current 1-1.2 μA and annealing at 800 K. The constant current STM image at 77 K is shown in Figure 2.10 a where clear atomic steps are visible. The atomic resolution STM image shown in Figure 2.10 b revealed the hexagonal arrangement of atoms on the surface with lattice constant of 2.88 å . The Shockley-type surface state was observed at -0.065 V as shown in Figure 2.10 c.
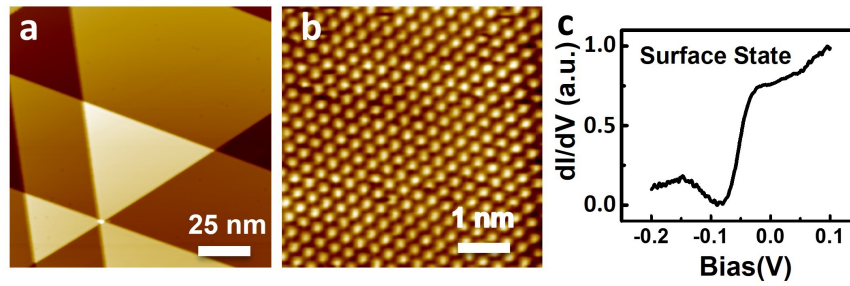
FIGURE 2.10: a) Clean Ag(111) surface showing nice triangular island and atomic step. b) Atomically resolved Ag(111) surface. (c) STS measurement on Au(111) showing Shockley-type surface state at -0.065 V. Imaging condition: V=0.5 V, I= 0.8 nA.

2.4.3 Bi_2Se_3 topological insulator substrate
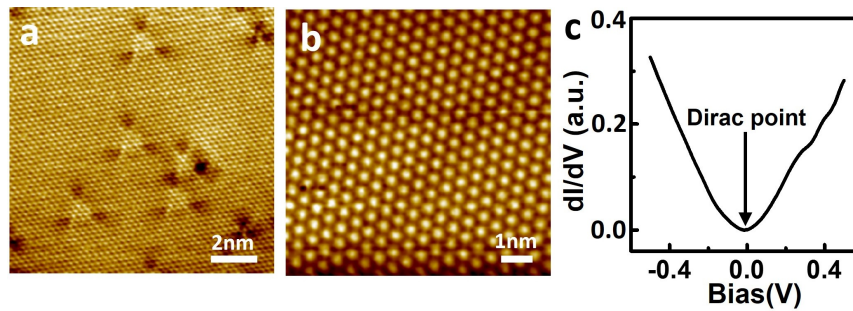
FIGURE 2.11: a) Cleaved Bi_2Se_3 surface showing nice triangular Se vacancy defects . b) Atomically resolved $Bi_2Se_3(111)$ surface showing hexagonal arrangement of Se atoms. (c) STS measurement on the surface showing Dirac cone like surface state at the Fermi energy. Imaging condition: V=0.6 V, I= 0.4 nA.

The Bi_2Se_3 single crystal was prepared by flux method (see appendix). The layered structure of the crystal (as explained in chapter 5) make it easy to cleave it in UHV. The atomically clean substrate can be made just by in-situ cleaving of the crystal. To cleave the sample we have used the crystal cleaver installed in the preparation chamber. Figure 2.11 a represents the constant current STM image of in-situ cleaved $Bi_2Se_3(111)$ surface where triangular defects due to the Se vacancies are key signatures of Se surface [92]. Zoomed in atomically resolved STM image in Figure 2.11 b reveals the similar hexagonal pattern of Se atoms like other (111) surface. STS measurement shows the Dirac cone like surface state similar to graphene in the bulk gap between conduction and valence band [80, 93].

2.4.4 Molecule deposition over the substrate

CuPc(CN)$_8$ and CuPc molecules were investigated on Au(111) in chapter 3 and 4. In all experiment in this thesis for evaporation of molecules we have used the evaporator mentioned earlier in section 2.3. CuPc(CN)$_8$ was synthesized by a method in the literature [94] and was evaporated from a resistively heated quartz crucible at 650 K onto a clean Au(111) surface held at room temperature. In another experimental run, CuPc, bought from Sigma–Aldrich and used as received, was deposited at 670 K onto a clean Au(111) surface. In chapter 3 for 1D chain formation of molecule on the step edge the exposure time was controlled to about 10 sec and for 2D monolayer formation the time was 60 sec.

FePc, CuPc and F$_{16}$CoPc molecules were purchased from Sigma Aldrich and used as it is for evaporation from resistively heated quartz crucible attached to the sample preparation chamber. In the study of FePc and CuPc on Bi$_2$Se$_3$ discussed in chapter 5. The evaporation temperature for FePc and CuPc was 500 K and 670 K respectively. The Bi$_2$Se$_3$ substrate was kept at room temperature. The concentration of molecules was controlled by the exposure time. The F$_{16}$CoPc molecule was evaporated at 650 K onto Bi$_2$Se$_3$ and Ag(111) kept at room temperature. After the deposition the substrate was kept at room temperature for 30 minutes and then transfered to the LT-STM chamber for STM and STS measurements.

All STS measurements presented in this thesis are collected at 77 K using lack-in amplifier with modulation frquency and modulation voltage are 652Hz and 20mV respectively.

2.5 Computational Details

Calculations were carried out by spin-polarized density functional theory within the projector augmented wave formalism [95] as implemented in the Vienna Ab initio Simulation Package (VASP). [96, 97] The wave functions were expanded in plane-wave basis with 500 eV cutoff. The exchange–correlation energy was described with the Perdew–Burke–Ernzerhof (PBE) form of generalized gradient approximation,[98] which very well describes the structural and electronic properties of bulk Au and CuPc and CuPc(CN)$_8$ molecules in the gas phase. To better model the interaction between molecules and the Au(111) substrate, van der Waals interaction was incorporated by use of DFT-D3 formalism with zero damping. [99] The Au substrate included four Au layers with 10×9 lateral supercell, which were separated by 18 Å vacuum. While the first two layers were fixed to the bulk, the top layers and the

molecules were fully relaxed until the forces were smaller than 0.01 eV/Å. The Brillouin zone was sampled by the use of a $4 \times 4 \times 1$ Monkhorst–Pack k-grid. A $30 \times 30 \times 12$ Åsupercell was used to study molecules in the gas phase, and reciprocal-space integration was carried out by use of the Γ point. The molecular adsorption energy was calculated as $E_{ads} = E_{molecule/Au(111)} - E_{Au(111)} - E_{molecule}$ for CuPc/Au(111) and CuPc(CN)$_8$/Au(111).

Chapter 3

Effect of CN substitution in Copper-Phthalocyanine

3.1 Introduction

Controlled adsorption and the study of the behavior of molecular adsorption over a surface is a necessary requirement to form molecular building blocks and tune their physical properties for organic-based molecular device applications. One of the most useful ways to fabricate such an organic device is by bottom up self-assembly of organic molecules over atomically well-defined solid surfaces[100–102]. The formation of such molecular nanostructure mainly depends on the fine tuning of the intermolecular and the molecule-substrate interactions. Several molecules have already been studied for bottom up self-assembly over atomically flat surfaces [103]. Apart from the flat surfaces using the reconstructed surface for selective adsorption[104, 105], strain-relief patterns for quantum arrays[106] and periodically stepped surfaces for self-ordering growth[107, 108] have been effective for molecular nanostructure formation. The dimensional confinement in one dimensional (1D) nanostructure enhances the transport of charge and spin by restricting the carriers to move in a particular direction [109, 110]. Due to the fewer co-ordination of the atoms at defects and step edges the adsorbed molecules always prefer defects and step edges as their adsorption sites. Hence, a step edge can be used as an ideal template guide for the construction of 1D molecular nanostructures along the step edge. Metal phthalocyanine (MPc) molecules are one of the most studied organic semiconductors due to their stable, planar chemical structure and excellent tunability of their chemical and physical properties[111, 112].There are two ways to tune their chemical and physical properties by changing the central metal ion or by functionalizing the molecule by replacing the H atoms with functional groups. Incorporation of functional groups opens up the possibility to enhance the intermolecular interaction to balance it with the molecule-substrate interaction to develop substrate supported molecular self-assembly. Formation of ordered nanostructures and their physical properties by

incorporating functional groups to the molecule has been studied before[81, 113, 114]. In additon there are few studies of MPc adsorption at the monoatomic(MA) step edge to form 1D chains which include FePc on Au(111)[115], CoPc on Vicinal Au(788)[108] and Au(111)[116], CoPc on fractional atomic step[110], CuPc on TiO_2(110) and TiO_2(210)[117]. In every case MPc adsorbs across the step edge. Only in case of Pb(111) MPcs m get adsorbed flat in the lower terrace whereas same molecules on Au(111) adsorb across the step[118]. To the best of our knowledge there are no reports of the adsorption behavior of functional Pc at the MA step edge. We believe that in the presence of an extra functional group it can modify both the intermolecular and molecule-substrate interaction.

Here, in this chapter we report a comparative study of the site-specific and orientation-selective adsorption of CuPc and -CN functionalized $CuPc(CN)_8$ at the monoatomic(MA) step of Au(111) substrate carried out using LT-STM at 77K. At very low deposition both the molecules prefer to adsorb across the Au(111) MA step edge to form 1D chain and with increasing deposition the molecules start to form a monolayer self-assembly over the flat terraces. STM imaging of Pcs reveals their characteristic planar geometry in the form of a 4-lobe structure [72] for both CuPc and $CuPc(CN)_8$[81]. For the step edge,CuPc molecules adsorb only in one configuration with their two lobes positioned toward the upper terrace of the MA step edge and two lobes toward the lower terrace. $CuPc(CN)_8$ adsorbs in two distinct configurations at the MA step edge, C1 where one lobe rests over the upper terrace with 3 lobes on the lower terrace, and C2 where two lobes rest over the upper terrace with two lobes on the lower terrace. These configurations are strongly site dependent and both form 1D nanostructures along the step edge. In the 1D chain with one lobe resting over the upper terrace, molecules are observed to align in two specific angular orientations with respect to the MA step edge. STS measurements reveal a clear shift in the HOMO energy of the $CuPc(CN)_8$ molecule at the step edge for both configurations with respect to the molecule adsorbed at flat terrace [81]. To get more insight into site and orientation dependent adsorption behavior of $CuPc(CN)_8$ we have done extensive calculations using DFT, which are in accord with the experimental results.

3.2   Adsorption Behavior of CuPc and $CuPc(CN)_8$ at Step Edge

Planar metal phthalocyanine(MPc) consists of two major parts - an inner core where the metal ion can be placed by chemical functionalization to tune the magnetic properties, and an outer periphery where outer meso-hydrogens can be replaced with any
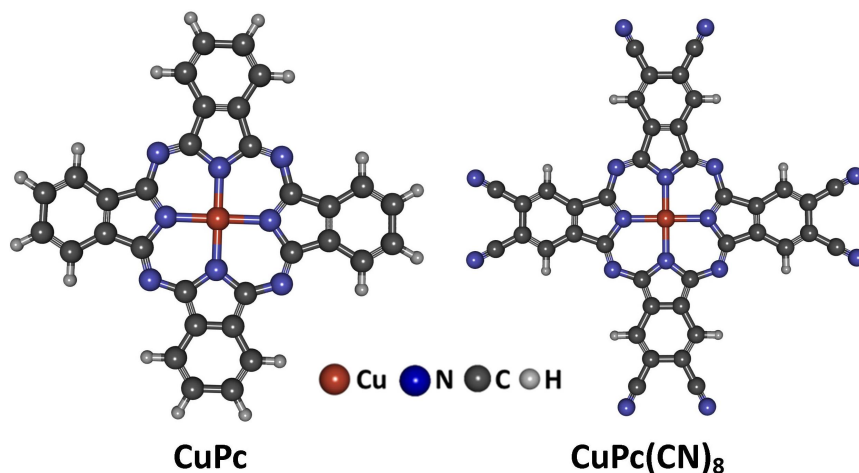
FIGURE 3.1: Chemical Structure of CuPc and CuPc(CN)$_8$

desired functional group. The central molecular core generally interacts with the substrate to provide a site-specific adsorption while the functional groups in the outer periphery ensure the interaction with nearby molecules. Figure 3.1 represents the chemical structure of CuPc and CuPc(CN)$_8$ where 8 selected H atoms are substituted with the cyano(CN) functional group[119].

The D_{4h} symmetry of CuPc and CuPc(CN)$_8$ leads to a 4-lobe structure in STM image [72] and thus, makes it easy to recognize and study the site and orientation dependent adsorption behavior. The molecules were deposited on a clean Au(111) surface for a very low deposition time to ensure only a sparse concentration of molecules adsorbed over the surface at the lowest energy configuration without forming any self assembly. Sample preparation and Experimental details are described in section 2.4.4. Similar to other metal phthalocyanine on metal surface [108, 115, 116, 118], CuPc at very low coverage first adsorbs on to the MA step edge,a Figure 3.2a, as the herringbone reconstruction on Au(111) are clearly visible on the terrace. The herringbone reconstruction is a periodic array of wide face centered cubic(fcc) and the narrow hexagonal close pack(hcp)stacking regions. At the interface between fcc and hcp stacking the atoms go through a bridge transition along $[1\bar{1}0]$ crystallographic direction which appears as a bright line in STM image called soliton wall[120]. At low deposition a few molecules are also observed only over the fcc region of the flat terrace that suggests that after the step edge the next lowest energy adsorption site is the fcc region over the flat terrace. Figure 3.2b is an enlarged STM image of the same area where CuPc is clearly resolved at the MA step edge and over the terrace with 4-lobe structure. Interestingly, the molecules at the steps are observed to be adsorbed at the fcc region MA step edge(step edge at the top of Figure 3.2b) as there are hcp regions that are not covered with molecules. We also don't observe the CuPc at
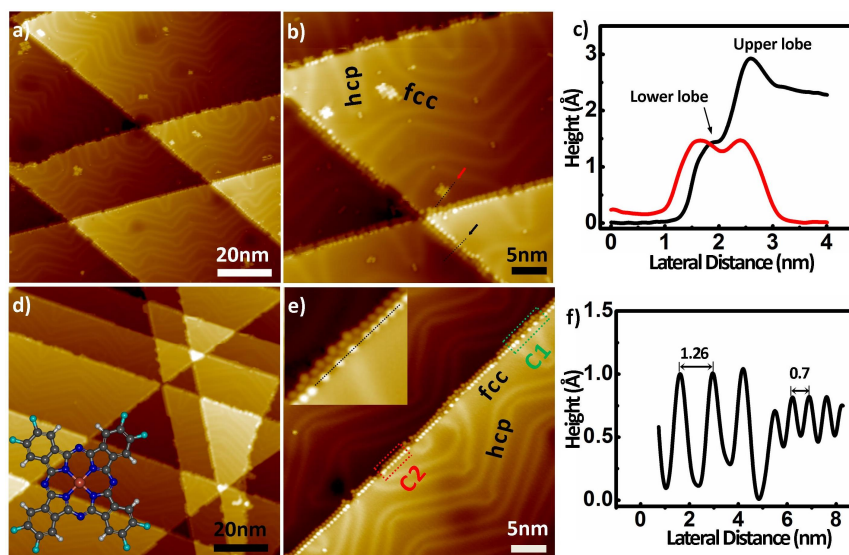
FIGURE 3.2: a) STM image of CuPc at very low coverage showing step edges covered with molecules and few molecules at the fcc region over the flat terrace. b) Enlarged STM image showing molecule at the fcc flat region and molecule at the step with two lobe resting on the upper terrace. c) Cross-sectional profile across two lobes of molecule on the terrace(red) and at step edge(black). d) STM image of CuPc(CN)$_8$ at very low coverage showing only the steps are covered with CuPc(CN)$_8$ e) Enlarged STM image showing two distinct configurations one lobe(C1) and two lobe(C2) resting over the upper terrace at hcp and fcc region respectively. f) Line profile across the two and one lobe configuration as indicated with dotted line in inset image. A schematic of the molecule is shown in the inset of d) (black-C, blue-N, white- H and green- CN). All images are taken at 0.2 nA and 1.0 V.

step edge to act as a nucleation centre to extend the molecular assembly in 2D. This observation is very similar to FePc[115] and CoPc[108, 116] where both are seen to adsorb on the fcc region of the MA step and very few molecules with one lobe resting over the upper terrace are observed and these adsorption sites do not act as nucleation centers to extend the assembly in 2D starting from the step edge. It seems like the general tendency of Pc adsorption at MA step since as all Pc molecules have the same skeletal 4-lobe structure.

The cross-sectional profile across the two lobes of CuPc at the flat terrace(red curve) and at the step(black curve) are shown in Figure3.2 c. The positions of cross-sectional profile are indicated by a red arrow, a black arrow, and a dotted line in Figure 3.2b. Both the lobes of the molecule adsorbed on the terrace show the same height. For the molecule adsorbed at the step edge, the height of the lobe at the lower terrace is same but the height for the lobe resting on the upper terrace of the step edge is decreased. From these two line profiles, the lesser lateral distance between the two lobes reveals a tilted molecular plane at the step edge adsorption. For higher coverage, CuPc binds in a tetramer unit cell geometry and forms a monolayer self assembly that goes over the step edges and covers the Au(111) surface uniformly [81].

Figure 3.2d shows the large area STM image of CuPc(CN)$_8$ at very low deposition, where only the MA step edges are observed to be covered with CuPc(CN)$_8$. Unlike CuPc, CuPc(CN)$_8$ is not observed on the flat terrace deposited as a single molecule. An enlarged STM image of CuPc(CN)$_8$ adsorbed at step edge is shown in Figure 3.2e. Here the herringbone reconstruction is clearly visible and the fcc and hcp regions are marked. Two distinct configurations of CuPc(CN)$_8$ are observed and they are strongly dependent on the adsorption site. The two site-specific configurations are (i) molecule binds with one lobe on the upper terrace and three lobes rest on the lower terrace, at the hcp region indicated by green dotted rectangle at the MA step edge, referred to as configuration C1, and (ii) molecule binds with two lobes on the upper terrace and the other two lobes resting over the lower terrace at the fcc region indicated by red dotted rectangle at the MA step referred to as configuration C2. Configuration C1 and C2 both form 1D chain along the step edge direction. C1 can only be seen over hcp region while C2 can only be seen over the fcc region and the molecules in both these configurations are a bit tilted toward the MA step edge. A line profile of the lateral spacing of the lobe resting on the upper terrace (indicated by dotted black line in inset figure) for both C1 and C2 configurations are shown in Figure 3.2f. The lateral spacing along the step edge for configuration C1 is 1.26 nm that is close to twice the spacing (0.7 nm) of the configuration C2 lobe spacing.

Among these two configurations C1 forms a long 1D chain along the step edge
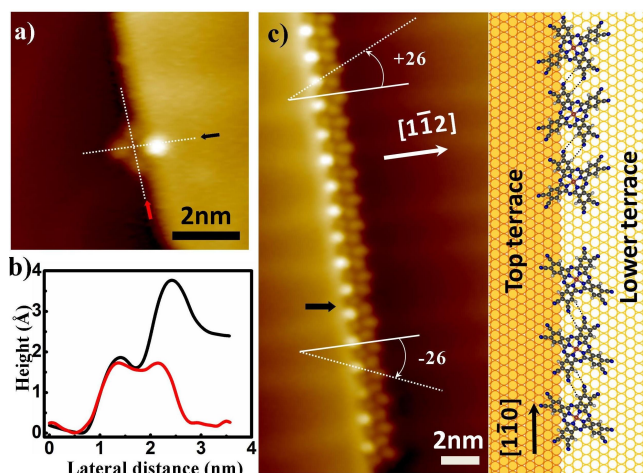
FIGURE 3.3: a)STM image of a single molecule adsorbed at step edge with one lobe resting on the upper terrace. b) Cross-sectional profile of the molecule along two principal axes marked with red and black dotted arrow in a). c) 1D chain of $CuPc(CN)_8$ molecule at step edge of configuration C2 type with schematic drawing of molecule adsorption at step edge. a) and c)(scale bar= 2 nm). Images are taken at 0.3 nA and 1.2 V.

$[1\bar{1}0]$ crystallographic direction when periodic stacking of wide fcc and narrow hcp is perpendicular to the step direction and goes through the step. Figure 3.3a is the STM image of a single $CuPc(CN)_8$ molecule adsorbed at the step edge in C1 configuration. This is similar to the FePc and CoPc with one lobe resting over the top terrace.[115, 116] The black and red arrows indicate the two axes of the molecule. The axis that crosses the step edge is perpendicular to the step edge direction. The cross-sectional profile of the molecule along the two principal axes(indicated in Figure 3.3a) is shown in Figure 3.3b. The height of all three lobes bound to the lower terrace is 1.74 nm. The height of the lobe bound to the upper terrace is 1.38 nm. This asymmetric height might be due to the tilting or due to the difference in electron density distribution at the step edge. Such adsorption has not been observed in case of CuPc. $CuPc(CN)_8$ shows this adsorption presumably due to the -CN functional group. The nitrile nitrogen in $CuPc(CN)_8$ binds more strongly to the substrate than the H-atom in CuPc and stabilizes the C1 cofiguration for $CuPc(CN)_8$. The formation of 1D chain along $[1\bar{1}0]$ guided by step edges with the configuration C1 is shown in Figure 3.3c. Unlike the single molecule adsorbed perpendicular to the step edge in Figure 3.3a, in the 1D chain the molecules are adsorbed parallel to each other and not exactly perpendicular to the step edge. Two specific angular orientations of the molecule in 1D chain of $\pm26°$ with $[1\bar{1}2]$ crystallographic direction were observed as shown in Figure 3.3c. There is a transition point(marked by black arrow) where

the molecular orientation goes from +26° to the -26°. We have also observed long chains with single molecular orientation either +26° or -26°. Both orientational preferences are equally probable. This is indicative of twinning behavior in 1D chain. Twinning effect has been reported in a recent STM report of 2D molecular assemblies on graphite [121] where the origin of twinning is ascribed to the chirality in the 2D system. The difference in orientations between a single molecule at step and forming 1D chain is attributed to the enhanced intermolecular interaction in the 1D chain. In the chain the molecule binds in such a way that each molecule participates in total four C-H$\cdots$N$\equiv$C hydrogen bonding-like interaction with the two nearest neighbor molecules on the opposite side as shown in Figure 3.2c schematic drawing. Such preferred angular orientation of molecules actually enhances the intermolecular interaction via C-H$\cdots$N$\equiv$C hydrogen bonding-like bond formation. We believe this is only possible when electronegative functional groups are there to enhance the intermolecular interaction. Such orientation-specific 1D chain with one lobe resting over top terrace has not been observed with any MPc on metal surface[108, 115, 116, 118]. The $CuPc(CN)_8$ molecules within the 1D chain are very closely bound to each other and it is defect-free which is evident as there is no gap or any structural modification in the chain formation A molecule-laced step edge can also be use-
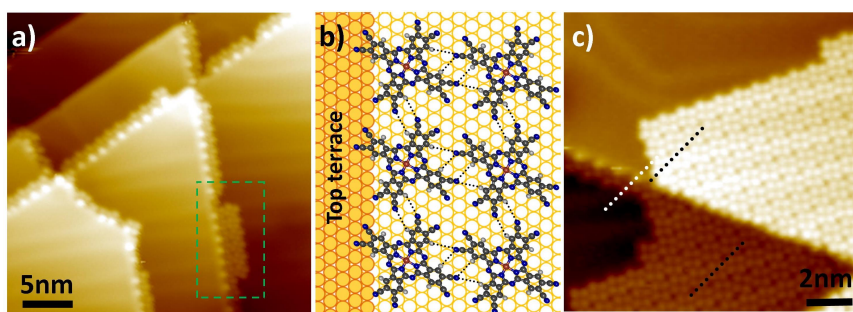
FIGURE 3.4: a)STM image of a molecules adsorbed adjacent to molecule at step edge(green rectangle). b)C-H$\cdots$N$\equiv$C interaction between molecule next to the step edge molecule c) STM image of 2D assembly of $CuPc(CN)_8$ nucleated from 1D chain at the step edge, white and black dotted lines are direction of molecule at step edge and on terrace. I=0.2 nA, V=1.2 V.

ful for designing heterointerfaces using organic molecules. Such chain formation at step edge with hydrogen like bond is fundamentally important, also it may enhance the electron transfer efficiency and make them important for technological application[122, 123]. Step edge functionalized with a 1D molecular chain can be useful for edge passivation to curtail inadvertent and unnecessary growth of molecular layers, thereby limiting the on-surface coverage and the concomitant interplay of interaction energies at the molecular level. A recent study of 4,4-biphenyl dicarboxylic

acid (BDA) molecules on the step edges of Cu(001) revealed a strong interaction between the BDA molecules and step edges that can restrain nucleation on step edges [94].Thus, step edges decorated with molecules can either act as roadblocks to arrest this growth of molecular layers or as sites to advance the growth of the molecular layer as seen in our case as discussed further ahead.

Each lobe corresponds to two adjacent nitrile of the $CuPc(CN)_8$. In 1D chain of C1 type adsorption shown in Figure 3.3c, for a particular molecule two lobes along the step edge participate in forming C-H$\cdots$N$\equiv$C interaction while rest of the two lobes one in the upper terrace and one in the lower terrace remain available to interact with other molecules via formation of C-H$\cdots$N$\equiv$C interaction and can transform this 1D assembly into 2D layer. Figure 3.4a shows that upon increasing the molecular concentration a second set of molecules is seen to be adsorbed just next to the 1D chain in the lower terrace. Each molecule participates in extra pairs of C-H$\cdots$N$\equiv$C interactions, Figure 3.4b. Hence due to the nitriles, molecules in 1D chain act as a nucleation center to expand the 1D chain into a 2D assembly that extend into both upper and lower terraces (Figure 3.4c) and align the same orientation as the molecule in MA step edge. The orientation of the molecule in the MA step edge(white dotted line) and on the upper terrace(black dotted line) is parallel to each other, Figure 3.4c. Thus the molecule at the step edge can act as a nucleation center to form the 2D $CuPc(CN)_8$ assembly through the step edge and the orientation of the molecules in the upper or lower terraces will be determined by the orientation of the molecule in the 1D chain along the step edge.
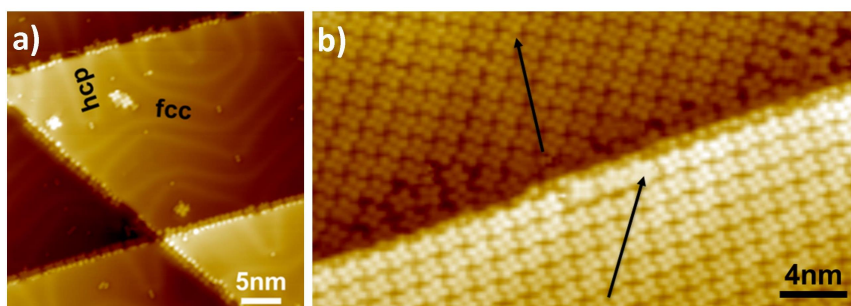
FIGURE 3.5: a)STM image of molecules adsorbed on flat terrace. b)Molecules on both terraces have different orientation and do not align with the molecules at step edge I=0.2 nA, V=1.2 V.

Such step edge nucleation has not been observed with CuPc. In case of CuPc, molecules go over the flat terrace even before saturating the step edge as shown in Figure3.5a. The hcp region at the step edge remains empty but molecules can be seen on the terrace at fcc region. These molecules on the terrace did not diffuse next to the molecules at step edge. CuPc self-assembly on both the upper and lower terrace

are not dependent on orientation of the step edge molecule. The molecules next to the step edge adsorb randomly and then form an independent assembly as shown in Figure 3.5b. The angular orientation of the molecules in upper and lower terrace are entirely different(black arrows represent the molecular orientation). For higher coverage , CuPc(CN)$_8$ forms a tetramer unit cell on the flat terraces and self-assemble into 2D clusters[81]. A striking observation at higher coverage for both CuPc and CuPc(CN)$_8$ is that CuPc(CN)$_8$ assemble into 2D clusters whereas CuPc forms a 2D monolayer on Au(111) surface without cluster formation prior to the full coverage [81].

To study the electronic properties of the CuPc(CN)$_8$ molecules adsorbed at step edge in C1 and C2 configurations, STS measurements are carried out and compared with the dI/dV spectra of the CuPc(CN)$_8$ molecule on the terrace(marked as A) at 77 K, Figure 3.6 . All the dI/dV spectra were taken at the center of the CuPc(CN)$_8$ molecule and show a similar profile; namely, distinct HOMO and LUMO peaks are observed at negative and positive energy (bias voltage). However, the HOMO peak of molecule at step C1 and C2 is slightly shifted from that of the molecule at the terrace but the LUMO peak remains almost in the same position at around ~ 2.1 V. The HOMO energies for A, C2 and C1 are -2.2, -2.0 and -1.9 V respectively(Figure
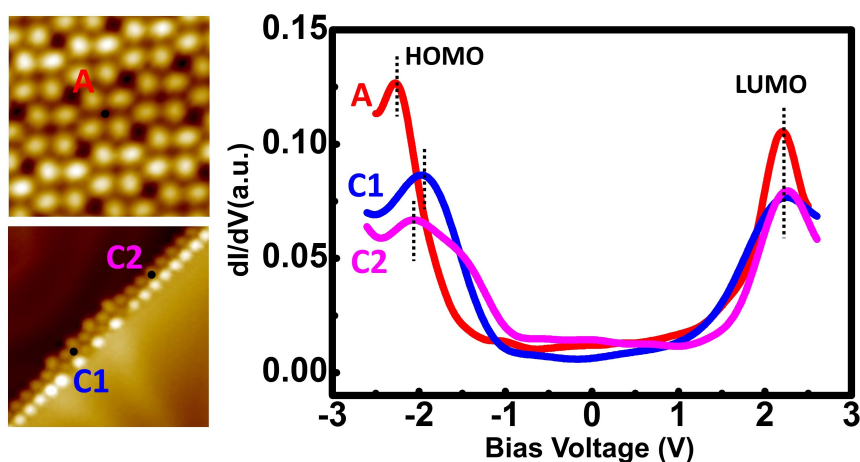
FIGURE 3.6: Two STM images are shown(left). dI/dV spectra for molecule inside a 2D cluster(red curve), C1 one lobe(blue curve) and C2 two lobes(pink curve) resting over the top terrace are presented in the graph. I=0.2 nA, V=1.2 V.

3.6)(Histogram plot for the HOMO and LUMO positions is shown in Appendix C). Thus, going from the CuPc(CN)$_8$ molecule in a cluster over the flat terrace to two lobe resting over the top terrace(C2) to one lobe resting over the top terrace(C1) the LUMO energy decreases. This shift in the dI/dV spectra of step edge molecule with respect to the molecule on the terrace can be attributed to the tilted molecular plane

due to the adsorption at the step edge. This tilted configuration slightly changes the distance between the central Cu(II) ion and the surface Au atom (d_{Cu-Au}), and is responsible for the shift in dI/dV. This shift of HOMO can also be interpreted as a small variation of the HOMO-LUMO gap. Having four lobes oriented such that the molecular plane is parallel to the surface leading to weaker interaction with the surface and HOMO is at -2.2 V. The C2 orientation with two lobes up and the tilted molecular plane, binds more strongly with the surface, HOMO is at -2.0 V. For C1 orientation with one lobe up the tilt is further enhanced, and the HOMO is at -1.9 V. Thus the decrease in HOMO-LUMO gap energy follows the trend – molecule within the cluster –> 2 lobe up –> 1 lobe up. The shifting of HOMO to lower energy is an interesting connection between the change in the structural configuration of the molecule and its direct impact on the electronic properties at the molecular level. Such a control of these shifts can be useful to customize structure-property dynamics within the molecules for targeted applications.

3.3 Density Functional Theory Calculations

The complex interaction of $CuPc(CN)_8$ molecule on the Au(111) step edge was investigated via extensive first-principles density functional theory. It was earlier found that on flat Au(111) surface, the $CuPc(CN)_8$ molecule is absorbed at the hcp-hollow site, where the Cu-ligand axis is rotated by $\sim 30°$ from the Au-$[1\bar{1}0]$ direction[81]. This azimuthal rotation plays an important role while absorbed at the step-edge, which is along the $[1\bar{1}0]$ crystallographic direction, Figure 3.3c. For absorptions at both fcc and hcp sites, two distinct configurations at the step-edge, (i) two lobes of $CuPc(CN)_8$ are resting over the upper terrace and two on the lower terrace (C2 configuration, Figure 1e dotted red square), and (ii) A 45° rotated configuration, where one lobe each is resting over the upper and lower terrace, while two other lobes are along the step edge (C1 configuration, Figure 1e dotted green square) were computationally studied. At the step edge, the absorbed molecules have a new degree of freedom and can tilt by an angle τ, which optimizes the electronic interaction between the molecule and stepped substrate. The two-lobe C2 configuration adsorbed at the hcp-site to be the ground state has a strong electronic interaction of -3.03 eV, which is tilted at the step-edge by $\tau \sim 9°$ [Figure 3.7(a)]. The height of the central Cu(II)-ion is calculated to be 2.65 Å above the upper terrace. In contrast, the tilted one-lobe C1 configuration absorbed at the hcp-site is computed to be metastable with -2.59 eV binding energy [Figure 3.7(b)]. Tilting of $CuPc(CN)_8$ molecule at the step edge increases the binding energy of C1 configuration by about 0.44 eV from the corresponding C2 configuration. Furthermore, the otherwise flat $CuPc(CN)_8$ becomes

non-planar and bends [Figure 3.7(a) and (b)]. The simulated STM images clearly indicate two and one lobe for C2 and C1 configurations Figure 3.7(c) and (d). These computational findings are in excellent agreement with the present experimental results that the two-lobe absorption is more favorable than one-lobe absorption Figure 1e . In contrast, the adsorption at the fcc step edge site are found to be much higher in energy (~ 0.45 eV) and thus are not preferable. The current results are in contrast to FePc absorption on Au(111) step edge, where the fcc site is preferred over the hcp site [115] . In comparison to the adsorption at the hcp step edge, the adsorption at the hcp site on a flat Au(111) surface maximizes the electronic interaction of the aza-N atoms with the Au-substrate. Further, an azimuthal rotation of the Cu-ligand axis about the [1$\bar{1}$0] direction increases this interaction, and the molecule binds strongly on the flat Au(111) surface with -5.86 eV binding energy.
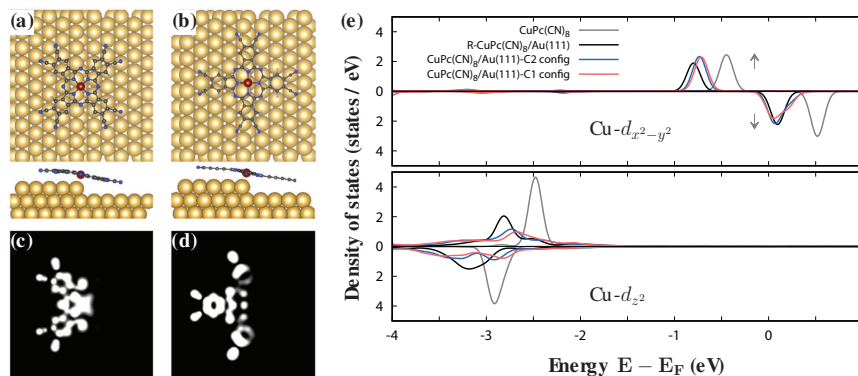
FIGURE 3.7: Top and side views of the optimized configurations of the absorbed CuPc(CN)$_8$ at the high-symmetry hcp-site on Au(111) step edge (a) Two lobes on the upper terrace (C2 configuration) and (b) one lobe on the terrace(C1 configuration). In both cases, the molecule tilts and bends at the step edge to optimize the absorption energy. (c, d) The simulated STM images at bias voltages -2.72, and -2.68 V for the C2 and C1 configurations, respectively. (e) The Cu-projected spin-polarised density of states, calculated with 0.1 eV smearing , and compared with the molecule at the gas-phase and the molecule absorbed at the flat Au(111) surface. While the localized $d_{x^2-y^2}$ generates the magnetic moment, the d_{z^2} interacts with the STM tip to generates the tunneling current. The shift in d_{z^2} with respect to the different adsorption configuration is in excellent agreement with the present experimental result.

The calculated spin-polarized density of states (DOS) indicates the $1\mu_B$ magnetic moment for gas-phase CuPc(CN)$_8$ arises from the singly occupied localized Cu-$d_{x^2-y^2}$ orbital located at -0.45 eV below the Fermi level [Figure 3.7(e)]. Due to the structural reconstruction of the molecule at the step edge, this moment generating localized Cu-$d_{x^2-y^2}$ orbital is pushed down in energy to -0.74 and -0.71

eV for the C2 and C1 configurations, respectively. This gives rise to $1\mu_B$ moment for both configurations. In contrast, the Cu-$d_{x^2-y^2}$ orbital is localized at -0.85 eV, while the molecule is absorbed at the flat Au(111) surface [81]. It is important to note here that the in-plane Cu-$d_{x^2-y^2}$ orbital does not contribute to the tunnelling current, and the calculated DOS indicates that Cu-d_{z^2} is exposed to the STM tip, which is thus the measured HOMO in the present STM experiment. Here the observation is two-fold [Figure 3.7 (e)]. First, for all cases, the Cu-d_{z^2} orbital is much broader in energy than the same in the gas-phase, which indicates a strong interaction with the Au(111) surface. Second, the Cu-d_{z^2} orbital is pushed down in energy to -2.72 and -2.68 eV for the C2 and C1 configurations, respectively, with respect to -2.48 eV for the gas-phase CuPc(CN)$_8$. In contrast, for the most probable adsorption on the flat terrace, the Cu-d_{z^2} lies at -2.85 eV with respect to the Fermi level. This trend in HOMO energy,–molecule within the cluster –> 2 lobe up –> 1 lobe up, is in excellent qualitative agreement with the present experimental observation in Figure 3.6.

3.4 Conclusions

Using LT-STM imaging the adsorption of CuPc and CuPc(CN)$_8$ molecules at the MA step edges of Au(111) surface has been investigated. While CuPc adsorbs in one configuration, there are two adsorption configurations for CuPc(CN)$_8$ at the Au(111) step edge forming 1D linear chains. The alignment of CuPc(CN)$_8$ molecules in one of these configurations enables a transition from a linear 1D assembly to a 2D planar assembly upon higher coverage of molecules. STS measurements show that there is a systematic shift of HOMO to higher energy as the molecule changes its configuration. This is a direct correlation between the adsorption morphology and the local electronic structure of the molecule. The result from DFT calculations for CuPc(CN)$_8$ adsorption and the shift of HOMO are in accord with the experimental results. Our work advances the current understanding of the step edge-molecule interaction and intermolecular interactions and thereby demonstrates that changing the pendant group of phthalocyanine can act as a handle for designing specific adsorption morphologies at the molecular level.

Chapter 4

Energy-Specific Chirality in Cyano Substituted CuPc

4.1 Introduction

Self-assembly is a ubiquitous phenomenon and has its hallmark in various systems at all length scales ranging from carbon atoms in interstellar medium, [124]organic molecules in interstellar ices,[125]and proteins in cephalopods[126] to three dimensional photonic crystals[127]. Molecular self-assembly in solution as well as in solid phase relies on the collective strength of noncovalent interactions[128]. For polymerization induced by visible light, nanoparticles in different morphologies of self-assembly can be realized in solution,[129] whereas for substrate-supported self-assembly of diacetylene molecules, polymerization by UV light has been demonstrated to template the surface[130]. Conjugated polymers, with their propensity for supramolecular self-assembly, have proved to be promising for applications in optoelectronic devices.[131–134] Surface self-assembly entails a rich mix of physisorption and chemisorption, giving rise to a coordinated network of atoms and molecules on surfaces. It indulges in covalent as well as noncovalent bonds, thereby making this supramolecular chemistry indispensable for interdisciplinary advances toward new functionalities[135]. In the case of organic molecular self-assembly, phthalocyanines (Pc) are one of the prime members of organic functional materials with applications in molecular photovoltaics. Their potential to enhance the efficiency of solar cells by using different anchoring groups or ligands has been well-demonstrated[136]. Surface-supported Pcs like (RuPc)2 dimers are promising entities for spintronics and nanoscale devices[137]. The introduction of functional groups to the periphery of the Pc core opens up the possibility of more in-plane intermolecular interactions between adsorbed molecules on a surface[138]. Adding an electron-withdrawing group to phthalocyanine tunes it remarkably for high-performance electronic device applications.[139] It is an effective way to tailor different types of self-assemblies and

molecular architectures[140] with desirable properties for targeted applications in organic electronic and optoelectronic devices[141, 142]. Many molecular assemblies have directional intermolecular interactions guiding a wide range of one- and two-dimensional (1D and 2D) supramolecular self-assemblies,[143, 144] while in other assemblies a balance of the interaction strengths between intermolecular interaction and molecule–substrate interaction[145] forms a bimolecular structure,[146] making the self-assembly relevant for spintronics.[147] Molecular self-assembly on 2D materials is also pertinent from the viewpoint of surface functionalization of the 2D substrates. This functionalization, either covalent or noncovalent, has the potential to exploit the inherent properties of the 2D materials and to enhance them for dedicated objectives like flex electronics[148].Chiral molecules carry properties of mirror symmetry and handedness. The adsorption and assembly of chiral molecules on a surface leads to symmetry breaking, leaving chiral signatures that include molecule–surface interactions[149]. If both the molecule and the surface are achiral, the local chirality at a single molecule upon adsorption can lead to supramolecular chirality at the assembly level through weak, noncovalent bonding interactions[150]. These interactions are substantially weaker than the covalent bonding within a molecule. These noncovalent interactions can lead to chirality in different forms, for example, surface-induced chirality in a single molecule[151] or in a 2D supramolecular assembly.[152, 153] Achiral molecules with a specific geometry can self-assemble through intermolecular interactions like hydrogen bonding. Such a self-assembly shows organizational chirality[154–156]. Also, the molecules can encounter conformational changes upon adsorption and exhibit chirality that arises from a change in the conformation of the molecules[157, 158]. Apart from these chiral manifestations, there is one more important kind of chirality that is completely electronic in nature and has recently been observed in copper phthalocyanine (CuPc) on Ag(100)[159] and ZnPc on Cu(100)[160]. This type of chirality is independent of the geometrical structure of the molecule, but it is energy-dependent. It occurs at specific energies, which means it represents the chiral nature of the molecule at a specific orbital energy. How pendant-group substitution of a phthalocyanine can enhance its intermolecular interactions and introduce energy-specific chirality in its self-assembly forms the premise of our study.

In continuation with step edge adsorption study in chapter 3, here in this chapter two dimensional (2D) self assembly of $CuPc(CN)_8$[119] on flat terrace of Au(111) has been explored using STM and STS at 77K. We then compare it with the self-assembly of CuPc on flat terrace of Au(111). Both these molecules assemble to form a tetramer unit cell on the surface. They exhibit adsorption-induced organizational chirality, which arises due to the characteristic arrangement of molecules in

the assembly. The herringbone reconstruction of Au(111) remains unperturbed upon $CuPc(CN)_8$ assembly, but for the CuPc assembly it increases, which is indicative of a stronger molecule–substrate interaction than intermolecular interaction for CuPc as compared to $CuPc(CN)_8$. STS measurements can determine the highest occupied molecular orbital (HOMO) and lowest unoccupied molecular orbital (LUMO) energy levels for the molecule in its self-assembled mode. A remarkable observation from STS is that as the chemical structure of the molecule is changed from CuPc to $CuPc(CN)_8$, the HOMO–LUMO gap increases from 3.0 eV (for CuPc) to 4.46 eV. To verify and to gain more insight into these results, we have done extensive calculations using density functional theory (DFT). Both our experimental observations are well-supported by these calculations. Apart from the organizational chirality, the voltage-dependent STM images reveal the chiral nature of individual $CuPc(CN)_8$ molecules on Au(111) only at LUMO energy, whereas such chirality is not present in the assembly of CuPc on Au(111). This voltage-dependent chirality in the 2D assembly of $CuPc(CN)_8$ on Au(111) is characterized by orbital energy dependence, thereby making it completely electronic in nature. At LUMO energy, the handedness of each

FIGURE 4.1: a) STM image of $CuPc(CN)_8$ clusters over flat terrace. b) STM image of a single cluster with herringbone reconstruction in backgrounds c) Enlarged molecular resolution STM image showing the relative arrangement of the molecule. Unit vectors $\vec{a}$ and $\vec{b}$ are shown to specify the unit cell in the assembly Inset showing a ball-and-stick model of CuPc(CN)8 superimposed on a single molecule. d)STM image of CuPc monolayer coverage on Au(111) e) Enlarged STM image showing herringbone periodicity increased to 7.2 nm. f) Molecular resolution showing identical unit cell formation to c) I=0.2 nA, V=1.0 V.

chiral molecule is decided by the direction of the dipolar coupling interaction in the tetramer unit cell. On the basis of comparison of CuPc on Au(111) with $CuPc(CN)_8$ on Au(111), we claim that the antiparallel dipolar coupling interaction present in the $CuPc(CN)_8$ tetramer, a consequence of cyano substitution of CuPc, strengthens the intermolecular interaction and plays a pivotal role in chiral manifestation in the $CuPc(CN)_8$ molecular self-assembly at LUMO energy. Thus, a combination of our work, experimental findings from STM and STS, and supporting DFT calculations gives us a holistic picture of the system under study and installs a footprint arising from cyano substitution of CuPc.

4.2 2D self-assembly of CuPc and $CuPc(CN)_8$ on flat terrace of Au(111)

$CuPc(CN)_8$ molecules were deposited on the Au(111) surface. These molecules assemble in the form of hundred-nanometer-sized rectangular clusters scattered over the Au(111) surface, and in some cases the assembly spills over the step edges as shown in STM image in Figure 4.1a. The enlarged STM image of one such cluster is shown in Figure 4.1b where these square-planar $CuPc(CN)_8$ molecules are assembled in a rectangular array. Through the array and in the background of the array, the bright lines are the lines of the herringbone reconstruction.This reconstruction is attributed to the atoms in the topmost layer being compressed by 4.5% in the $[1\bar{1}0]$ direction, thereby placing 23 atoms over the 22 atoms in the underneath layer. To remain thermodynamically stable, this compression leads to the formation of a periodic array of cubic close packed face-centered cubic (fcc) and hexagonal close-packed (hcp) regions. The interface between the hcp and fcc regions is marked by a dotted line in Figure 4.1 b. These regions are separated by a region where atoms go through a bridge-site transition that appears as a bright line in the STM image called a soliton wall.[120] A pair of soliton walls is called herringbone, and their average separation is 6.34 nm on Au(111). This separation, also referred to as herringbone reconstruction periodicity, is a sensitive tool to measure the interaction strength of an absorbed molecule upon a substrate. For a strong interaction between the adsorbed molecules on Au(111), the herringbone separation increases from 6.34 nm and disappears when all the 4.5% Au atoms are removed depending on the strength of the interaction.[91, 161–163] For the $CuPc(CN)_8$ assembly, the herringbone spacing is 6.30 nm (Figure 4.1b) which is same as its free space value. Hence, the self-assembly does not remove the reconstruction, indicating weak van

der Waals bonding between CuPc(CN)$_8$ and the Au(111) surface. The 4-fold symmetry of CuPc(CN)$_8$ is observed in the self-assembly as a 2D square lattice. Figure 4.1c shows close-up STM images of the assembly where the 2D lattice has unit cell parameters $\vec{a} = \vec{b} = 1.56$ nm and the molecules have a high packing density of 0.41 molecule/nm^2. A schematic of CuPc(CN)$_8$ molecule is superimposed with the STM image shown in the inset of Figure 4.1c. The self-assembly of CuPc is shown in Figure 4.1d. These molecules form monolayer coverage [unlike clusters for CuPc(CN)$_8$], going over the step edges of Au(111).The assembly is planar and each molecule has a square geometry as expected. The herringbone reconstruction can be seen through the monolayer. The herringbone reconstruction periodicity for this assembly is 7.2 ± 0.3 nm (Figure 4.1e), larger than the unperturbed 6.3 nm value seen for CuPc(CN)$_8$ as discussed previously.This enhanced herringbone periodicity is a direct pointer to the stronger molecule–substrate interaction in the CuPc/Au(111) assembly. CuPc exhibit the identical square lattice unit cell formation. The unit cell vectors are $\vec{a} = \vec{b} = 1.53 \pm 0.1$ nm and packing density is 0.43 molecule/nm^2. To investigate the other the other exciting phases of self-assembled growth of both the molecules we have searched for different regions of the sample. We have observed that both molecules form two different mirror symmetric square lattice unit cell with similar unit cell vectors as mentioned above. Figure 4.2 a and b represent two mirror symmetric unit cell for CuPc(CN)$_8$. For CuPc Figure 4.2 c, and d are the two mirror assembly with mirror symmetric unit cell. From the STM image it is clearly observed that Figure 4.2a and c have the identical unit cell and corresponds to configuration α. Where as the identical assembly in Figure 4.2 b and d corresponds β. The configuration is referred to as α when the angle δ between the unit cell vector of the assembly and the molecular symmetry axis M_1 of CuPc(CN)$_8$ is $32° \pm 2°$ and as β when it is $56° \pm 2°$. The schematic of both configurations α and β are shown in Figure 4.2 e and f. These two configurations are mirror symmetric to each other.The assembly of CuPc(CN)$_8$ and CuPc over Au(111) shows the adsorption-induced organizational chirality. For CuPc(CN)$_8$ in both configurations, the unit vectors are $\vec{a} = \vec{b} = 1.56$ nm. Configurations α and β are unique to each molecular cluster and no mixed configuration was seen in any cluster.The black dotted lines in Figure 4.2 e and f denote the probable intermolecular H···NC hydrogen bonding between CuPc(CN)$_8$ molecules that mediates the intermolecular attraction, gives rise to a 2D close-packed assembly on Au(111), and guides the pattern formation. This is similar to the self-assembly of ZnPcCl$_8$, where the 2D hydrogen-bonded network is formed due to H···Cl interactions.[162] In this case, it is the highly electronegative nitrogen belonging to the cyano group that interacts with two hydrogen atoms of the nearest neighboring molecule. In addition to the hydrogen bonding, there is an intrinsic dipole due to
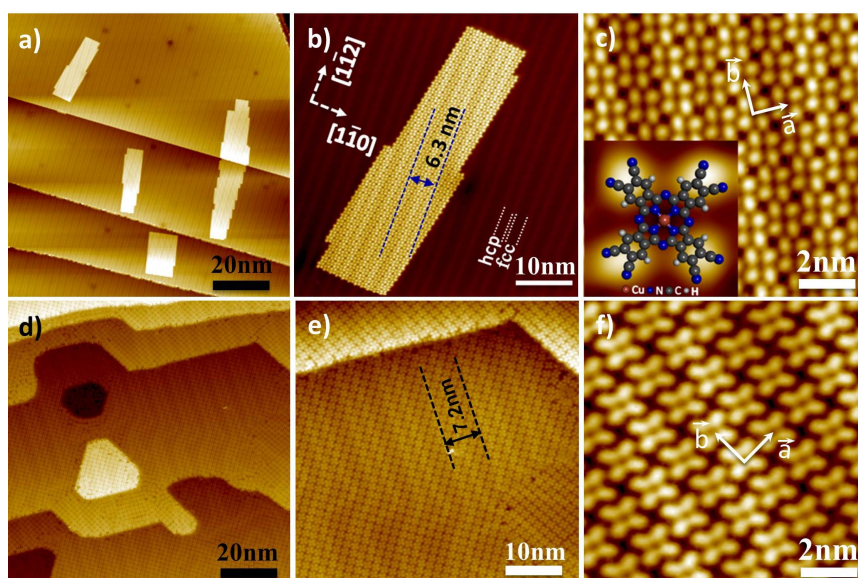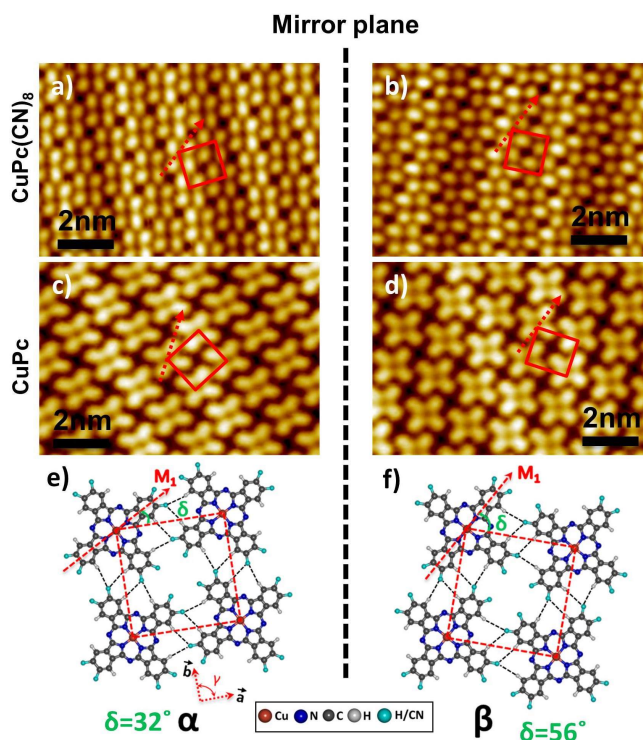
FIGURE 4.2: a) STM image of CuPc(CN)$_8$ clusters over flat terrace. b) STM image of a single cluster with herringbone reconstruction in backgrounds c) Enlarged molecular resolution STM image showing the relative arrangement of the molecule. Unit vectors $\vec{a}$ and $\vec{b}$ are shown to specify the unit cell in the assembly Inset showing a ball-and-stick model of CuPc(CN)$_8$ superimposed on a single molecule. d)STM image of CuPc monolayer coverage on Au(111) e) Enlarged STM image showing herringbone periodicity increased to 7.2 nm. f) Molecular resolution showing identical unit cell formation in c) I= 0.2 nA, V= 1.0 V.

each cyano group, and these also interact with each other in the molecular assembly. This interaction is the antiparallel dipolar coupling and was also observed in the self-assembly of cyano-functionalized porphyrins [143] and triarylamines [164] on Au(111). Both hydrogen-bonding and dipolar-coupling intermolecular interactions stabilize the self-assembly, giving rise to submonolayer domains of different sizes and shapes. No single CuPc(CN)$_8$ molecule adsorption was observed on the Au(111) surface even at low coverage, as the substrate was held at room temperature during molecule deposition, but observing single molecules at very low temperature like 5 K is plausible. Only 2D regions with tetramers were observed. Also conspicuous by its absence was the formation of 1D chain. This could be due to the high affinity for hydrogen bonding in all four in-plane directions. The black dotted lines for the CuPc unit cell denote the probable intermolecular van der Waals interactions between the CuPc molecules that bind the assembly, in addition to the stronger

molecule–substrate interaction evidenced by the 7.2 ± 0.3 nm herringbone recon-
struction periodicity that makes the CuPc/Au(111) self-assembly stable. During STS
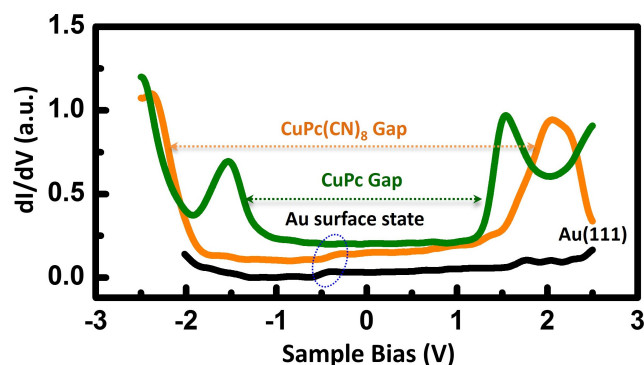
FIGURE 4.3: dI/dV spectra at the center of molecule for CuPc(green)
and CuPc(CN)$_8$ (orange). HOMO and LUMO peaks for CuPc(CN)$_8$
are at -2.3 V and 2.0 V and for CuPc they are at -1.5 and 1.5 V.The
Au(111) surface state at -0.5 V is indicated by the black trace in the
dI/dV spectra over Au(111) (black). The blue dotted oval highlights
the absence of the Au(111) surface state in the CuPc gap, the presence
and a slight shift of the Au(111) surface state toward the Fermi level
in the CuPc(CN)$_8$ gap, and the surface state of bare Au(111) surface

measurements, the tunneling of electrons through the HOMO and LUMO gives rise
to peaks in dI/dV. The dI/dV spectra were taken at the center of the molecule, for
both CuPc(CN)$_8$ and CuPc, and were measured for several molecules located in dif-
ferent positions on the substrate. The average of dI/dV spectra taken over CuPc(CN)$_8$
molecule (orange curve), over CuPc molecule (green curve), and on the bare Au(111)
substrate (black curve) are shown in Figure 4.3. As seen in Figure 2, for CuPc(CN)$_8$,
the LUMO occurs at 2.0 V and the HOMO occurs at -2.3 V with reference to the
Fermi energy at V = 0 V. For CuPc, the LUMO occurs at 1.5 V and the HOMO
occurs at -1.5 V.The key result of these spectra is that the HOMO–LUMO gap in-
creases from 3.0 to 4.3 V upon going from CuPc to CuPc(CN)$_8$. The STS curve
was measured over molecules in different positions of the cluster, but no signifi-
cant change was observed with respect to the STS peak position. Since the spec-
tra were recorded at different sites on Au(111), any substrate site-dependent orbital
energy fluctuation, as seen in other systems, can be ruled out.[165] Spin density
functional theory (SDFT) calculations have shown that the band gap increases from
CuPc (1.1 eV) to F$_{16}$CuPc (1.4 eV).[166] For our system, we speculate that the in-
crease in HOMO-LUMO gap from CuPc to CuPc(CN)$_8$ is a consequence of the role
played by the cyano groups. The HOMO-LUMO gap is also known to be affected
by molecule–substrate interaction: as the molecule–substrate interaction decreases,
the HOMO-LUMO gap increases. This is due to reduced screening of the substrate

that enhances the Coulomb repulsion for tunneling electrons.[167, 168] Our observation of the increased HOMO-LUMO gap for the $CuPc(CN)_8$/Au(111) system, where the molecule–substrate interaction is weaker compared to the CuPc/Au(111) system as evidenced by the intact herringbone periodicity and by the presence of surface state[169] in the STS data for the $CuPc(CN)_8$/Au(111) system, is consistent and in line with the expected behavior of such molecule–substrate systems. The substrate molecule interaction in self-assembly of CuPc is stronger than that of $CuPc(CN)8$, as seen from the change in periodicity of the herringbone reconstruction of Au(111) through the assembly. This is also reflected in the dI/dV spectrum of CuPc (green trace in Figure 4.3), where the Au(111) surface state is not seen. However, the surface state can be seen in the dI/dV spectrum of $CuPc(CN)_8$ (orange trace in Figure 4.3). Thus, our inference of the molecule–substrate interaction for the CuPc/Au(111) system being stronger than the $CuPc(CN)8$/Au(111) system is validated by the change in herringbone reconstruction periodicity, the quenching of the surface state for the CuPc/Au(111) system, and the trend of the HOMO–LUMO gap variation. The slight shift of the Au(111) surface state toward the Fermi level in the case of $CuPc(CN)_8$ can be ascribed to the phenomenon of molecular adsorption upon Au(111), albeit with a weak van der Waals interaction[170].

4.3   DFT Calculations for CuPc and $CuPc(CN)_8$ on Au(111)

To corroborate the complex structural modulation of Au(111) substrate and the electronic interaction of CuPc and $CuPc(CN)_8$ molecules with the substrate, we have performed extensive ab initio calculations within DFT implemented in VASP[96, 97]. An unreconstructed Au(111) slab model is a good approximation for studying the electronic properties of single CuPc and $CuPc(CN)_8$ molecules, along with the structural changes of the substrate that may occur due to molecular adsorption. There are four high-symmetry adsorption sites on Au(111) surface, namely, the top, hcp-hollow, fcc-hollow, and bridge sites. However, the orientation of the adsorbed molecules is complex due to their rotational degree of freedom with respect to the crystalline direction of the substrate. We find that both CuPc and $CuPc(CN)_8$ molecules are adsorbed at the hcp-hollow site. The most stable azimuthal orientation of the Cu–ligand axis for both molecules is rotated by $\sim$30° from the [1$\bar{1}$0] direction of the Au(111) surface (Figure 4.4 a and b). Such azimuthal rotation increases the binding energy by 0.25 and 0.06 eV for CuPc and $CuPc(CN)_8$, respectively, from the corresponding hcp-hollow site adsorption. The CN group in (R)-$CuPc(CN)_8$ strongly influences the interaction with substrate and binds strongly (-5.86 eV) compared to (R)-CuPc (-4.66 eV). The trend in the binding energy can be explained in terms of
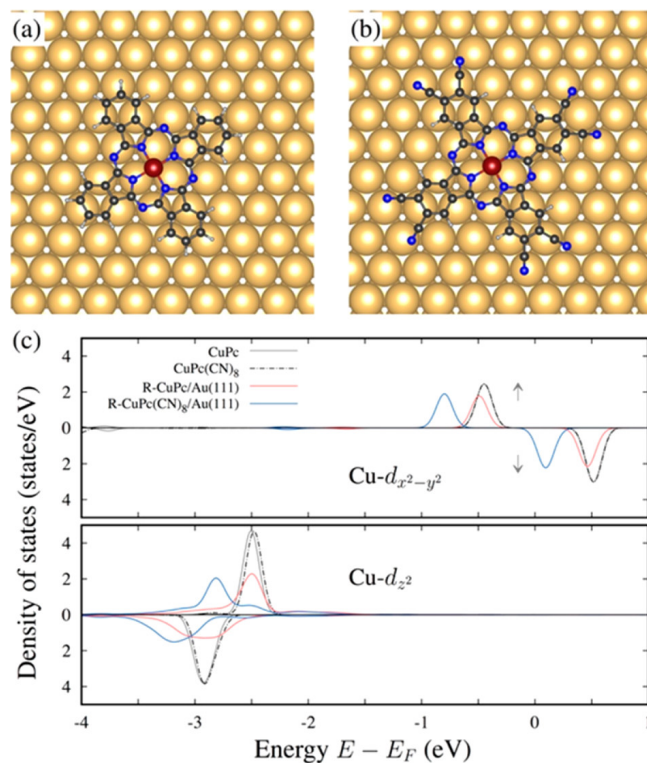
FIGURE 4.4: (a, b) Configurations of adsorbed molecules and (c) corresponding density of states. Both (a) CuPc and (b) CuPc(CN)$_8$ are adsorbed at the high-symmetry hcp-hollow site on Au(111) substrate with $\sim$30 $^\circ$ azimuthal rotation of the Cu ligand about the [1 $\bar{1}$0] direction of the substrate. (c) Spin-polarized density of states projected on Cu, calculated with 0.1 eV smearing and compared with the corresponding molecule in the gas phase. The Cu d$_{x^2-y^2}$ and Cu d$_{z^2}$ orbitals are shown.

the interaction between sp^2 orbitals localized on aza-N atoms with the Au atoms, as will be discussed.[159] The average vertical distance between aza-N atoms for (R)-CuPc(CN)$_8$ with Au(111) substrate is found to be much shorter, 3.11 Å, compared to that for (R)-CuPc, which is 3.23 Å. Thus, (R)-CuPc(CN)$_8$ binds strongly through the increased interaction between aza-N atoms and Au substrate. Consequently, in their optimized configurations, a remarkable net charge transfer of 0.55 and 1.22 electrons into the CuPc and CuPc(CN)$_8$ molecules, respectively, obtained from the Bader charge analysis,[171] explains the trend in adsorption energy. The experimental trend observed in the herringbone reconstruction can be qualitatively explained by investigating the structural details of the top Au layer without and with absorbed molecules. Within the PBE exchange–correlation functional,[171] the distance between successive Au(111) layers for bulk Au is $a/\sqrt{3}$ - 2.40 Å, where a is the lattice parameter (4.16 Å). Due to the lack of periodicity, the top layer of the bare Au(111) surface is reconstructed such that the vertical distance from the top layer

to the layer below decreases to 2.37Å, whereas the layers below are unperturbed. While the adsorption of (R)-CuPc(CN)$_8$ does not perturb this picture, the (R)-CuPc molecule pulls up the Au atoms below by an amount of 0.01 Å. This explains the observation of modified herringbone reconstruction periodicity in STM images for CuPc molecular assemblies. Thus, while the periodicity of the herringbone reconstruction is unperturbed for (R)-CuPc(CN)$_8$ absorption, remaining intact at 6.3 Å, for (R)-CuPc this periodicity increases to 7.2 ± 0.3 Å. The calculated spin-polarized density of states (DOS) indicates that the magnetic moments of 1μB for CuPc and 0.92μB for CuPc(CN)$_8$ arise from the singly occupied localized Cu d$_{x^2-y^2}$ orbital, which lie at -0.5 and -0.85 eV with respect to the Fermi level (Figure 4.4c). This is in contrast to their gas-phase counterparts, where the Cu d$_{x^2-y^2}$ orbital lies at $\sim$-0.45 eV for both molecules, and thus the cyano group does not affect the Cu d orbitals in the gas phase. Note that d$_{x^2-y^2}$ orbital does not contribute to the tunneling current, and the DOS indicates that the HOMO is of Cu d$_{z^2}$ and exposed to the STM tip. Similar to d$_{x^2-y^2}$ orbital, in the gas phase the cyano group does not affect the energy position of the d$_{z^2}$ orbital, which lies at -2.51 and -2.48 eV for CuPc and CuPc(CN)$_8$, respectively. However, the picture changes drastically when the molecules are adsorbed on the Au(111) substrate. Owing to the presence of the cyano group, the Cu d$_{z^2}$ HOMO is pushed deeper in energy at -2.85 eV due to stronger aza-N and Au interaction for CuPc(CN)$_8$/Au(111). However, this is unperturbed for (R)-CuPc/Au(111). This picture qualitatively explains the experimental trend in HOMO. The degenerate d$_{xz}$ and d$_{yz}$ orbitals for both molecules lie deeper in energy compared to the corresponding d$_{z^2}$ orbital.

4.4   Energy Specific Chirality in CuPc(CN)$_8$ on Au(111)

With HOMO and LUMO energy levels as reference points, voltage-dependent imaging was carried out for both CuPc(CN)$_8$ and CuPc assemblies to see if the conformation of the self-assembled molecules undergoes any change as a function of voltage. Figure 4.5 shows selective images related to this study. Note that the adsorption-induced organizational chirality is present at all voltages. For CuPc(CN)$_8$ on Au(111), no chiral contrast is seen in the HOMO-LUMO energy gap and at HOMO energy. This is clear from the STM images at -2.3 V and 0.5 V (Figure 4.5 a,b), where the conformation remains unchanged. Apart from the organizational chirality, an unexpected chiral conformational change is observed at 2.0 V, the LUMO energy, when the individual molecule in the tetramer conformation becomes chiral (Figure 4.5c). As chirality of an individual molecule is dependent on
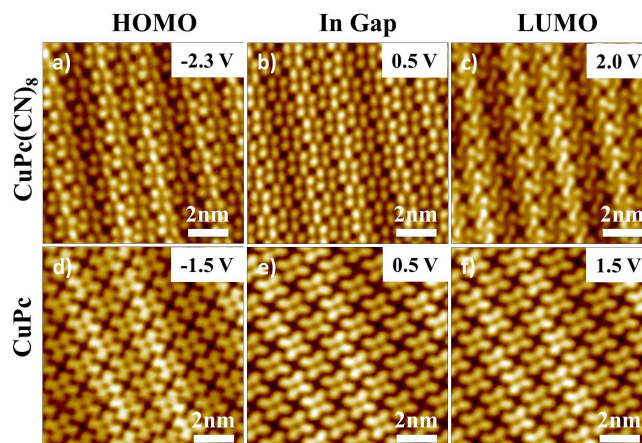
FIGURE 4.5: (a–c) Voltage-dependent STM images of CuPc(CN)$_8$ on Au(111) at voltages corresponding to (a) HOMO, (b) in the gap, and (c) LUMO for the same area, taken with constant current 0.2 nA. Among them, image c at 2.0 V shows chirality. (d–f) Voltage-dependent STM images of CuPc on Au(111) at voltages corresponding to (d) HOMO, (e) in the gap, and (f) LUMO for the same area, taken with constant current 0.2 nA. No chirality is seen for the CuPc assembly at any voltage.

the specific energy, it is electronic in nature [159]. The molecular assembly undergoes a corresponding change that is enhanced with increasing positive bias voltage. This electronic chirality emerges at the onset of LUMO energies from 1.8 V and remains chiral up to applied bias of 2.5 V. This energy range matches with the onset of the LUMO peak in the dI/dV spectra in Figure 4.3. The underlying organizational chirality remains intact, and this energy-specific electronic chirality in individual molecules emerges on top of the organizational chirality. In this assembly, an individual molecule at LUMO energy becomes chiral so the chirality is propagating from organizational to electronic chirality in an individual molecule. This is evident from Figure 4.5 and will be discussed in further detail. For CuPc on Au(111), at HOMO energy, there is a slight change in the appearance of the individual molecules in the assembly (Figure 4.5d). Each lobe of the four-lobed molecule looks squarelike, as opposed to the oval shape of the lobes. The oval shape is commonly seen at any energy in the gap (Figure 4.5e) and at LUMO energy (Figure 4.5f). Thus, no change in the shape of the lobe occurs at any energy in the gap or at LUMO energy. The slight deviation of the lobe shape at HOMO (-1.5 V) could be due to interaction of the CuPc HOMO orbital with the Au(111) surface, as the CuPc/Au(111) interaction is strong. A bias-dependent change in the molecular structure has been reported for the BTDA-TCNQ/Au(111) supramolecular assembly at LUMO energy due to the unoccupied states at LUMO energy.[172] The emergence of supramolecular chirality in

CuPc(CN)$_8$ at LUMO energy is a striking observation, and the absence of chirality in the CuPc assembly is a pointer to the role played by the eight cyano groups in contributing to this orbital-dependent electronic chirality that shows up only at the specific LUMO energy. Such chiral behavior has been reported for CuPc/Ag(100) for single CuPc molecules and in the CuPc self-assembly as well. The asymmetric charge transfer between the molecules and the substrate is reported to induce this chirality.[159]

4.5   Handedness of the Energy Specific Chirality
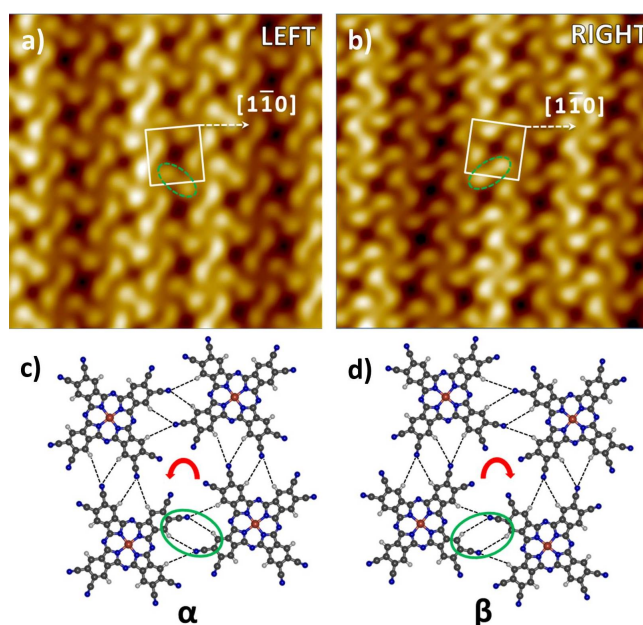
FIGURE 4.6: STM images of CuPc(CN)$_8$ on Au(111). Images a and b (10 nm × 10 nm) are taken at the LUMO energy of 2.0 V, I = 0.2 nA. They are labeled LEFT and RIGHT due to their chirality. (c, d) Illustrations of the tetrameric assembly. Chiral directions are indicated by the red solid arrows. Black dotted lines denote hydrogen bonding. Green solid ovals represent the antiparallel dipolar coupling that gives higher contrast in STM images at LUMO energy.

As the supramolecular self-assembly of CuPc(CN)$_8$ on Au(111) becomes chiral at LUMO energy, handedness emerges. The enantiomeric configurations α and β exhibit left- and right-handed chirality at LUMO energy. Shown in Figure 4.6a,b are the STM images taken with bias voltage 2.0 V, the LUMO energy. Schematic tetrameric unit cells are shown in Figure 4.6c,d. The organizational chirality, which is seen independent of bias voltages, as discussed after Figure 4.2, is present in the images in Figure 4.6 a,b also. But the emergence of handedness at LUMO energy is

an unprecedented observation. This is explained by use of the ball-and-stick model of $CuPc(CN)_8$ shown in Figure 4.6c,d. For the α configuration, the green oval in Figure 4.6c is a schematic representation of the antiparallel dipolar coupling between the nearest-neighbor cyano groups. This coupling is shown by the white dotted oval in the STM image (Figure 4.6a) of the α configuration. This explains the left-handed chirality seen in the STM image. Similarly, for the β configuration, the green oval in Figure 4.6d represents the antiparallel dipolar coupling between the nearest-neighbor -CN groups, reflected in the white dotted oval in the STM image (Figure 4.6b) of the β configuration. This explains the right-handed chirality observed in the STM image.

The STM images (Figure 4.6a,b) reveal that the region between the two lobes involved in the antiparallel dipolar coupling becomes bright. In both configurations, each molecule has four such antiparallel dipolar coupling interactions involved with each lobe. The direction of the anti parallel dipolar coupling interactions are exactly opposite for configurations α and β(marked with green oval). The organizational chirality uniquely defines the direction of the antiparallel dipolar coupling. This coupling provides the handedness in the electronic chirality in the individual molecule in configurations α and β at LUMO energy. Thus, the electronic and organizational chirality are coupled and are irreversible. Thus we are able to comment, from the sub-molecular resolution of the STM images of the tetrameric unit cell of the $CuPc(CN)_8$ self-assembly on Au(111), that the antiparallel dipolar coupling seems to be the driving force for the observed chirality at LUMO energy in the $CuPc(CN)_8$/Au(111) system. We emphasize that the chirality is turned on only at the LUMO energy, which supports our observation of the weak interaction of $CuPc(CN)_8$ with the Au(111) substrate, thereby underscoring the lack of contribution from the substrate to this unique observation of left- and right-handed chiral assemblies. The intermolecular interaction in the $CuPc(CN)_8$ assembly is augmented by the cyano groups, thus making the cyano substitution of CuPc a clear contributor to this chiral behavior.

4.6 Conclusions

In summary, we have presented an atomic-scale investigation of the influence of cyano substitution of CuPc on its molecular self-assembly. STM images of $CuPc(CN)_8$ on Au(111) showed a self-assembly with a tetrameric unit cell that exhibited adsorption-induced structural chirality and kept the herringbone reconstruction periodicity unperturbed. Monolayer coverage of CuPc on Au(111) also showed tetramers in two mirror-symmetric configurations. But the herringbone reconstruction periodicity was modified. This is indicative of a stronger molecule–substrate interaction in the

CuPc/Au(111) assembly than in the CuPc(CN)$_8$/Au(111) assembly. From the STS measurements, the HOMO–LUMO gap showed a drastic increment from 3.0 eV for the CuPc/Au(111) system to 4.3 eV for the CuPc(CN)$_8$/Au(111) system. We attribute these results to the partial cyanation of CuPc. These experimental findings of herringbone periodicity modification and the variation of the HOMO–LUMO gap were validated by ab initio DFT calculations. The voltage-dependent STM images unveil the orbital-energy-specific chirality of the CuPc(CN)$_8$ molecules and superimpose right and left-handedness on the existing structural chirality within the assembly. However, for CuPc no such energy-dependent chiral behavior was witnessed at any orbital energy. Our work thus presents a strategy to functionalize molecules for preferential interaction among them or with the underlying substrate, thereby enabling surface functionalization and templating for applications in catalysis and gas sensing.

Chapter 5

Molecular Doping Over Topological Insulator Surface

5.1 Topological Insulator

Topological insulator (TI) is a new electronic phase of quantum matter. TIs have a bulk insulating gap in the band structure similar to the ordinary insulator but their surface is endowed with a conducting surface state.[93, 173] This behavior is exactly opposite to an electric wire covered with an insulating coating on the outer surface where the electric conduction is in the bulk and the outer surface is insulating. The other important difference to note is that TI is not a composite of two different materials. The same material behaves differently in the bulk and on the surface. The origin of such electrically conducting surface state is mainly due to the intrinsic strong spin-orbit coupling and time reversal symmetry. Electrical insulator and conductor are the
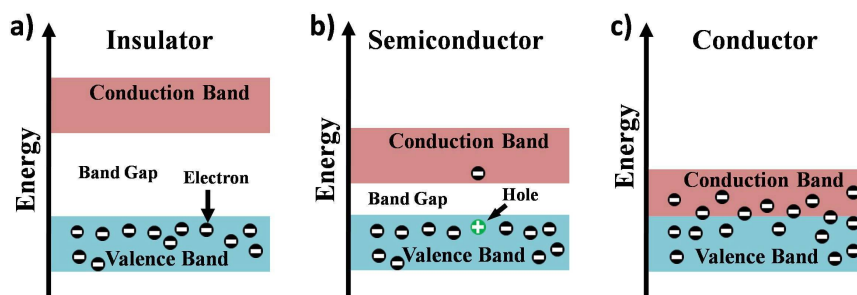
FIGURE 5.1: Schematic band diagram of a) Insulator, b) Semiconductor and c) Conductor

two basic electronic phases of matter having a large band gap and a conductor having an overlap in between the conduction and valence band. More interesting phase of matter discovered later is the semiconductor where the gap between the two band is lower than that of insulators and the electrical conduction can be due to electrons and holes. An exotic phase of matter is called superconductor where the electrical

conduction faces literally zero resistance in some systems due to electron-phonon interaction. These three phases of matter have a common mode of charge carrier transport inside the material and that depends only on the charge of the carrier. Certain peculiarities were seen in materials like Mott insulator, which should conduct electricity according to the band theory but acts as an insulator without any gap in the band structure.[174, 175] To explain such behavior in 1960s Kohn came up with a new characterization of insulating state .[176] This characterization includes both normal insulating phase and Mott insulator. In Kohn's characterization electron in an insulator was treated as occupying localized orbitals which are insensitive to the perturbation on the boundary(Figure 5.2 a). Despite the presence of bulk energy gap
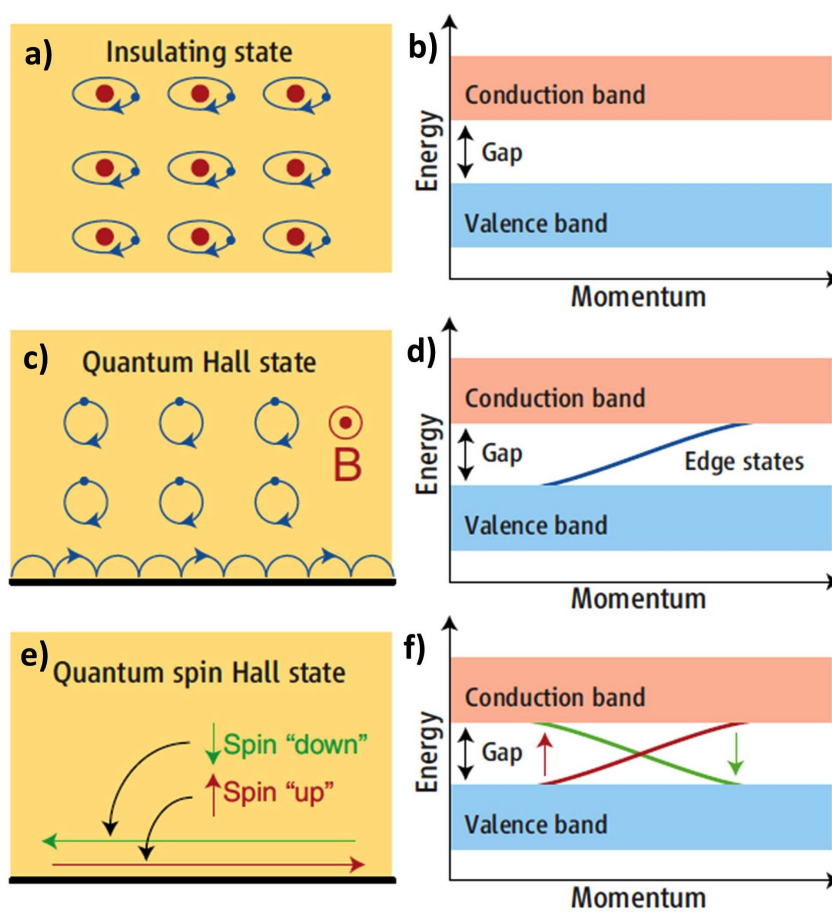
FIGURE 5.2: a) Insulating state where eleectron are bound to the localized orbital. b) corresponding band diagram c) Quantum hall state in the bulk electrons are in localized orbital motion but conducting state available due to the skipping orbital motion at the boundary. d) Corresponding edge state appear in the energy gap. Picture adapted from ref [177]

certain conducting states can be possible under some external field or due to the intrinsic properties of the material as discussed by Charles L. Kane and Eugene J Mele

in "A new Spin on the Insulating state"[177] and Joel Moore in "The birth of Topological Insulator" [178]. The simplest example is the "quantum hall effect" when a magnetic field is applied perpendicular to the two dimensional electron gas. Due to the perpendicular magnetic field electrons experience a perpendicular Lorentz force resulting in circular orbital motion around the magnetic field lines(5.2 c), similar to electron's motion around an atom in an insulator. Quantum mechanics explains that an energy gap is a result of the quantization of electron energy due to this orbital motion. These quantized energy levels are called Landau levels. Basically for a quantum hall system the bulk behaves as an insulator where the electron is bound to the circular orbital motion and cannot conduct electricity. But the interesting thing happens at the boundary. At the boundary electrons execute skipping orbital motion (Figure 5.2 c) that results in a conducting state along the boundary which is known as the edge state as shown in Figure 5.2 d. This edge state lets the charge flow only in one direction. The direction of charge flow can be reversed by reversing the direction of the magnetic field. Such conducting edge states can also be realized
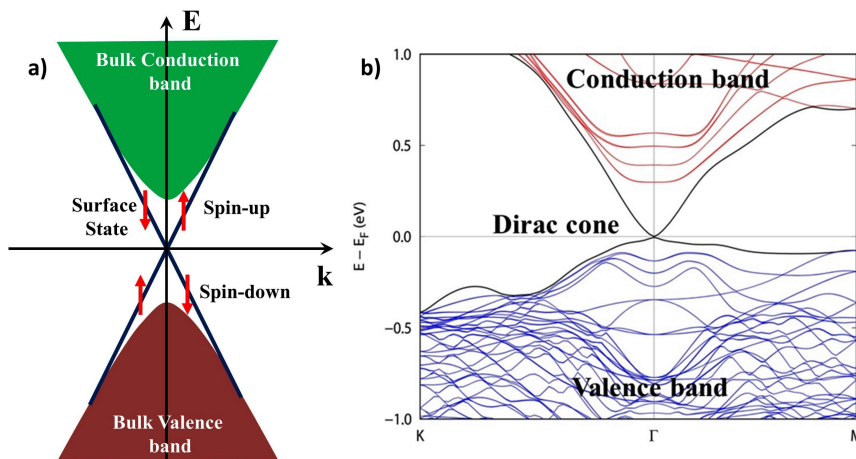
FIGURE 5.3: a) Schematic of Dirac cone-like dispersion in the bulk gap and spin-polarized surface state. b) Theoretically calculated band structure of Bi_2Se_3 topological insulator where Dirac cone is clearly visible in the bulk gap.

without a magnetic field but with strong intrinsic spin-orbit coupling in the material. This effect is known as quantum spin hall effect[179, 180] and the material is known as a two dimensional topological insulator(TI). In this case the spin-orbit coupling which is basically the interaction between the electron spin angular momentum and the orbital angular momentum leads to the spin up movement in one direction and spin down in the opposite direction as shown in Figure 5.2 e. The corresponding band structure is shown in the Figure 5.2 f. The edges are spin polarized and are insensitive to the defects at the boundary [177].Time reversal symmetry also plays

a very crucial role in such systems to make this spin-polarized conducting state robust. Time reversal symmetry simultaneously reverses the direction of propagation and the direction of spin leads to interchanging this counter propagating conducting state. Similar spin-polarized conducting state can also be possible for 3D materials having strong spin-orbit coupling. But in this case the motion of the electron will be in a 2D plane which is the surface of a 3D material. In case of 3D topological insulator inspite of a bulk band gap, conducting surface states are observed to form a Dirac cone-like dispersion in the gap as shown in Figure 5.3a. Similar to the one dimensional edge state, these surface states are very robust against the defects and any nonmagnetic impurities over the surface. The back scattering is also prohibited due to the time reversal symmetry.

The first experimentally discovered 2D quantum hall system is the sandwich of a thin layer of mercury telluride (HgTe) in between mercury cadmium telluride($Hg_xCd_{1-x}Te$) thin layers.[179]. The first experimental observation of 3D topological insulator was reported in the semiconducting alloy $Bi_{1-x}Sb_x$ using angle resolved photoemission spectroscopy (ARPES) in 2008 [181]. The band structure of $Bi_{1-x}Sb_x$ is complicated and difficult to identify the topological signature easily. Later Bi_2Se_3, Bi_2Te_3 and Sb_2Te_3 were recognized as 3D topological insulators with a large band gap reported by several groups.[80, 182–184]. All these three materials possess a single Dirac cone-like surface state together with the bulk band gap. The position of Dirac point is exactly in the middle of the bulk band gap (Figure 5.3 b) in Bi_2Se_3 which makes it easy to identify in ARPES and STM experiments . The large band gap of 0.3eV($\sim$3600K) makes Bi_2Se_3 the most promising TI for room temperature applications.

5.2   Doping Bi_2Se_3 Surface With Molecules

5.2.1   Introduction

As discussed in section 5.1 topological insulators (TIs) are endowed with an insulating bulk and unique metallic surface states. These surface states exhibit a Dirac cone-like dispersion similar to graphene and are topologically protected by time reversal symmetry[93, 178, 182–184]. The strong spin-orbit coupling in these surface states couples the spin degree of freedom with the momentum making the surface states immune to back scattering[185]. Thus the electron transport becomes spin-polarized. This makes the TIs promising candidates for the field spintronics and quantum computing. A guided manipulation of such surface states can lead to exploration of new exotic physical properties like unconventional superconductivity,[186]

Majorana bound state,[187] spin transport and torque devices,[25, 188, 189] fault tolerant quantum computing[190]. Quasiparticle scattering phenomena in topological insulator surface state of Bi$_2$Se$_3$ off defects probed by STM and STS have revealed the robust symmetry protection of TI surface state [191]. Though the non-magnetic metal doping doesn't affect the surface state, doping with magnetic metal atom [192, 193] or metal-organic complex [194] is observed to disrupt the surface state by breaking the time reversal symmetry and opening a gap at the Dirac point. Similar gap opening also observed due to the out-of-plane anisotropy of the magnetic moments of Fe. [195] The gap opening at the Dirac point is also explained by the observation of band bending and quantization of valence and conduction band for carbon monoxide adsorption over Bi$_2$Se$_3$.[196] Other recent experiments with magnetic doping have established the robustness of the surface state and no gap opening was observed.[197–199] The gap opening can only happen when there is sufficiently strong local magnetic moment or any magnetic ordering over the surface. This robustness of surface state is the necessary condition for forming a hybrid interface between metal atoms/metal-organic molecules and topological insulator surface. The hybrid interface can lead us to design new class of spintronics materials by tailoring the electronic properties of TI.[200–202] Metal Phthalocyanines (MPc) are the most promising and well studied organic molecules which host a transition metal ion with partially filled d orbitals at their center. These molecules are already characterized with their excellent electronic properties[203], giant magnetoresistance[204], spin doping[205] and high spin relaxation.[206] On Bi$_2$Te$_3$ surface, also known for its TI properties, different Pc molecules form a well ordered self-assembly depending on the interaction strength of the center metal atom and TI surface, thereby enabling the tailoring of the electronic and magnetic properties of the Pc-TI heterointerface[207]. A strong hybridization between molecular orbitals and substrate is observed in case of MnPc on Bi$_2$Te$_3$[208]. An in-plane magnetic anisotropy is also observed for FePc monolayer over Bi$_2$Te$_3$[209]. All such studies confirm the unaffected topological surface state after doping with organic molecules. The manipulation of TI surface state mainly due to the charge transfer at the interface is evident for MnPc on Bi$_2$Te$_3$[209] and CoPc on Bi$_2$Se$_3$[210]. A recent theoretical and experimental study shows the dependence of electronic properties on the hybridization strength for organic -TI interface and Rashba-split interface state can arise for strong hybridization[211].

5.2.2 Structure of Bi$_2$Se$_3$ and organic molecules

Bi$_2$Se$_3$ has rhombohedral crystal structure and belongs to the $R\overline{3}m$ space group. Each unit cell consists of total five atomic layers as shown in Figure 5.4 a and an alternating
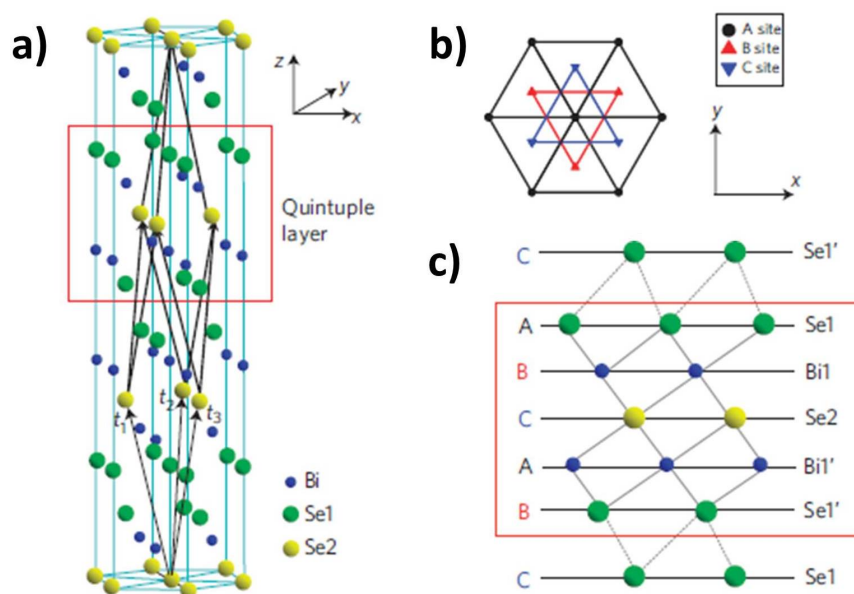
FIGURE 5.4: a) Rhombohedral crystal structure of Bi_2Se_3. b) Top view along the z-direction. The triangle lattice in one quintuple layer has three different positions, denoted as A, B and C. c) Side view of the quintuple layer structure. Along the z-direction, five consecutive layer Se-Bi-Se-Bi-Se in the red rectangle is called Quintuple layer. Bi_2Se_3 is consist of repeated stacking of quintuple layer. Picture source [182]

layer stacking of Bi and Se atoms. Figure 5.4 b represents the position of Bi and Se atom within each layer in the xy plane.

From the side view it is clearly seen that there is a five atomic layer unit consisting of Se-Bi-Se-Bi-Se layer, called Quintuple Layer(QL) as shown in Figure 5.4 c by red rectangle. Inside the QL the atoms are bound with strong covalent interaction(Se-Bi and Bi-Se) but the interaction between two QL which is the interaction between two Se atoms is weak Van der Waals interaction. So this material can be easily exfoliated similar to the mechanical exfoliation technique used for obtaining graphene from graphite (K. S. Novoselov, A. K. Geim, S. V. Morozov, D. Jiang, Y. Zhang, S. V. Dubonos, I. V. Grigorieva, A. A. Firsov Science 306 666 (2004)). Exfoliation exposes the Se hexagonal plane perpendicular to the z-axis as the top surface. In our experiment we have used the scotch tape to cleave Bi_2Se_3 inside the UHV chamber. After cleaving the surface is imaged with STM and it shows Se atoms of the topmost layer arranged in a regular hexagonal array as shown in Figure 5.5c The molecular structure of iron- phthalocyanine molecule (FePc) and copper-phthalocyanine (CuPc) is shown in Figure 5.5 a and b respectively. The only difference between these two molecules is central metal ion which has different 3d orbital filling. FePc has total 6 electrons in its 3d orbital with half filled d_{z^2} orbital which is perpendicular to the
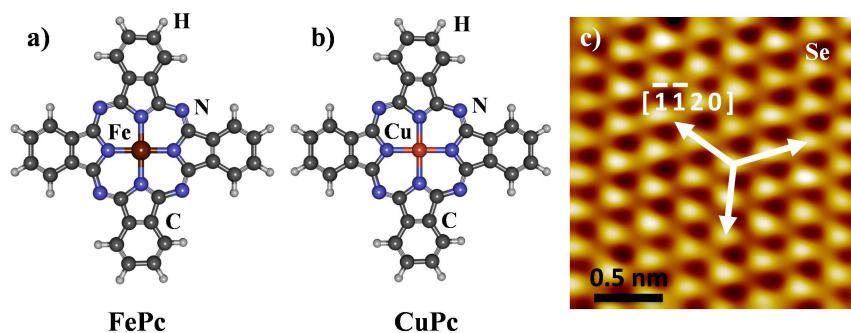
FIGURE 5.5: Molecular structure of a) FePc and b) CuPc. c) STM image of Bi$_2$Se$_3$ cleaved surface showing Se atoms and crystallographic directions.

molecular plane whereas CuPc has total 9 electrons in 3d orbital and d$_{z^2}$ is fully occupied. Due to this difference in the central metal ions the molecules can participate in different interactions with the substrate. The STM image of the substrate is shown in Figure 5.5c where three equivalent crystallographic directions are marked with white arrow. One of them is denoted with $[\bar{1}\bar{1}20]$. In this chapter and the following chapter (chapter 6) we will use this direction to determine the relative orientation of the molecule with respect to the substrate.

The work presented in this chapter concerns the effect of doping the Bi$_2$Se$_3$ surface with magnetic molecules FePc and CuPc. Given the diverse reports of magnetic atom doping on Bi$_2$Se$_3$ [192, 193, 195–199]. We would like to explore the interaction of an organic molecule with TI surface by depositing FePc and CuPc on Bi$_2$Se$_3$. Our investigation is focused on the 3d orbital dependent adsorption behavior of FePc and CuPc and bidirectional influence on the electronic properties of both substrate and molecule due to the molecule-substrate interaction and charge transfer in the molecule-substrate interface along with the effect of the interactions of ligands with the Bi$_2$Se$_3$ surface.

5.2.3 Adsorption behavior of iron-phthalocyanine(FePc)

FePc molecules were deposited on a clean Bi$_2$Se$_3$ surface at room temperature(see experimental section 2.4.4). Figure 5.6 a shows an STM image of FePc molecules after deposition on the Bi$_2$Se$_3$ surface at 77K. FePc molecules were not seen to form self-assembly, rather molecules were seen as individual entities or more than one molecule aggregating together. The typical 4-lobe Pc structure, a characteristic of the square planar, D$_{4h}$ symmetry of the molecule can be easily identified. Also the center of the molecule is seen raised as a bright protrusion in the center. We refer to this configuration as phase A - raised 4-lobe. In a cluster of molecules, a piling of

Before Annealing   **After Annealing**
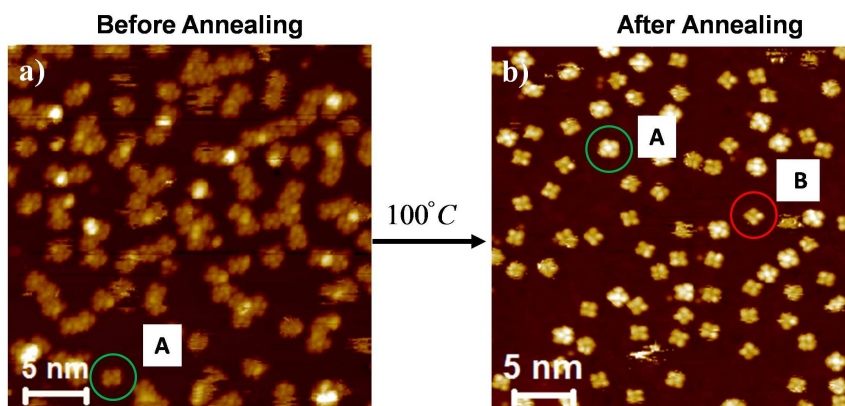
FIGURE 5.6: (a) STM image of FePc molecules adsorbed on Bi_2Se_3 is shown . Only one phase of molecules is seen prior to annealing where the center of the molecule is visible as a bright blob, referred to as phase A and marked by a green circle. (b) Upon annealing the molecules are seen in 2 phases, phase A and phase B, marked by red circles in (b). Phase B has a hollow center unlike phase A which has a bright blob in the center. For both images V = 2.2 V, I = 80 pA.

molecules atop the cluster is also observed, the bright spot in the STM image(Figure 5.6 a). Thus the molecular recognition of FePc is straight forward and is similar to that of FePc on other substrates like Au(111) [212, 213], Pb(111) [214], Ag(110) [215] Cu(111) [216] and on 2D materials like graphene and hexagonal boron nitride(hBN) [217]. Not forming a self-assembly implies that the molecule-substrate interaction is more than the intermolecular interaction and molecules over Bi_2Se_3 have very less diffusion energy. To recognize other possible adsorption configurations and whether FePc can form self-assembly by increasing the kinetic energy of the molecules over the surface we annealed the sample. Annealing at a certain temperature provides external energy to enhance the kinetic energy of the physisorbed molecules so that they can diffuse to the other possible adsorption sites. The striking observation after annealing the sample at 100° C, is that apart from the phase A (Figure 5.6 a) before annealing, molecules adsorb with another conformation. This conformation is completely different from the phase A. Apart from the raised 4-lobe structure as defined earlier they can also be seen in the new configuration where the center appears hollow, we call it phase B - the hollow 4-lobe structure marked with red circle in Figure 5.6 b. The STM image in Figure 5.6 b clearly reflects that the phase B has a different symmetry with respect to the conventional 4-fold symmetry of FePc observed on other metallic substrate. Symmetry reduction in MPcs has been reported in case of low temperature deposition[216]. In our case we believe that phase B is the next lowest energy configuration of FePc on Bi_2Se_3 as it was observed after annealing the sample. Here the fact that we see phase B after annealing could
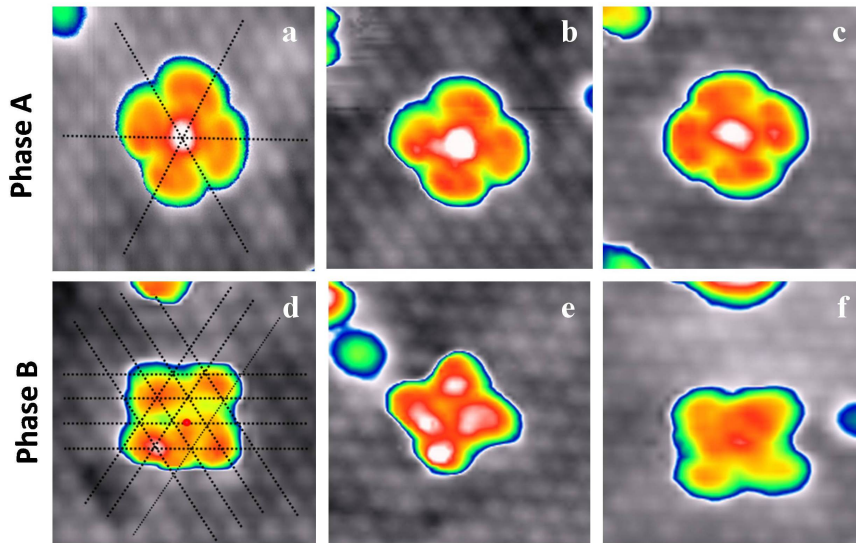
FIGURE 5.7: (a-c) STM image of single FePc molecule of phase A with surface Se atoms in background showing on top adsorption.(d-f) Similar background Se atom resolved single molecule image of phase B showing bridge site adsorption.

be due to the energetic affinity of the different sites of the Se lattice for the Fe atom. Atomic registry of the adsorbed molecules can be determined by using single atoms adsorbed on the surface as shown for the sexiphenyl molecules on Ag(111) [218] or by referring to the atomic resolution of the surface as in case of MPc molecules on Bi$_2$Te$_3$ which is another TI surface. [207, 208]. In our case, we acquired high resolution image of a single FePc molecule, both in phase A and in phase B, with Se atoms in the background as shown in Figure 5.7. To get the registry of the FePc molecule with respect to the Se lattice dotted lines were drawn along the three equivalent Se atoms close-packed directions (as shown in Figure 5.5 c . The point of intersection of these lines is the Se atom. The center of FePc molecule can be clearly seen at the intersection (Figure 5.7 a) implying that FePc is adsorbed on top of an Se atom. Three such STM images with phase A are shown in Figure 5.7 a,b and c and it is clearly observed that this irrespective of molecular orientation, molecules are always sitting on the top of Se atom. In Figure 5.7 d, e and f are closeup STM images of FePc molecules in phase B. Again, drawing the same Se close-packed directions, we see that in this phase B the central Fe atom in FePc molecule is adsorbed on the bridge site, which is the location between 2 nearest neighbor Se atoms. This adsorption is also independent of molecular orientation. The topological surface state(TSS) of Bi$_2$Se$_3$, known to open a gap by Fe atom deposition [192, 195], was then probed with STS measurements. These measurements were done close to the Fermi surface to see if the Bi$_2$Se$_3$ surface before doping with FePc molecules showed any change
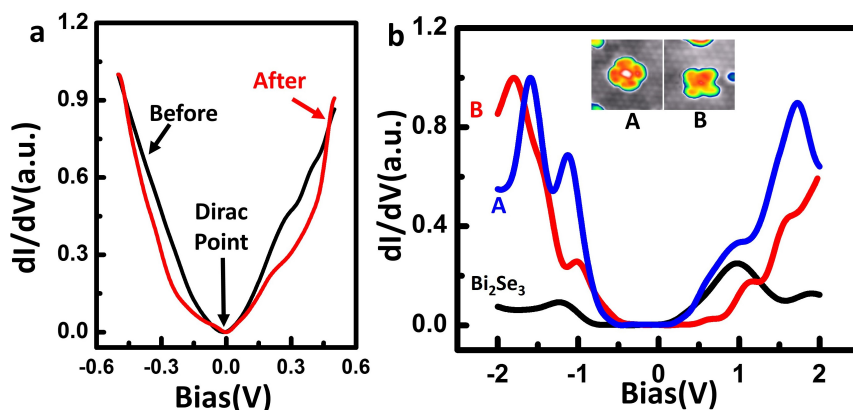
FIGURE 5.8: Point spectroscopy (STS) data (a)for doped and undoped Bi_2Se_3 surface . The undoped Bi_2Se_3 surface shows the Dirac point at the Fermi energy (Ef), black/circle trace. The position of the Dirac point remains unchanged after the doping of the Bi_2Se_3 surface with FePc molecules. (b) STS point spectroscopy over bare Bi_2Se_3 surface is shown by the black trace, with states seen at -1.2 eV and 0.9 eV. The blue trace is the STS data for FePc molecule in phase A (residing on the top site of the Bi_2Se_3 surface). The red trace is STS data for FePc molecule in phase B (residing on the bridge site of the Bi_2Se_3 surface). The electronic states for phase A at negative bias are slightly shifted towards Fermi energy. Inset showing the STM images of two phase A and B

after the doping. An expected change is either a band gap opening as seen in some results of Fe on Bi2Se3[192, 195] or a charge transfer process as seen in CoPc on Bi2Se3 [210]. A charge transfer resulting in the shift of the Dirac point was also seen in the case of MnPc on Bi_2Se_3 [207]. For the FePc doped Bi_2Se_3 surface the STS data showed no change in the position of the Dirac point. The black curve in Figure 5.8 a shows the dI/dV spectrum taken on the bare Bi_2Se_3 surface, and the red curve shows the dI/dV curve taken after FePc molecule deposition over the surface. The Dirac point remains fixed at the Fermi energy. This indicates that there is no contribution from the magnetic Fe atom of FePc to perturb the topological surface state of Bi_2Se_3. Thus this magnetic phthalocyanine-TI interface keeps the surface state intact. No gap opening is observed. Also there is no effective charge transfer between the molecule and the substrate unlike the MnPc/Bi_2Te_3 system where the charge transfer that manifests as a shift of the Dirac point has been attributed to the band bending of Bi_2Te_3 caused by the molecule doping.[208] while with other molecules like CuPc and CoPc no shift is observed [207]. Comparing this with the ARPES study of CoPc on Bi_2Se_3 [210] that shows charge transfer, and ARPES study of 2H-Pc on Bi_2Se_3 where the topological surface state is protected, we see that the central metal atom upon adsorption on the TI surface does influence its interaction

with the exotic surface state of the TI. STS measurements were performed to observe the electronic state for both site selective phases A and B of FePc on Bi$_2$Se$_3$. STS spectra were taken at the center of the molecule in each case. Figure 5.8 b represents the STS spectra for phase A (blue curve) , phase B (red curve) and bare Bi$_2$Se$_3$ (black curve). The Bi$_2$Se$_3$ states are observed at -1.2 eV and at 0.9 V. The Bi$_2$Se$_3$ states are likely to arise from the bulk Bi$_2$Se$_3$ states based on the calculated bulk band structure for Bi$_2$Se$_3$ [219]. For single FePc molecules on the Bi$_2$Se$_3$ substrate,we observe that for FePc phase A and phase B the spectra looks almost similar. For FePc phase A the peak at -1.1 V and 1.0 V and for FePc phase B peak at -1.0 V and at 1.1 V are close to the reported values by other groups. The HOMO and LUMO values of FePc are close to the reported values by other groups [220]. The electronic state at positive bias for both these phases A and B are almost in the same position. But the electronic state for phase A in the negative bias are slightly shifted towards the Fermi energy than the phase B. This could be due to the site dependence of the FePc molecules. A theoretical insight from DFT calculations would be helpful to understand these shifts better.

5.2.4 Energetic tuning of Dirac point and symmetry reduction of CuPc

CuPc, an organic semiconductor, with its ease of availability and amenability to modifications, is a potential choice for organic spintronic devices. Particularly useful is its long spin relaxation time[206], optoelectronic application[221] and exchange interaction[222]. Combining these attributes of CuPc with the backscattering-immune traits of the topological insulator Bi$_2$Se$_3$ is a worthwhile strategy to pursue for upcoming quantum technologies. The chemical structure of CuPc is shown in Figure 5.5 b. The adsorption behavior of molecules over solid surfaces strongly depends on the fine tuning between the molecule-substrate interfacial interaction and intermolecular interaction. Most of the 2D planar molecules like phthalocyanine lie flat over the substrate for having the maximum overlap between substrate electronic state and molecular orbitals[81]. But they can also show tilted adsorption at mono atomic step edge[223] and upright configuration in the second layer when the molecules in the second layer are decoupled from the substrate owing to the molecule-substrate interaction of the first molecular layer formed by the same molecules [224] or thin insulating layer [225]. Figure 5.9 a shows the STM image of CuPc molecules over Bi$_2$Se$_3$ at a very dilute concentration where CuPc molecules are evaporated thermally on to the Bi$_2$Se$_3$ substrate held at room temperature. CuPc molecules are seen to be dispersed over the whole surface. The inset shows the molecular structure of CuPc
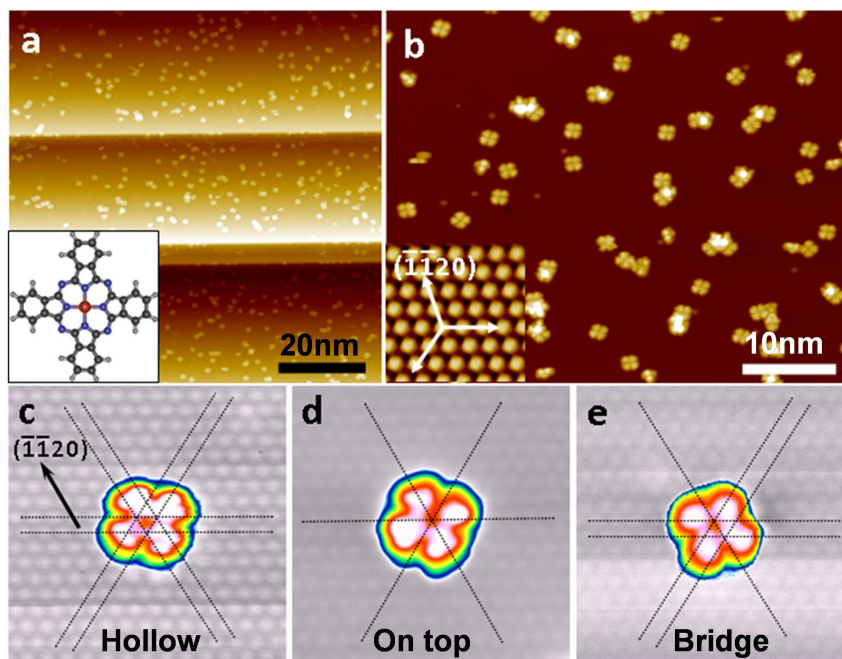
FIGURE 5.9: (a) STM image showing CuPc molecules at dilute con-
centration scattered on Bi_2Se_3 surface. (b) A closer look at the ad-
sorbed CuPc molecules, the inset shows the Se atoms of Bi_2Se_3
surface and the crystallographic directions(white arrows).I= 0.2 nA,
V=-1.6 V (c)-(e) show the site-specific resolution of a single CuPc
molecule, hollow site, top site, bridge site respectively with the reg-
istry of Se atoms in the background, I= 0.2nA, V=-1.6 V (Image size
5 nm X 5 nm)

where Cu atom is located at its center. The 4-lobe configuration is a known character-
istic of the planar MPc molecules. Individual CuPc molecules with 4-lobe structure
can be seen in the zoomed-in STM image in Figure 5.9 b with the inset showing
the Se atoms over the surface. The arrows represent three equivalent close-packed
directions of the surface. The three equivalent orientations of the 4-fold CuPc are ob-
served with respect to the 6-fold (0001) plane of Bi_2Se_3. In each orientation the two
lobes are along one of the close-packed Se direction$[\bar{1}\bar{1}20]$ and the other two lobes are
oriented along $[1\bar{1}00]$ crystallographic direction of the substrate. The STM images of
CuPc molecules with atomically resolved Se lattice in background reveal the differ-
ent adsorption sites of the central Cu atom of CuPc. It sits on the hollow site between
3 Se atoms (Figure 5.9 c), on top of Se atom (Figure 5.9 d), and on the bridge site
between 2 Se atoms (Figure 5.9 e). Such images are a direct real space tool for an un-
ambiguous determination of the adsorption site of the CuPc molecule on the Bi_2Se_3
surface. Though the molecule sits on a different site the orientational preference of
the molecule remains same where one pair of opposite lobes is always directed along
the close-packed Se atoms $[\bar{1}\bar{1}20]$ direction. This indicates a strong interaction of the

ligand with the substrate to pin the orientation of the molecule. In contrast to the earlier study of different MPcs on Bi$_2$Te$_3$ surface the only adsorption site observed is on top[207, 208]. But FePc on Bi$_2$Te$_3$ is observed to adsorb on both bridge and top sites[209]. Such an orientational preference provides a symmetry mismatch between 4-fold molecule on a 6-fold substrate and creates a non-identical environment for the isoindole groups of the molecule and can induce a geometrical distortion in the molecule. A similar effect has been seen in MnPc over Bi$_2$Te$_3$[208] but despite similar orientation of CuPc and CoPc on Bi$_2$Te$_3$ no geometrical distortion and symmetry reduction like MnPc has been reported[207]. In our investigation of CuPc/Bi$_2$Se$_3$ hy-
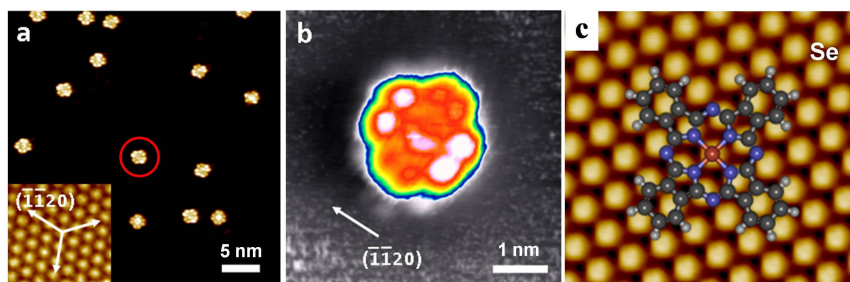
FIGURE 5.10: (a) STM image of isolated CuPc molecules on Bi$_2$Se$_3$ surface at 1.8 V and 0.2 nA (b) A closer look at the symmetry reduced single CuPc molecule, the 8-lobe structure V= 1.8 V , I= 0.2 nA. (c) A ball and stick model of CuPc is superimposed with real space STM image of bare Bi$_2$Se$_3$ to understand the asymmetric underneath atomic environment of the molecular ligands.

brid interface the effect of ligand substrate interaction is clearly visible in the STM image recorded at the positive bias. More interestingly a reduction of 4-fold molecular symmetry to 2- fold is observed. The STM image in Figure 5.10 a is recorded at 1.8 V and 0.2 nA and it is evident from the image that two lobes along the [$\bar{1}\bar{1}20$] direction appear as bright in contrast to the other two lobes which are perpendicular to the [$\bar{1}\bar{1}20$] direction and appear dark in contrast. This reduces the symmetry of CuPc from C$_4$ to C$_2$. This symmetry reduction is more evident in the single molecule image as shown Figure 5.10 b. Such symmetry reduction of CuPc has been observed before on metal surfaces Ag(110)[226] and Cu(111)[216, 227]. The origin of this symmetry reduction is attributed to the underneath non-equivalent atomic environment which induces an asymmetric molecule-substrate interaction between the lobes oriented along the close-packed Se direction and in the perpendicular direction. For a better understanding of this underneath asymmetric atomic environment we have superimposed a ball and stick model of CuPc over a atomically resolved Se surface as shown in Figure 5.10 c. It is clearly observed that molecular lobes which are along the crystallographic [$\bar{1}\bar{1}20$] are sitting over the the closed pack Se atom whereas lobes

perpendicular to the $[\bar{1}\bar{1}20]$ are sitting on a different atomic environment. As it is described in case of CoPc on Cu(111)[228] two lobes along $[1\bar{1}0]$ direction interact more with the substrate effecting a bending towards the substrate and appear darker in STM image. We observe a similar effect for the CuPc lobes perpendicular to $[\bar{1}\bar{1}20]$ direction of Bi_2Se_3. They interact more with the substrate and bend towards the substrate and appear dark while the other two lobes along the close-packed direction appear bright. We believe that the central Cu atom does not play a crucial
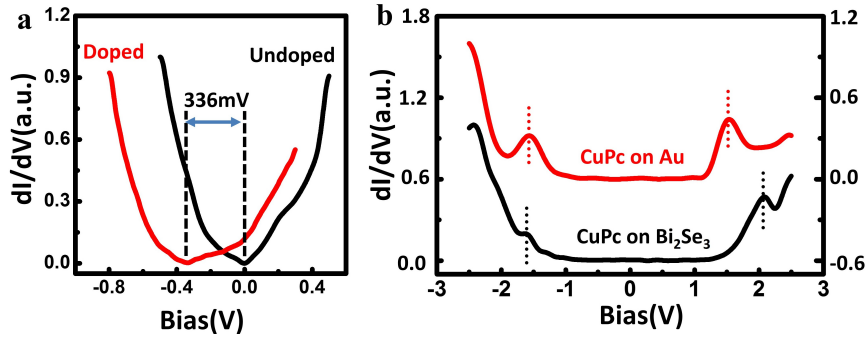
FIGURE 5.11: a)STS spectra of doped and undoped Bi_2Se_3 surface. The Dirac point can be seen at E_F in the pristine Bi_2Se_3 but upon CuPc doping it is shifted to -336 mV.(b)HOMO and LUMO levels of CuPc on Bi_2Se_3 surface and on Au(111) surface. The set point for CuPc/Au(111) is 1.4 V, 0.2 nA and for CuPc/Bi_2Se_3 is 1.8 V, 0.4 nA. The CuPc/Au(111) is shifted vertically for clarity.

role as its d_{z^2} orbital is fully occupied. The weak interaction of central Cu atom has been observed on several metal substrates, also on Bi_2Te_3. Despite similar orientational preference of CuPc on Bi_2Te_3 at dilute concentration no symmetry reduction is observed[207]. The symmetry reduction of CuPc over Bi_2Se_3 strongly depends on the asymmetric hybridization of the ligand with the substrate. To study the effect of such hybridization of the CuPc/Bi_2Se_3 interface in charge distribution and in electronic properties we investigated the local density of states(LDOS) by STS. Our STS measurements for Bi_2Se_3 surface state before(black curve) and after CuPc doping(red curve) are shown in Figure 5.11 a. A clear downward shift of Dirac point of 336mV to the negative bias is observed after CuPc doping. This shift in Dirac point is attributed to the charge transfer in the interface. Such a shift is previously observed in several molecule-TI interfaces[207, 210] and transition metal doping studies over Bi_2Se_3 [199, 229]. In case of CoPc on Bi_2Se_3 this shift in Dirac point is observed to vary with the molecule coverage on the surface. After 0.66 ML the charge transfer decreases and Dirac point shift starts to decrease. The charge transfer from CuPc leaves it positively charged and in turn makes it electrostatically bound to the Bi_2Se_3 surface with the CuPc/Bi_2Se_3 interface dipole strength. This prohibits any ordered

in-plane self-assembly on the surface even for a coverage more than 1ML as will be discussed later. To assess the effect of hybridization over the molecule we compared CuPc/Bi$_2$Se$_3$ with the CuPc/Au(111). As it is observed from our previous study of CuPc on Au(111) no symmetry reduction is observed in the voltage-dependent STM images. But the HOMO-LUMO gap increment is observed due to the pendant group substitution in CuPc[230]. The HOMO-LUMO gap measurement for CuPc using the STS technique for both Au(111) and Bi$_2$Se$_3$ are shown in Figure 5.11 b. A clear increment in the gap is observed. For CuPc molecules adsorbed on Bi$_2$Se$_3$ the HOMO-LUMO gap was found to be 3.67 eV whereas for CuPc on Au(111) this gap was 3.09 eV. The increment is mostly due to the shift of LUMO going away from the Fermi energy whereas the HOMO is slightly shifted towards negative voltage. A molecule upon adsorption on a substrate encounters electronic screening due to the substrate. This influences the energy levels of the molecule-metal system. For PTCDA [231] molecules, the change in the HOMO-LUMO gap from the isolated PTCDA value of 5.0 eV, occurs as a function of the substrate - for Au(111) it is seen to be the least at 3.1 eV, for graphite it is 3.49 eV, and when a monolayer of transition metal dichalcogenide WSe$_2$ is deposited on graphite the HOMO-LUMO gap changes to 3.73 eV. Thus the effect of screening is pronounced for the metallic Au substrate and it manifests in the reduced HOMO-LUMO gap for PTCDA/Au(111). The HOMO-LUMO gap of PTCDA on WSe$_2$ has been observed to reduce due to the strong charge screening when adsorbed on Au(111)[231]. For CuPc/Bi$_2$Se$_3$ the gap is less on Au(111) due to the metallic nature of the substrate and stronger screening than the bulk insulating Bi$_2$Se$_3$. This highlights the fact that the type of substrate can play a major role in the energy level alignment at the molecule-substrate interface. From the STM images of individual CuPc molecules it is clearly observed that the CuPc molecule at dilute concentration binds reasonably well to the substrate with preferred orientation via the ligand-substrate hybridization and dipole formation due to the interface charge transfer which makes them more steady and stable. So it is expected for the molecule to not form a nice and ordered self-assembly via intermolecular interaction. The strong molecule-substrate interaction plays a role here, and due to the charge transfer from CuPc to Bi$_2$Se$_3$ surface the positively charged CuPc molecules repel each other. To probe the structural evolution of CuPc over Bi$_2$Se$_3$ at higher coverage, Bi$_2$Se$_3$ substrate was exposed for a long time until molecule coverage reached more than 1ML. We don't see any ordered self assembly even after 1ML coverage. Figure 5.12 represents the STM image for CuPc coverage more than 1ML. As seen in Figure 5.12 a, over the flat terrace molecules are sitting on the second layer (bright one) over the flat lying molecules in first layer but no ordered self-assembly can be seen. The step edges nucleate an ordered assembly. Figure 5.12 b represents a zoomed in view
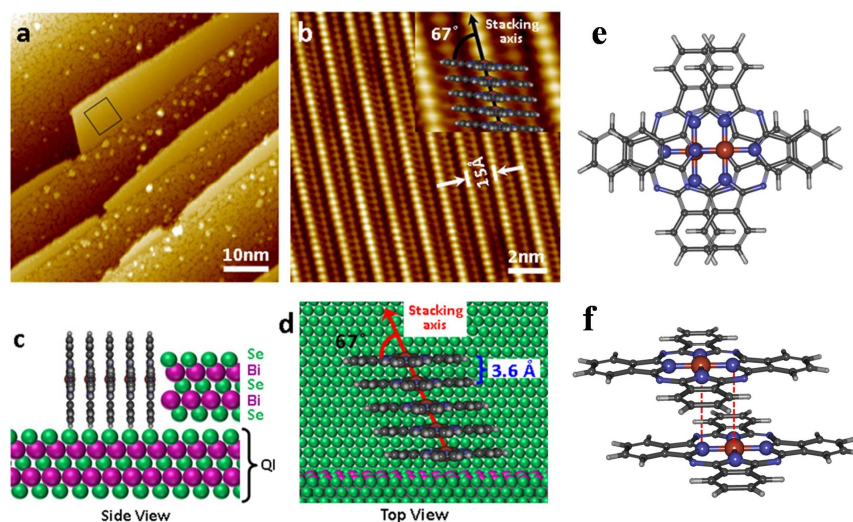
FIGURE 5.12: (a) STM image at higher coverage more than 1ML of CuPc molecules on Bi_2Se_3. Disordered molecules at the terrace but ordered assembly nucleated from the step edge (Scale bar=10 nm). (b) The black square on the self-assembly in (a) is shown in a magnified scale. V=1.8 V I=0.2 nA. Inset showing the superimposed standing-up molecules in the 1D chain. (c-d) Schematic for side and top view of standing up CuPc 1D chain. (e-f) Schematic relative arrangement of two parallel CUPc in 1D chain and their overlap. It is clearly seen that molecules are shifted parallely along the principle axis which is parallel to the surface and central Cu atom is sitting over pyrrole N atom of the nearby molecule.

over the black square area marked in Figure 5.12 a. It reveals 1D chain formation nucleated from the step edge. In this 1D chain CuPc molecules align in standing-up configuration and stack parallel to each other as shown in the inset of Figure 5.12 b. The bright line corresponds to the Cu atom at the center of the molecule. This standing up configuration with a face-to-face alignment has been observed in case of a coverage dependent study of CuPc on Bi(111)[224]. Though there is a strong molecule-substrate interaction for flat-lying CuPc over Bi_2Se_3 this transition from flat-lying to standing-up is due to the lifting of the molecule-substrate interaction for the molecules in the second layer by the first layer. The report for 1.6 ML thin film of CuPc where a tilted adsorption geometry with an upright configuration is seen, is a validation of the intermolecular interaction overpowering the CuPc-Bi(111) inter-action [225]. In another study involving SnPc molecules, where a thin NaCl layer was observed to act as a buffer layer to reduce the molecule-substrate interaction, a similar arrangement was seen upon Au(111) substrate modification. SnPc molecules when deposited on Au(111) form a thin film parallel to the surface in the Stranski-Krastanov mode whereas when a partial layer of NaCl is deposited on Au(111) a decoupling occurs between CuPc and Au(111). SnPc molecules adsorb in a tilted

configuration on the NaCl layer in the Volmer Weber growth mode forming molecular nanocrystals. [225]. For CuPc/Bi$_2$Se$_3$ the first flat-lying layer acts as a buffer layer to reduce the molecule-substrate interaction and molecules coming next opt for a standing up configuration. But we believe that the step edge is playing a major role to nucleate such 1D chain formation as it is only seen to form at the step edge but not on the terrace. Monoatomic step edge on Au(111) is observed to act as a template to assemble molecules along the step edge in a tilted configuration[223]. The step edge of Bi$_2$Se$_3$ is completely different from the monoatomic step edge of a conventional metal. It consists of five atomic layers with alternating Se-Bi-Se-Bi-Se stacking and the height is 9.5 Å [182]. The molecule at the step edge experiences a strong support to adsorbed vertically as the Bi and Se atoms at the step edge have fewer coordination number. Apart from the fully occupied d$_{z^2}$ orbital of Cu atom there are pyrrole and azamethine nitrogen atoms which can interact with the layer stacked Bi atom in the step to make the molecule stable in standing up configuration .The inset of Figure 5.12 b shows that the stacking, the line joining the central Cu atoms of each molecule with respect to the molecular plane, is 67°. The molecules are stacked in parallel but their center is slightly shifted. Such stacking is similar to the well defined cystalline α -phase of the CuPc molecules [232]. Figure 5.12 c shows a side view of the schematic of 1D chain, and Figure 5.12 d shows the top view. The separation between the stacking axis (line joining Cu atoms) i.e the bright lines in STM image in Figure 5.12 b is 15 Å and the separation between two molecules in the 1D chain is 3.6 Å}. That the molecules in the chain are very close to each other reflects the strong intermolecular interaction in standing-up configuration. The multilayer α-phase stacking of CoPc with stacking angle 65.8° has been observed to have strong antiferromagnetism [233]. The mechanism of superexchange in similar stacking of CoPc on Pb(111) has been studied using spin flip spectroscopy and it is observed that such materials can function as versatile toolkits for composing molecule-based magnetic materials[234]. A 1D chain of CuPc with similar stacking is theoretically proposed to have indirect spin exchange[235]. Such 1D chains can be used to design new class of magnetic materials using phthalocyanines. Figure 5.12 e and f represent the stacking of two molecules inside the 1D chain. In the 1D chain the molecules are not stacking with 100 % overlap. Rather molecules are slightly shifted in either direction(left or right) along the molecular principal axis parallel to the surface. The central Cu atom of one molecule is exactly sitting over the pyrrole nitrogen of the nearby molecule, so the Cu atom from two nearby molecules can not participate in direct exchange but they can engage for an indirect exchange interaction via pyrrole nitrogen as shown in Figure 5.12 f. This mechanism is similar to the indirect exchange in case of CoPc layered stacking. [234]

5.2.5   Conclusions

To summarize we have investigated the magnetic phthalocyanine molecules, FePc and CuPc, on Bi_2Se_3 the topological insulator surface. Our investigation reveals the emergent structural and electronic properties of the hybrid interface formed between molecules (FePc and CuPc) and Bi_2Se_3. Individual molecules of FePc were seen to adsorb on top site. But after annealing at 100 ° a few molecules were seen to diffuse to the bridge site of the Bi_2Se_3 surface and appeared with a symmetry reduced phase . Such site-dependent adsorption was determined by concomitant background surface atomic resolution with the adsorbed single molecule resolution. No large scale ordering of FePc was observed on Bi_2Se_3. There is a slight shift of orbitals of FePc based on the adsorption site. The topological surface state of Bi_2Se_3 remains protected after the on surface deposition introduced by the FePc molecules. In case of CuPc on Bi_2Se_3 despite a weak interaction of the fully occupied d_{z^2} orbital with the substrate, CuPc is observed to bind stably with the surface via ligand-substrate interaction and charge transfer in the interface. CuPc orients along one of the close-packed directions of the topmost Se layer. The manipulation of Dirac point from the Fermi energy towards negative energy is observed with CuPc doping but the Dirac surface state remains protected. The STS measurement for HOMO and LUMO orbitals and comparison of HOMO-LUMO gap with CuPc/Au(111) reflects the gap increment mainly due to the shift of LUMO towards the positive voltage. This gap increment is attributed to the reduced screening due to the Bi_2Se_3 surface than the metallic Au(111). At higher coverage CuPc is seen to form a 1D chain with standing-up configuration nucleated from the step edge. Such upright stacking opens up channels for indirect spin exchange. Due to the high spin relaxation of CuPc and the spin dependent transport properties of Bi_2Se_3 such a hybrid interface between CuPc and Bi_2Se_3 can be harnessed for rich spintronics-related phenomena and for new molecule-based designer magnetic materials. Thus our proposed organic molecule-topological insulator hybrid interface awaits application for advances in spintronic devices.

Chapter 6

Resonant tunneling and Negative Differential Resistance in the F_{16}CoPc-Bi_2Se_3 interface

6.1 Introduction

In the year 1974, Aviram and Ratner [32], in a seminal paper, proposed the construction of a recitifier using an organic molecule. Taking hemiquinone molecule as an example they explained that its molecular subunits could act as the elements of a rectifier. The quino (=O) groups on the left could decrease the π electron density and raise the electron affinity acting as the acceptor subunit whereas the methoxy (-OCH3) groups on the right could increase the π electron density and lower the ionization potential acting as donor subunit and the methylene bridge would be the sigma electron system to separate these two subunits. This concept laid the foundation for molecular electronics and led to an intense research in this area with demonstration of conducting molecular wires [236]. An interesting finding in a subsequent molecular device made of Au-alkanethiolate-Au self-assembled monolayers (SAMs) was large on-off ratios and negative differential resistance (NDR) in these devices [237]. A couple of years after this were inundated by several reports of carbon nanotubes acting as transistors, and wiring of molecules into circuits, realized by the advent of the now ubiquitous and indispensable electron beam lithography [238]. The concept of NDR, simply understood as a decrease in current with an increase in voltage through a device, was first observed by Leo Esaki in a tunnel diode [239, 240]. The nonlinear I-V characteristics of a regular p-n junction diode (fig. 2a) get uniquely modified in a tunnel diode (fig. 2f), where the thin depletion layer ($\sim$10 nm) between highly doped p and n regions gives rise to tunneling of electrons and a subsequent NDR effect. In ordinary diode forward bias, the current started to flow when the bias voltage crosses the cut-in voltage as shown in Figure 6.1 a. But the I-V characteristic is different for a tunnel diode. No cut-in voltage is required for the carrier conduction,

electron and hole can tunnel through the narrow depletion region to conduct current. In unbiased condition, due to heavy doping the conduction band of n-region overlap with the valence band of p-region. With increasing temperature the electrons start to tunnel from n-region to p-region and similarly holes tunnel to in the opposite direction. The net current is zero as equal no of electrons and holes flow in the opposite directions (Figure 6.1 b). At very low bias less than the cut-in voltage of the narrow depletion region, a forward current appears due to the tunneling of a conduction band electrons of n-region to the empty state of valence band of p-region through the depletion barrier (Figure 6.1 c). A slight increment in the bias increase the overlap between the conduction and valence band and more no of electrons start to tunnel and current increases. The current reaches the maximum value when the overlap between the conduction band and valence band become maximum with the increasing bias. Figure 6.1 d represent the schematic for maximum current. Upon further increase in the bias there is a decrease in the overlap and the tunneling current starts to decrease as shown in Figure6.1 e. If the applied bias is largely increased, the overlap becomes zero and the current attains a minimum value and the diode then starts to behave as a normal p-n junction diode as shown in Figure 6.1 f. The most interesting feature in the I-V of a tunnel diode is that after the maximum value is reached the current starts to decrease with increasing bias, this phenomenon known as negative differential resistance(NDR) as shown in Figure 6.1 f.

Similar NDR phenomenon has also been observed precisely at atomic scale in STM tunneling junctions in several systems like doped silicon surface [241, 242] and polycrystalline diamond films[243]. Such localized NDR is also observed when selected molecules are placed over the metal/semiconductor substrate in the STM tunneling junction[244–247] or in the molecular self-assembly involving chemical changes in the molecules due to the reaction process[237, 248]. A spin dependent NDR using spin-polarized STM in antiferromagnetically coupled few Fe atom spin chain[249] and vibrationally mediated NDR [250] have also been reported. A detailed understanding of the NDR mechanism can help tune NDR [251, 252]. NDR in STM tunnel junctions has been characterized by the resonant tunneling between two sharp localized energy levels either in occupied or unoccupied states. The resonant tunneling happens between the localized state in STM tip and the surface[241–244]. In such cases NDR appears at any applied bias voltages as the tip apex keep changing with scanning and can disappear if the tip is replaced with a different material[253]. However if resonant tunneling happens between the specific energy level of the adsorbed molecule and the substrate then the effect is independent of the tip and appears at a specific bias magnitude. In case of semiconducting substrate NDR can also appear at a particular bias polarity [245, 251, 252]. For molecular STM
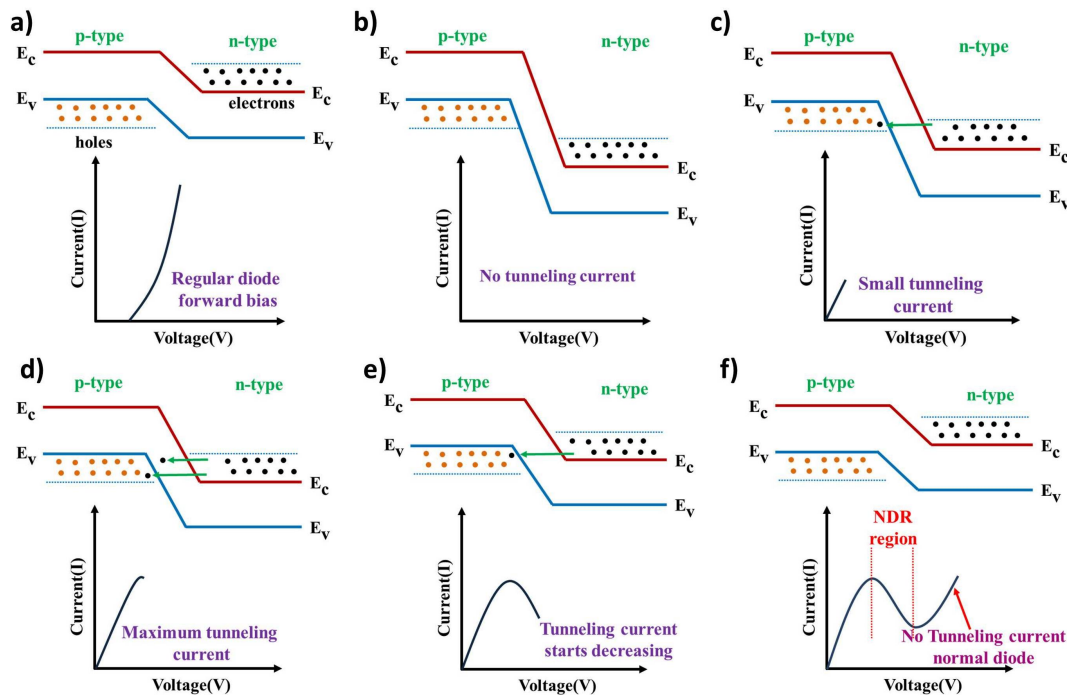
FIGURE 6.1: (a) Forward bias I-V characteristics of a regular p-n junction diode, the current starts to increase after the cut-in voltage. (b-f)Represent the stepwise I-V characteristics of a tunnel diode. (b) At zero bias there is no net tunneling current. (c) When a very small bias is applied electrons from the conduction band of n-region tunnel into the empty states of p-region giving rise to a small current.(d)With increasing bias, the overlap between conduction band and valence band increases and the current also increases. When the conduction band and valence band exactly matches with each other the current attains the maximum value.(e) With further increase in the bias voltage the overlap starts to decrease and the tunneling current also starts to decrease. (f) When the applied bias becomes very large the conduction band and valence band no longer overlap, hence there is no tunneling current. The diode then follows the characteristics of a regular diode.

junction the resonant tunneling is also observed to occur between a specific molecular orbital and the intrinsic surface state of the substrate[254].

In this chapter we report the adsorption behavior of $F_{16}CoPc$ over Bi_2Se_3 surface. This turns out to be a very interesting system for STM and STS studies. In our STS measurement NDR occurs consistently at a particular bias when the STS spectra are taken at the center of the molecule over Co atom. In the self-assembly $F_{16}CoPc$ is observed to form a complete monolayer over Bi_2Se_3 with two different rotational domains and these domains alternate in all directions. Similar to FePc on Bi_2Se_3 discussed in chapter 5, we haven't observed any shift in the Dirac point which means that there is no effective charge transfer from the molecule to the substrate and vice-versa. Previous reports of NDR involving 2,2,6,6-tetramethyl-1-piperidinyloxy and

CoPc molecule demonstrate that the bulk band gap[247] or the gap between the surface states [254] is necessary to observe NDR. When a specific molecular orbital involved in resonant tunneling immediately after the resonance falls into the gap it gives rise to NDR. We decided to investigate the same $F_{16}CoPc$ molecule over Ag(111) metal surface with same set of STM tips to further rule out the tip effect. Interestingly we haven't observed any NDR effect for $F_{16}CoPc$ over Ag(111) surface. We observed a difference in the self-assembly formation though. $F_{16}CoPc$ molecules were observed to form dimer chains along specific crystallographic directions.

6.2   Rotational domain of $F_{16}CoPc$ on Bi_2Se_3

The chemical structure of fluorinated cobalt-phthalocyanine($F_{16}CoPc$) is shown in Figure 6.2. Where the central metal atom is cobalt(Co) and all hydrogen atoms in MPc are substituted with fluorine(F) atoms. Central Co atom has total 7 electrons in the 3d orbital with fully occupied d_{xy},$d_{xz}d_{xy}$, half filled d_{z^2} orbital and unoccupied $d_{x^2-y^2}$ orbital. $F_{16}CoPc$ is slightly different from the FePc and CuPc(as discussed in
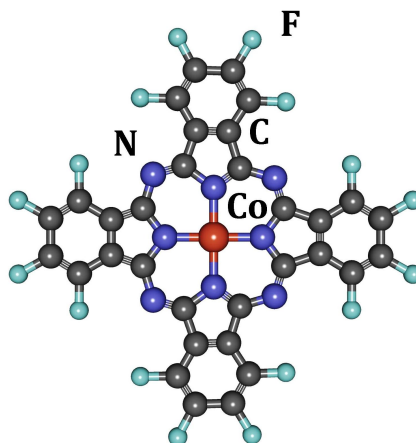
FIGURE 6.2: Chemical structure of $F_{16}CoPc$ where the central metal is Co and outer 16 H atoms were replaced with F atoms

chapter 5) with respect to the 3d orbital filling and the outer F atoms. Due to these two very crucial changes in the chemical structure of the molecule it is expected to observe different molecule-substrate interaction dominated by the central core and the intermolecular interaction provided by F atoms. This effect can reflect in its molecular adsorption and in the electronic properties at the interface. After depositing the $F_{16}CoPc$ molecules on Bi_2Se_3 substrate held at room temperature (see details in the experimental section 2.4.4)the molecules were observed to form nice monolayer assembly as shown in Figure 6.3 a. Where empty space of Bi_2Se_3 is marked with a white arrow. The molecules were seen to adsorb in a flat-lying configuration
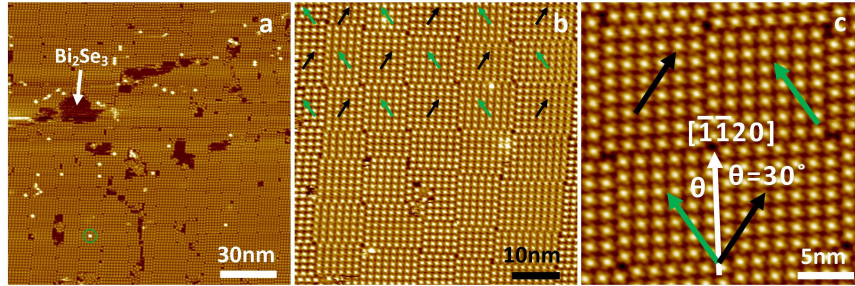
FIGURE 6.3: (a) A large area STM image of F$_{16}$CoPc molecules adsorbed on Bi$_2$Se$_3$ where monolayer coverage of F$_{16}$CoPc with nanometer-sized domains can be seen. The empty space of Bi$_2$Se$_3$ is indicated by white arrow. Few scattered molecules were also observed in the second layer marked with green circle. (b) Zoomed-in STM image where black and green arrows represent the orientation of the molecules in a domain. These specific rotational domains show up in an alternating order in all the four in plane directions. (c) Further zoomed-in image shows individual F$_{16}$CoPc molecules with two orientational preferences $\pm$ 30° with respect to the [$\overline{1}\overline{1}20$] direction. Imaging parameters are V = 1.6 V, I = 100 pA.

parallel to the surface. There are the molecules on the second layer marked by a green circle which adsorb parallel to the molecule in the first layer(discussed later in detail). The nano-domains were clearly seen in the assembly. Further resolved domains are shown in Figure 6.3 b. It is clearly seen that molecules form very small rectangular shape nanometer-size domains. There are mainly two different domains and they are distinguished by the orientation of the molecule in each domain with respect to the substrate crystallographic direction [$\overline{1}\overline{1}20$]. The black and green arrows represent the orientation of the molecule in each domain. Interestingly these domains are arranged in an alternating order in all four directions in the 2D plane over surface as illustrated by the alternating arrangement of black and green arrows in Figure 6.3 b. We haven't seen any domain with mixed orientation of the molecules with respect to the substrate. The domain boundaries are formed due to the different orientation of the molecules. A careful look at the individual molecule resolved in the STM image shown in Figure 6.3 c for the specific orientation of molecules over the Bi$_2$Se$_3$ surface reflects that the two orientations of the molecules are either +30 ° or -30 ° with respect to the [$\overline{1}\overline{1}20$] crystallographic direction. The relative rotation of the 4-fold symmetric molecule on a 6-fold surface leave the molecule in the same configuration with respect to the substrate. So these two orientational configurations of $\pm$ 30° are equivalent to each other and are energetically degenerate to each other with respect to their adsorption energy. Either of these two configurations are equally probable. Any such rotational domain was not observed when F$_{16}$CoPc was deposited on Ag(110)[255] and graphene[256]. In case of F$_{16}$CoPc on Ag(110) two different

well-defined crystalline structures were observed which strongly depend on the inter-row spacing. The main driving force for such monolayer formation seems to be the adsorbate-substrate interaction [255]. On graphene $F_{16}CoPc$ was observed to form a monolayer assembly with an oblique lattice.[256] In our previous study on FePc and CuPc on same substrate Bi_2Se_3(see chapter 5), no self-assembly or ordering was observed. But $F_{16}CoPc$ formed an ordered self-assembly like other phthalocyanines on various metal substrates [255, 256] . This might be due to the modified tuning of the interaction strength between molecule-substrate and intermolecular interaction. Different 3d orbital filling can lead to the self-assembly formation as discussed in case of different phthalocyanines on Bi_2Te_3 where CoPc and CuPc were seen to form a self-assembly but MnPc was not seen to order on the same surface [207]. The addition of F atoms by substituting the H atoms can also enhance the intermolecular interaction which can also a key factor for forming self-assembly [230] . To study the coverage
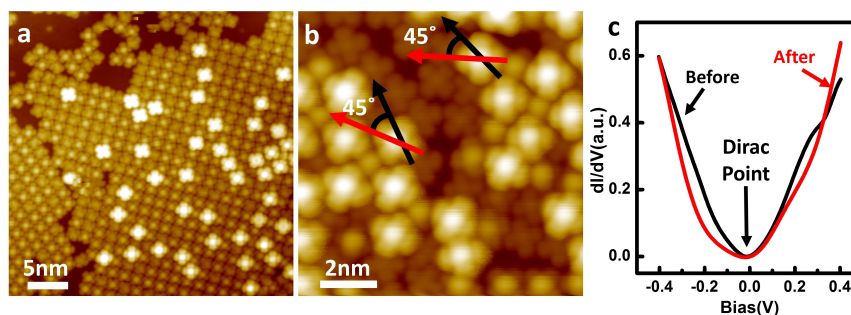
FIGURE 6.4: (a)STM images for $F_{16}CoPc$ molecules on the second layer which can clearly be identified with the four lobe cross-like structure as seen in the first layer.(b) Zoomed-in STM image for the $F_{16}CoPc$ on the second layer. The relative orientation between molecule in first and second layer remains constant at 45 ° Imaging conditions are V = 1.8 V, I = 200 pA. (c) STS spectra for Dirac point before and after doping the substrate with molecules. It is clearly observed that there is not shift in the Dirac point after doping.

dependent behavior we deposited more molecules over the substrate and molecules on the second layer were seen to self-assemble nicely as shown in the STM image in Figure 6.4 a and b. In most cases the molecules on the second layer were seen to adsorb exactly on top of a molecule in the first layer in flat-lying configuration which means that the molecular planes are parallel to each other. The relative orientation is 45 ° as shown in Figure 6.4 b where the orientation of the molecule in 1st layer(black arrow) and 2nd layer (red arrow) are marked. DFT calculations for $F_{16}CuPc$ suggest that such a configuration in the second layer is the most favorable [257]. The STS measurement for Dirac point before and after doping is shown in Figure 6.4 c. We haven't observed any shift in the Dirac point for both the spectra before(black curve) and after (red curve) doping. This implies that there is no significant charge transfer

between the molecule and the substrate. A shift in the Dirac point due to the interfacial charge transfer was observed in case of CuPc doping over Bi$_2$Se$_3$(as discussed in chapter 5)[258] and many other systems [208, 210]

6.3   Negative differential resistance of F$_{16}$CoPc on Bi$_2$Se$_3$

The current-voltage(I-V) curves were measured by placing the STM tip at the center of the molecule over the Co atom at 77 K. The representative spectra are shown in Figure 6.5 a. At positive bias the current starts to increase with the applied bias after 1.4 V and two different slopes are seen in the spectra. The interesting feature is observed at negative bias where the current starts to increase after -1.5 V. A clear NDR was observed at -1.9 V. After -1.7 V current increases rapidly and reaches the maximum value at -1.9 V and then starts decreasing with the applied bias. This decreasing the current with increasing bias is known as NDR. The corresponding dI/dV spectra measured using lock in technique is shown in Figure 6.5 b. A clear NDR was observed at -1.9 V. After the NDR the DOS increases gradually. On the other hand, at the positive bias a sharp peak was observed at 1.8 V which corresponds to the LUMO of F$_{16}$CoPc. Similar measurements were conducted on different isolated molecules and also on molecules within the self-assembly. It is observed that NDR only occurs at negative bias. Such NDR phenomenon were seen to appear due to the presence
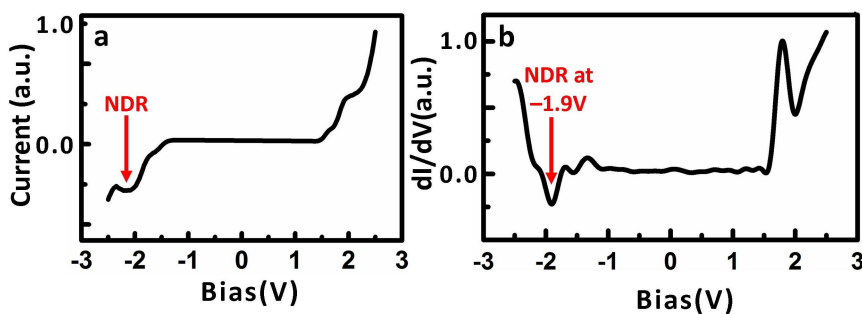
FIGURE 6.5: (a) I-V measurement at the center of F$_{16}$CoPc molecule showing NDR at -1.9 V (b) corresponding dI/dV spectra measured using lock-in technique clearly showing NDR at -1.9 V. NDR only observed at negative bias. Imaging condition V = 1.8 V, I = 400 pA.

of sharp features in the density of states of the STM tip or when the STM tip was functionalized with a molecule.[241–244] In such cases the observed NDR in I-V and dI/dV strongly depend on the tip condition and may disappear after changing the STM tip. But this is not the case in our measurements. To confirm that this is not an effect from the STM tip we have performed the same experiment with several different tips and the NDR effect was repeatedly observed at -1.9 V. Therefore we

believe that NDR, which is not a tip effect, underscores the dominant role played by the molecule-substrate interface.

In every system reported earlier, the main mechanism behind such behavior is the resonant tunneling between two specific orbitals either in between the narrow band of tip and substrate or in between the molecule orbital and narrow band of the substrate. When such resonant tunneling happens at a specific bias the tunneling current starts to increase rapidly and attains a maximum value and on further varying the bias the orbital falls off resonance and current starts to decrease as expected. This mechanism was nicely explained in an experimental report by Nathan et al. [247] and theoretically analysed by Datta et al.[259]. Where styrene and 2,2,6,6-tetramethyl-1-piperidinyl-oxy(TEMPO) were investigated on Si surface and NDR was observed in both bias polarity, positive and negative, by changing n-type or p-type doping in the bulk Si respectively. In this case the resonant tunneling was predicted to occur in between the molecular LUMO and narrow conduction band edge in case of n-type doped Si and NDR occurred at negative bias. For p-type doped substrate NDR was observed at positive bias with the corresponding resonant tunneling between HOMO and narrow valence band edge.

Another study with a different system, CoPc molecule on R3-Ag/Si substrate [254], where NDR was observed, suggests that the Co d_{z^2} orbital and the well defined intrinsic surface state are involved in the resonant tunneling. There is a finite gap between the intrinsic surface states. So at a critical bias Co d_{z^2} participates in resonant tunneling and tunneling current reaches the maximum value. Just after the resonant tunneling a slight increase in the bias shifts the d_{z^2} in the gap and tunneling current starts to decrease.

Both these results discussed above prove that resonant tunneling can happen between a specific molecular orbital and the narrow band of the substrate either from the bulk or surface. But the gap is necessary which might be the bulk band gap or a gap in between the surface state. In our observation we speculate which one of the above mentioned mechanisms [247, 254] is causing resonant tunneling. As the substrate Bi_2Se_3 in our system has both the bulk gap between conduction and valence band along with well defined spin-polarized surface state which has Dirac cone-like dispersion in the bulk gap (as shown in chapter 5). Then there are two possible ways of having the resonant tunneling- (1) the HOMO of $F_{16}CoPc$ is aligning with the valence band edge for resonance tunneling leading to a current maximum at -1.9 V and with further increase in bias the HOMO falls in the bulk gap between valence and conduction band and current starts to decrease(as discussed in ref [247]) and (2) the specific orbital of the molecule matches with the surface state for resonant tunneling(as discussed in ref[254]).

A detailed theoretical calculation is thus imperative to complete this exciting picture of NDR in our case.

6.4 Double row stacking of F$_{16}$CoPc on Ag(111)

To confirm the necessity of bulk gap or surface state we have investigated the same F$_{16}$CoPc molecule over Ag(111) metal substrate which has the same 6-fold surface symmetry as Bi$_2$Se$_3$ For the monolayer growth of F$_{16}$CoPc on Ag(111) the
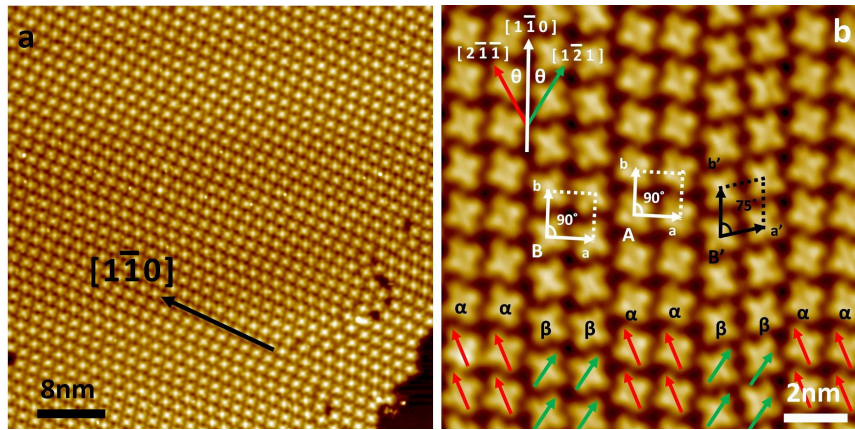
FIGURE 6.6: (a) High resolution STM image of well ordered rows of F$_{16}$CoPc along the [1$\bar{1}$0] crystallographic direction of Ag(111) surface. (b) Corresponding zoomed-in STM image showing two different orientations of the molecule α and β which are denoted by red and green arrows respectively. Two different unit cells consist of orientations marked as α and β orientation are labeled as A and B respectively. The angle between the unit cell axes is 90°. Another unit cell consists of β orientation is marked as B′ where the angle between unit cell axes is 75°. Image parameters are V = 1.5 V, I = 200 pA.

molecules were deposited over Ag(111) held at room temperature. In general metal phthalocyanine molecules in the 1st layer were seen to adsorb in flat-lying configuration [212, 220, 230]. Tilted configurations were observed in case of molecules at the monoatomic step edge, upright configuration being another possibility at the step edge [223] or in case of inert substrate [225]. In our experiment F$_{16}$CoPc molecules in the first layer were adsorbed in flat-lying configuration on the flat terrace of Ag(111) as shown in Figure 6.6 a. This is presumably the most favorable scenario as in such adsorption the molecluar π electrons ensure maximum overlap with the substrate electron density to have maximum molecule-substrate interaction. Figure 6.6 a shows that the molecules in flat-lying configuration assemble themselves along the [1$\bar{1}$0] crystallographic direction of the substrate to form molecular rows with defect-free long range order, where as the same molecules were seen to

form nano-domains on Bi_2Se_3 surface with very short range order. Such molecular row formation was observed previously in the self-assembly of F_16CuPc on Ag(111)[260] and Cu(111)[261], CoPc on semimetallic substrate Bi(111)[262] and $F_{16}CoPc$ on Ag(110)[263]. A closer look of small area STM image in Figure 6.6 b reveals that all molecules inside the row have a specific orientation with respect to the substrate. The two different orientations are denoted as α and β and are marked by red and green arrow respectively. The α and β molecules are making +30° or -30° with respect to the [1$\bar{1}$0] direction which are along the [1$\bar{2}$1] and [2$\bar{1}\bar{1}$] directions respectively as shown in Figure 6.6 b. Another important observation is that these molecules are not forming single molecular rows with a particular orientation(α or β) rather they are forming double molecular rows (dimer rows) implying that molecules in two neighboring rows have the same orientation either α or β.

With respect to the unit cell formation in the monolayer assembly there are three different types of unit cell formation. Two square lattice unit cells A and B consist of molecules with α and β orientation respectively. In both A and B unit cell the angle between the unit cell axes $\vec{a}$ and $\vec{b}$ is 90° These two unit cells are mirror symmetric to each other as seen in case of CuPc on Au(111)[230]. Another oblique unit cell with molecules of β orientation as marked by B′ (with black arrow) is observed which has the angle between the unit cell axis($\vec{a'}$ and $\vec{b'}$) of 75°. Based on these results we infer that the $F_{16}CoPc$ molecules exercise certain freedom in an orientational preference but they are very robust with respect to the long range order along the [1$\bar{1}$0] direction. The different in-plane relative arrangement of the molecules is attributed to the effect of F substitution. Because of the high electronic affinity of fluorine the atoms in the neighboring molecules are affected by an electrostatic repulsion. The relative arrangement of the neighboring molecules with respect to each other to form different unit cells is presumably to minimize the electrostatic repulsion.

6.5   Absence of negative differential resistance of $F_{16}CoPc$ on Ag(111)

The local electronic properties at the interface of $F_{16}CoPc$ on Ag(111) are explored using STS measurement. The dI/dV spectra is shown in Figure 6.7 a. The spectra is highly reproducible and independent of the orientation of the molecule. This measurement was also done using several STM tips to rule out the contribution of the STM tip in the spectra. The spectra clearly show two shoulders in both the bias polarity. Two different peaks at negative bias and positive bias were identified as HOMO
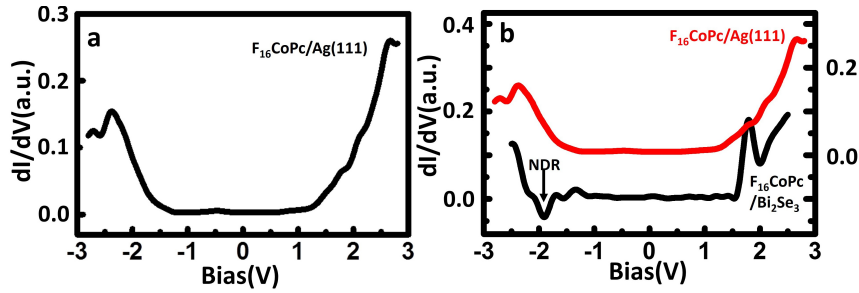
FIGURE 6.7: (a) dI/dV spectra of F_{16}CoPc over Ag(111) show-
ing two peaks at -2.1 V and 2.5 V as LUMO and HOMO respec-
tively. No NDR was observed at any bias voltage. V = 2.5 V, I = 400
pA. (b) dI/dV spectra of F_{16}CoPc/Ag(111) is plotted together with
F_{16}CoPc/Bi_2Se_3. F_{16}CoPc/Bi_2Se_3 is showing NDR at -1.9 V whereas
no NDR effect was observed for F_{16}CoPc on Ag(111). Spectra are
vertically shifted for clarity

and LUMO respectively. LUMO is at -2.1 V and the HOMO at 2.5 V. The HOMO-
LUMO gap(4.6 V) in our observation is larger than the previously observed value on
Ag(110)[264]. No NDR was observed at any applied bias. This implies that there is
no resonant tunneling which is expected due to the broad metallic band of Ag(111).
No contribution in the resonant tunneling with specific molecular orbital from the
STM tip. This confirms that NDR is only possible when the F_{16}CoPc molecules are
coupled with the Bi_2Se_3 surface. Also the observed NDR is not due to the resonant
tunneling between the STM tip as the measurement was performed with the same
tip. To clearly identify the difference between the dI/dV spectra of F_{16}CoPc/Bi_2Se_3
and F_{16}CoPc/Ag(111) we have plotted both the spectra in the same graph as shown
in Figure 6.7 b. The spectra are shifted vertically for clarity. It is clearly observed
that F_{16}CoPc/Bi_2Se_3 shows NDR at -1.9 V whereas for F_{16}CoPc/Ag(111) there is no
NDR is seen and the spectra shows a maxima at -2.1 V which is identified as LUMO.
The NDR effect is unique to the case of F_{16}CoPc adsorbed on Bi_2Se_3 and it is purely
due to the resonant tunneling between the molecule and the substrate.

6.6 Conclusions

This chapter reports a detailed study of self-assembly formation and interfacial elec-
tronic properties of F_{16}CoPc on Bi_2Se_3 topological insulator surface and Ag(111)
metallic surface. The STM and STS data for both these systems reveal that the
self-assembly formation and the interface electronic properties are different due to
the different molecule-substrate interactions. F_{16}CoPc molecules on the Bi_2Se_3 sur-
face form nano-domains with a particular orientation with respect to the substrate

symmetry. There are two different orientations of the molecule with $\pm 30°$ with respect to the $[\bar{1}\bar{1}20]$ crystallographic direction. Some molecules on the second layer were adsorbed on top of the molecules in the first layer with a relative orientation of $45°$. Similarly $F_{16}CoPc$ molecules on metallic $Ag(111)$ substrate were observed to adsorbed in two different orientations with $\pm 30°$ (α and β) with respect to $[1\bar{1}0]$ direction. But no nano-domains was observed,only molecular rows along the $[1\bar{1}0]$ direction with specific orientation throughout the entire row. Each two neighboring rows consists of same orientation. Three different unit cells were observed in this double row, two of them being mirror symmetric to each other. The most striking observation was revealed by the STS measurement. STS measurement shows that when the molecule is adsorbed over Bi_2Se_3 it shows NDR effect whereas no NDR was observed in case of the same molecule over $Ag(111)$ substrate. The observation of NDR is very unique and has been reported to occur when two narrow bands align themselves for resonant tunneling. This is not possible for a broad metallic band. Identifying such system showing robust NDR at particular bias is very important to build molecular NDR device which can advance the progress of molecule-based electronic devices.

Chapter 7

Conclusions and Outlook

The application of molecules in electronic devices depends crucially on the understanding of molecule-substrate, molecule-molecule interactions, adsorption geometry, and stability on substrates. The electric and magnetic properties of gas phase molecules generally get modified or quenched upon in contact with metal electrode or substrate. The primary mechanisms governing such changes are hybridization of molecular orbitals with the substrate band or charge transfer at the interface. Adsorption via weak van der Waals interaction offers a weak perturbation to the molecule-substrate system. A detailed understanding of these interactions and a refined control of the structural growth of organic molecules with various chemical functionalities and physical properties on the substrate is an essential requirement for the development of advanced molecular electronic devices. The invention of scanning tunneling microscope (STM) in 1983 led to a phenomenal advance in probing the step by step growth of molecular nanostructures from single molecule to one dimensional (1D) chain and then to monolayer or multilayer. The introduction of the scanning tunneling spectroscopy (STS) technique along with imaging, allows a direct real space probe of the above mentioned interactions, highest occupied molecular orbital (HOMO) and lowest unoccupied molecular orbital (LUMO), and emergent interfacial properties. Studying the HOMO and LUMO of a molecule is very important as HOMO, LUMO are analogous to the valence and conduction band of semiconductor and mainly responsible for the electronic transport through the molecule.

In this thesis, we have used STM and STS to investigate the molecule-substrate interactions, intermolecular interactions, interface properties, and HOMO-LUMO of individual molecules upon adsorption on the substrates. The molecular systems that we have investigated were MPc (M=Fe, Co, Cu) molecules with cyano(-CN) and fluorine(F) substituent on the noble metal surfaces Au(111) and Ag(111), and topological insulator Bi2Se3 surface. In section 1.2 different types of adsorption of atom/molecules are described. A qualitative picture of molecular orbital hybridization, charge transfer through HOMO or LUMO, and weak van-der Waals interactions

are also discussed. The second chapter of this thesis presents the theoretical background of STM and its operating principle. First, we have considered the 1D step potential as a representative model for STM tip-sample tunnel junction followed by the 3D Tersoff and Hamann model STS data acquisition using lock-in amplifier is also described in this chapter.

In chapter 3, we have described the effect of –CN functionalization of CuPc and compared it with CuPc in the context of the adsorption of CuPc and CuPc(CN)$_8$ molecules at the monoatomic (MA) step edges of the Au(111) surface. CuPc adsorbs only in one configuration but there are two adsorption configurations for CuPc(CN)$_8$ at the Au(111) step edge forming 1D linear chains. This clearly reflects that the –CN functional group is altering the interaction of these two molecules with MA. Single CuPc(CN)$_8$ molecule at the MA step aligns with one of the principal axes parallel to the step edge and the other one perpendicular to the step edge which is [1 $\bar{1}$ 0] direction. But in the 1D chain at the step edge CuPc(CN)$_8$ molecules align themselves in $\pm$ 22 $^\circ$ with [1$\bar{1}$0] direction to form CN—HC bond. The alignment of CuPc(CN)$_8$ molecules in such configurations enables a transition from a linear 1D assembly to a 2D planar assembly upon higher coverage of molecules by forming maximum number of CN—-HC hydrogen bonds to enhance the intermolecular interaction. No such transition was observed in case of CuPc molecules. STS measurements show that there is a systematic shift of HOMO to a lower energy as the molecule changes its configuration. This is a direct correlation between the adsorption morphology and the local electronic structure of the molecule. The results from DFT calculations for CuPc(CN)$_8$ adsorption and the shift of HOMO are in accord with the experimental results.

In chapter 4, we have presented the influence of cyano substitution of CuPc on its molecular self-assembly on the flat terraces of Au(111). STM images of CuPc(CN)$_8$ on Au(111) show self-assembly with a tetrameric unit cell that exhibits adsorption-induced structural chirality leaving the herringbone reconstruction periodicity unchanged. Monolayer coverage of CuPc on Au(111) also showed tetramers in two mirror-symmetric configurations. But the herringbone reconstruction periodicity was altered. This is indicative of a stronger molecule-substrate interaction in the CuPc/Au(111) assembly than in the CuPc(CN)$_8$/Au(111) assembly. From the STS measurements, the HOMO–LUMO gap showed a substantial increment from 3.0 eV for the CuPc/Au(111) system to 4.3 eV for the CuPc(CN)$_8$/Au(111) system. We attribute these results to the partial cyanation of CuPc. Ab initio DFT calculations validated these experimental findings of herringbone periodicity modification and the variation of the HOMO-LUMO gap. Voltage-dependent STM images unveil the orbital-energy-specific chirality of the CuPc(CN)$_8$ molecules and superimpose

right-and left-handedness on the existing structural chirality within the assembly. However, for CuPc no such energy-dependent chiral behavior was witnessed at any orbital energy.

These two chapters, 3 and 4 together, reflect that the MA step of metal can be used as a template to construct defect free 1D molecular chains. The pendant group substitution is an effective way to tune the molecule-substrate and intermolecular interaction. This can help for engineering directional self-assembled growth over the surface. The electronic properties of molecules can also be altered by such functional group substitution.

Chapter 5 focuses on magnetic phthalocyanine molecules FePc and CuPc on the topological insulator (TI) surface Bi_2Se_3 emphasizing on their adsorption behavior and the spectroscopic signatures of the magnetic molecule-TI interface on the intrinsic characteristic nature of TI. At very low coverage individual FePc molecules adsorb on the top site of the Se surface of Bi_2Se_3. But after annealing at 100 ° a few molecules diffuse to the bridge site of the Bi2Se3 surface and attain a reduced symmetry phase. Such site-dependent adsorption with single molecule resolution is determined by concomitant background surface atomic resolution.. No large scale ordering of FePc is observed on Bi_2Se_3 even at higher coverage. An adsorption site dependent shift in HOMO and LUMO peaks is recorded in the STS measurement of FePc. However there is no shift of the Dirac point due to the doping with FePc molecules. Thus the topological surface state of Bi_2Se_3 remains protected. In case of CuPc on Bi_2Se_3 despite a weak interaction of the fully occupied d_{z^2} orbital with the substrate, CuPc is observed to bind stably with the surface via ligand-substrate interaction and charge transfer in the interface confirming the chemisorption of CuPc over the Bi_2Se_3 surface. CuPc orients along one of the three equivalent Se close-packed directions of the topmost layer. The Dirac surface state remains protected but due to the interfacial charge transfer from molecule to the substrate, a shift of Dirac point from the Fermi energy towards negative energy is observed with CuPc doping. The STS measurement for HOMO and LUMO orbitals and a comparison of the HOMO-LUMO gap with CuPc/Au(111) reflects the gap increment mainly due to the shift of LUMO towards the positive voltage. This gap increment is attributed to the reduced screening due to the Bi_2Se_3 surface than the metallic Au(111). The interfacial charge transfer leaves the molecules charged and thereby the individual molecules become repulsive in nature. As a result even at a coverage more than 1ML CuPc doesn't form any self-assembly on the flat terraces of Bi_2Se_3 but CuPc forms a 1D chain with standing-up configuration nucleated from the step edge. Such standing-up of CuPc stacking opens up channels for indirect spin exchange via the pyrrole nitrogen of the phthalocyanine unit.

In chapter 6, we have reported a detailed study of self-assembly formation and interfacial electronic properties of $F_{16}CoPc$ on Bi_2Se_3 topological insulator surface and Ag(111) metallic surface. The STM and STS data for both these systems reveal characteristic self-assembly formation and interface electronic properties due to the modified substrate-molecule interaction and intermolecular interaction due to F substitution. $F_{16}CoPc$ molecules on the Bi_2Se_3 surface form nano-domains in a particular orientation with the substrate symmetry. There are two different orientations of the molecule are observed with $\pm$ 30 ° with respect to the [1$\bar{1}$20] crystallographic direction. Some molecules on the second layer are adsorbed with a relative orientation of 45 ° with respect to the molecule at the first layer and sitting exactly on top of a molecule. Similarly, $F_{16}CoPc$ molecules on metallic Ag(111) substrate are seen in two different orientation in $\pm$ 30 ° with respect to [1 $\bar{1}$ 0] direction. Molecules prefer to form a double molecular row along the [1 $\bar{1}$ 0] direction with one of the orientation throughout the entire row. Three different unit cells are observed in this double row, two of them being mirror symmetric to each other. The most striking observation was revealed by the STS measurement. STS measurement shows that when the molecule adsorbed over Bi_2Se_3, it shows NDR effect at -1.9V due to the resonant tunneling between molecular orbital and the substrate. While no NDR was observed in case of the same molecule over Ag(111) substrate. The observation of NDR is very unique and only possible when two narrow bands align themselves for resonant tunneling and not possible for the broad metal band. To understand our results completely calls for DFT calculations to pinpoint the bands responsible for resonant tunneling. NDR is a potent mechanism, which if harnessed effectively and in a scalable way, can revolutionize device design and implementation in molecular electronics.

To summarize, the detailed investigation from single molecule to self-assembly of MPc with or without functional group substitution on various substrates have empowered us to shed light on the structural growth of molecular nanostructures and the changes in the local electronic properties both in the molecule and the substrate. The results put forth by this thesis are a significant footstep to understand the adsorption geometry, electronic structure, and charge redistribution when molecules are deposited on a substrate. Undoubtedly each portion of the molecule contributes to the molecule-substrate interaction. The central metal ion, the ligand, the substituent group, and the underneath surface have to be considered to understand the local electronic properties of the molecule. Moreover, charge carrier transport through the interface is very crucial to any electronic and optoelectronic device made from a single molecule, monolayer, or thin organic film. Thus, the hybridization, charge transfer, and the energy level alignment must be understood in detail at the molecular scale to

utilize the emerging interface properties for device applications.

It has been more than 30 years [26] that scientists have invested their efforts to develop fabrication and measurement techniques to characterize the charge transport in a single molecule, self-assembled monolayer (SAM), metal junctions including scanning probe microscopies (STM, C-AFM), mechanically controlled break junctions. Though we achieved some really effective techniques to probe the electronic properties even at single molecular level but a broadly accepted and scalable molecule-substrate combination for electronic device applications is yet to be realized. Our study on electron withdrawing group substitution suggests that the individual molecular properties and the intermolecular interaction can be improved by substitution. To take this work further such functional group substitution can be incorporated in other phthalocyanines or even in other organic molecules to tune their electronic properties, and then combine with various metal or magnetic substrates. The substituent groups can enhance the intermolecular interaction while magnetic substrates can provide extra freedom to interact with central metal ion via spin-spin interaction. The other way is to combine this substituted phthalocyanine with the unsubstituted molecule to form a bimolecular selfassembly with a different central metal ion with a different spin state as described in reference [147] to create a 2D spin array. The study of MPcs on the more reactive topological insulator surface rather than the noble metal further confirms the role played by the substrate. The most interesting part of using topological insulator substrate is that the topological surface state which shows a Dirac cone-like linear dispersion is spin-polarized. So it will be exciting to study the spin-dependent effects using spin-polarized STM at low temperature(4.2 K). The immediate question that arises after observing NDR is whether it is a spin-polarized effect or not, as the substrate surface state is spin-polarized. Such spin-dependent study of organic molecules on topological insulator or magnetic substrate will be fascinating and can contribute significantly in the interdisciplinary field called molecular spintronics [30] or Spinterface [49].

Appendix A

STM tip preparation

In scanning tunneling microscope (STM) electrons tunnel across the potential barrier established between sharp metal tip and conducting or semiconducting surface, under appropriate bias voltage. Resolution of the STM depends upon the quality of the tip. STM tips are generally fabricated from metal wires. Tungsten (W) wire electrochemically etched to fabricate good quality tips.

Electrochemical etching procedure involves anodic dissolution of the metal electrode. For fabricating sharper tips direct current (dc) etching is preferred. "Drop off" method is used for dc etching, in this method etching occurred at electrolyte metal wire interface and portion of wire drops off when its weight exceed the tensile strength of etched region of the wire. Schematic of the etching process is shown in the figure below. The electrochemical reaction involves anodic dissolution of tung-
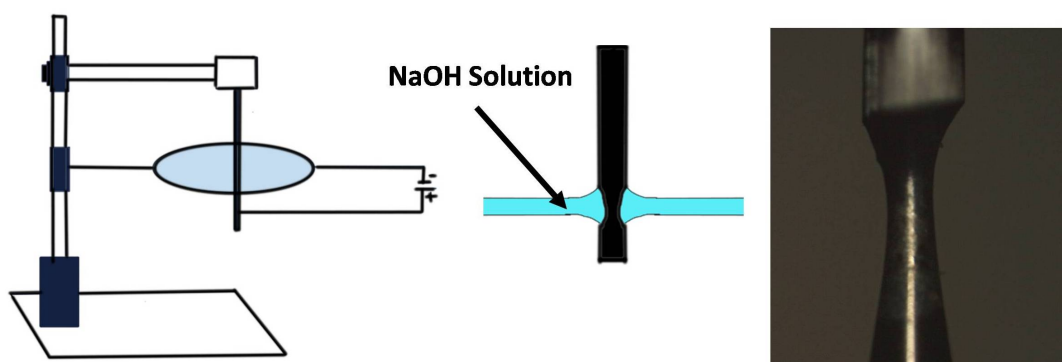
FIGURE A.1: a)Left schematic diagram for W tip etching using NaOH solution film. Middle enlarged view showing the etching shape. Right actual partially etch W tip is shown to get an idea about the etching shape.

sten in aqueous base. The apparatus consist of film of 2M NaOH solution on metal ring acting as cathode and the W wire pierce the film at centre acting as anode. W wire held with support and portion of wire below the film connected to voltage source by very thin copper wire. Thickness of wire is 0.25 mm.

Etching occurs at meniscus formed by the electrolyte film at W wire, when positive bias is applied to wire. The detailed chemical reactions are as below[265].

$$Cathode: \qquad 6H_2O + 6e^- \rightarrow 3H_2(g) + 6OH^-$$

$$Anode: \qquad W(s) + 8OH^- \rightarrow WO_4^{2-} + 4H_2O + 6e^-$$

$$W(s) + 2OH^- 6H_2O - \rightarrow WO_4^{2-} + 3H_2(g)$$
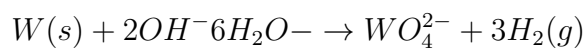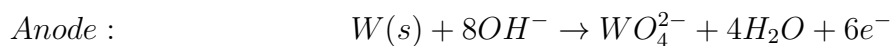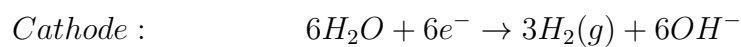
W oxidises to form soluble anion WO_4^{2-} at the anode, water reduces into hydrogen
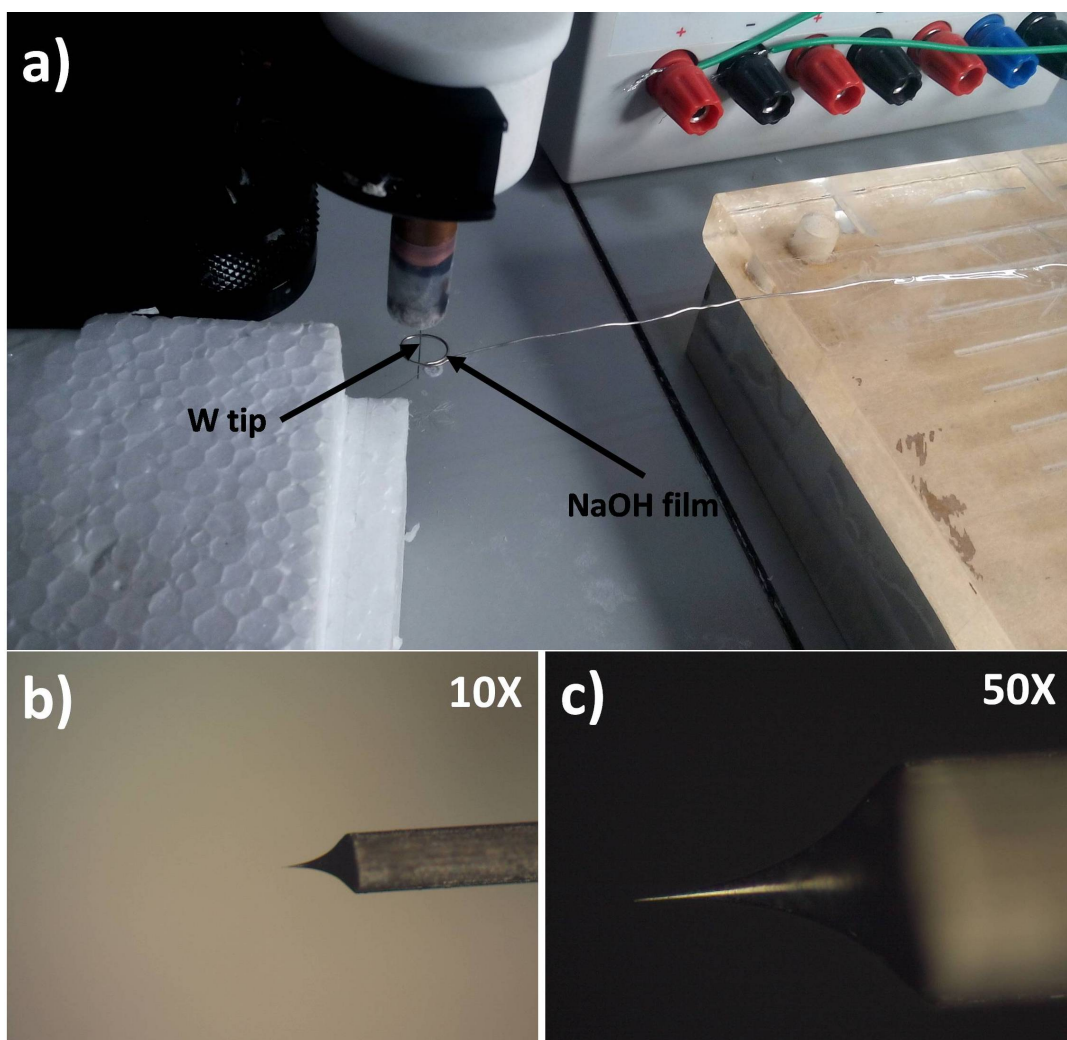
FIGURE A.2: a) Picture of actual tip etching setup, where NaOH film was prepared in the ring of Ni wire marked with arrow. b-c) are the optical microscope image of a good tip with 10X and 50X magnification respectively.

gas and OH- ions at cathode. E0 is sum of standard reduction potential (SRP) and standard oxidation potential (SOP) for tungsten. Etching starts when potential exceeds E0 value that is 1.43 V. Voltage applied for etching is 4 V. Circuit breaks as wire fall down after completion of etching due to weight of wire below film. Tip is then cleaned with distilled water. Tips formed by this method are sharp and hyperboloidal in shape. Parameters that affect the sharpness of tip are length of wire in film, voltage applied and cleaning procedure. Optical microscope is used to quickly check the quality of tip. Actual tip eatching setup and optical microscope image of a good tip is shown in below Figure A.2

Appendix B

Bi$_2$Se$_3$ crystal growth

The Bi$_2$Se$_3$ single crystal was grown using the modified Bridgman technique[266]. First, stoichiometric mixtures of high purity elements Bi, 99.999 and Se, 99.999 were weighted and grounded properly to prepare fine mixture in powder form under argon environment in a golve box. Fine mixture then loaded in a quartz ampoule. The ampoule then evacuated up to 10^{-3} torr and sealed by melting the neck of the quartz tube. The mixture then melted at at 850 ° C inside a vertical furnace for 24 hrs. Then the mixture allowed to cool down to 650° C very slowly at the rate of 3°C per hrs. The mixture then kept at 650°C for a day then cooled it down to room temp. Single crystal Bi$_2$Se$_3$ was collected by breaking the quartz ampoule. A time and temperature profile is shown in Figure B.1 to represent the whole reaction procedure.
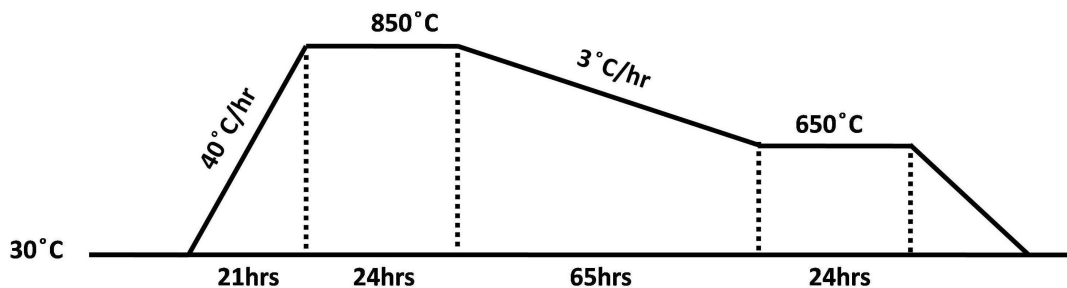
FIGURE B.1: Time and temperature profile for Bi$_2$Se$_3$ single crystal growth.

Appendix C

HOMO and LUMO

The STS spectra presented in chapter 3 were measured using lock in amplifier with moldulation frequency 652Hz and modulation voltage 20mv. The spectra were taken by positioning the tip at the center of the molecule. Below figure represent the histogram for the HOMO and LUMO position for the $CuPc(CN)_8$ molecules for three different configurations.
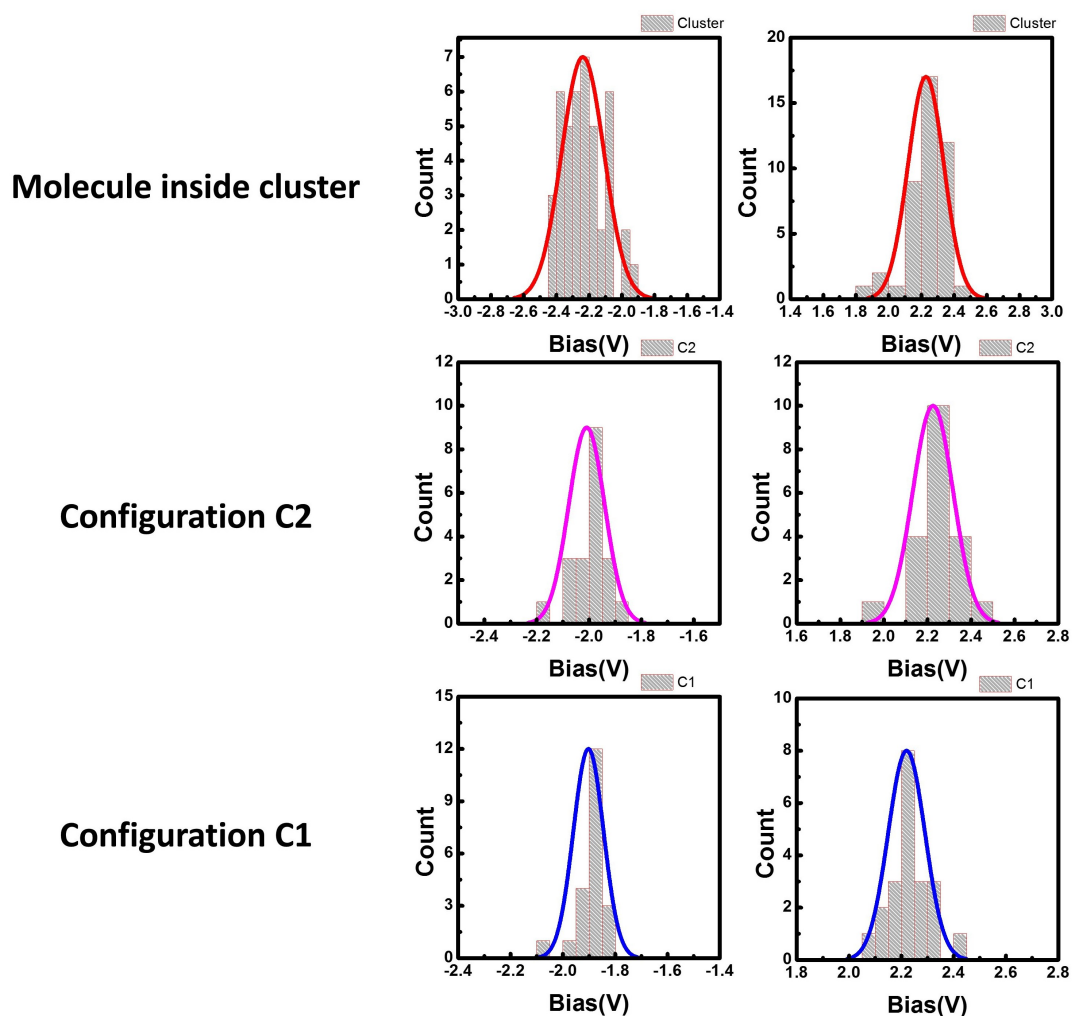
FIGURE C.1: Histogram plot for HOMO and LUMO positions for three different adsorptions of molecules, inside of a cluster on flat terrace, C2 on MA step edge, and C1 on MA step edge.

Bibliography

[1]   William F Brinkman, Douglas E Haggan, and William W Troutman. "A history of the invention of the transistor and where it will lead us". In: *IEEE Journal of Solid-State Circuits* 32.12 (1997), pp. 1858–1865.

[2]   Jack S Kilby. "Invention of the integrated circuit". In: *IEEE Trans. on Electoron Devices* 23.7 (1976), pp. 651–652.

[3]   Richard P Feynman. "There's plenty of room at the bottom [data storage]". In: *Journal of microelectromechanical systems* 1.1 (1992), pp. 60–66.

[4]   Wolfgang M Arden. "The international technology roadmap for semiconductors—perspectives and challenges for the next 15 years". In: *Current Opinion in Solid State and Materials Science* 6.5 (2002), pp. 371–377.

[5]   AE Grigorescu and CW Hagen. "Resists for sub-20-nm electron beam lithography with a focus on HSQ: state of the art". In: *Nanotechnology* 20.29 (2009), p. 292001.

[6]   Takashi Ito and Shinji Okazaki. "Pushing the limits of lithography". In: *Nature* 406.6799 (2000), p. 1027.

[7]   GF Cardinale et al. "Demonstration of pattern transfer into sub-100 nm polysilicon line/space features patterned with extreme ultraviolet lithography". In: *Journal of Vacuum Science & Technology B: Microelectronics and Nanometer Structures Processing, Measurement, and Phenomena* 17.6 (1999), pp. 2970–2974.

[8]   Bo Cui. "Recent advances in nanofabrication techniques and applications". In: (2011).

[9]   David A Muller et al. "The electronic structure at the atomic scale of ultrathin gate oxides". In: *Nature* 399.6738 (1999), p. 758.

[10]   KS Novoselov et al. "Two-dimensional atomic crystals". In: *Proceedings of the National Academy of Sciences* 102.30 (2005), pp. 10451–10453.

[11]   Kostya S Novoselov et al. "Electric field effect in atomically thin carbon films". In: *science* 306.5696 (2004), pp. 666–669.

[12]   Vinod K Sangwan and Mark C Hersam. "Electronic Transport in Two-Dimensional Materials". In: *Annual review of physical chemistry* 69 (2018), pp. 299–325.

[13]   Gianluca Fiori et al. "Electronics based on two-dimensional materials". In: *Nature nanotechnology* 9.10 (2014), p. 768.

[14]   Chwan K Chiang et al. "Electrical conductivity in doped polyacetylene". In: *Physical review letters* 39.17 (1977), p. 1098.

[15]   Hideki Shirakawa. "The discovery of polyacetylene film: the dawning of an era of conducting polymers (Nobel lecture)". In: *AngewandteChemie International Edition* 40.14 (2001), pp. 2574–2580.

[16]   Josef Salbeck. "Electroluminescence with organic compounds". In: *Berichte der Bunsengesellschaft für physikalischeChemie* 100.10 (1996), pp. 1667–1677.

[17]   Ching W Tang and Steven A VanSlyke. "Organic electroluminescent diodes". In: *Applied physics letters* 51.12 (1987), pp. 913–915.

[18]   Hi Koezuka, A Tsumura, and T Ando. "Field-effect transistor with polythiophene thin film". In: *Synthetic Metals* 18.1-3 (1987), pp. 699–704.

[19]   Yang Yang and Fred Wudl. "Organic electronics: from materials to devices". In: *Advanced Materials* 21.14-15 (2009), pp. 1401–1403.

[20]   Igor Žutić, Jaroslav Fabian, and S Das Sarma. "Spintronics: Fundamentals and applications". In: *Reviews of modern physics* 76.2 (2004), p. 323.

[21]   SA Wolf et al. "Spintronics: a spin-based electronics vision for the future". In: *Science* 294.5546 (2001), pp. 1488–1495.

[22]   Mario Norberto Baibich et al. "Giant magnetoresistance of (001) Fe/(001) Cr magnetic superlattices". In: *Physical review letters* 61.21 (1988), p. 2472.

[23]   Grünberg Binasch et al. "Enhanced magnetoresistance in layered magnetic structures with antiferromagnetic interlayer exchange". In: *Physical review B* 39.7 (1989), p. 4828.

[24]   Hyun Cheol Koo et al. "Control of spin precession in a spin-injected field effect transistor". In: *Science* 325.5947 (2009), pp. 1515–1518.

[25]   AR Mellnik et al. "Spin-transfer torque generated by a topological insulator". In: *Nature* 511.7510 (2014), p. 449.

[26]   Dong Xiang et al. "Molecular-scale electronics: from concept to function". In: *Chemical reviews* 116.7 (2016), pp. 4318–4440.

[27] Naoto Ishikawa et al. "Lanthanide double-decker complexes functioning as magnets at the single-molecular level". In: *Journal of the American Chemical Society* 125.29 (2003), pp. 8694–8695.

[28] Stefan Schmaus et al. "Giant magnetoresistance through a single molecule". In: *Nature nanotechnology* 6.3 (2011), p. 185.

[29] Xiangnan Sun et al. "A molecular spin-photovoltaic device". In: *Science* 357.6352 (2017), pp. 677–680.

[30] Alexandre R Rocha et al. "Towards molecular spintronics". In: *Nature materials* 4.4 (2005), p. 335.

[31] Bernhard Mann and Hans Kuhn. "Tunneling through fatty acid salt monolayers". In: *Journal of Applied Physics* 42.11 (1971), pp. 4398–4405.

[32] Arieh Aviram and Mark A Ratner. "Molecular rectifiers". In: *Chemical Physics Letters* 29.2 (1974), pp. 277–283.

[33] NJ Geddes et al. "Fabrication and investigation of asymmetric current-voltage characteristics of a metal/Langmuir–Blodgett monolayer/metal structure". In: *Applied physics letters* 56.19 (1990), pp. 1916–1918.

[34] Robert M Metzger et al. "Unimolecular electrical rectification in hexadecylquinoliniumtricyanoquinodimethanide". In: *Journal of the American Chemical Society* 119.43 (1997), pp. 10455–10466.

[35] Gerd Binnig et al. "7×7 reconstruction on Si (111) resolved in real space". In: *Physical review letters* 50.2 (1983), p. 120.

[36] Christian Joachim et al. "Electronic transparence of a single C 60 molecule". In: *Physical review letters* 74.11 (1995), p. 2102.

[37] Jiwoong Park et al. "Coulomb blockade and the Kondo effect in single-atom transistors". In: *Nature* 417.6890 (2002), p. 722.

[38] Stuart M Lindsay and Mark A Ratner. "Molecular transport junctions: Clearing mists". In: *Advanced Materials* 19.1 (2007), pp. 23–31.

[39] H Yu Lam and Douglas Natelson. "Transport in single-molecule transistors: Kondo physics and negative differential resistance". In: *Nanotechnology* 15.10 (2004), S517.

[40] AA Houck et al. "Kondo effect in electromigrated gold break junctions". In: *Nano Letters* 5.9 (2005), pp. 1685–1688.

[41] Aidi Zhao et al. "Controlling the Kondo effect of an adsorbed magnetic ion through its chemical bonding". In: *Science* 309.5740 (2005), pp. 1542–1544.

[42]   Paolo Sessi et al. "Single electron gating of topological insulators". In: *Advanced Materials* 28.45 (2016), pp. 10073–10078.

[43]   Jens K Nørskov et al. "Density functional theory in surface chemistry and catalysis". In: *Proceedings of the National Academy of Sciences* (2011), p. 201006652.

[44]   Andrew Zangwill. *Physics at surfaces*. Cambridge university press, 1988.

[45]   Carsten Deibel and Vladimir Dyakonov. "Polymer–fullerene bulk heterojunction solar cells". In: *Reports on Progress in Physics* 73.9 (2010), p. 096401.

[46]   Zoltán G Soos and Benjamin J Topham. "Surface dipole of F4TCNQ films: Collective charge transfer and dipole–dipole repulsion in submonolayers". In: *Organic Electronics* 12.1 (2011), pp. 39–44.

[47]   Xinghua Lu et al. "Charge transfer and screening in individual C 60 molecules on metal substrates: A scanning tunneling spectroscopy and theoretical study". In: *Physical Review B* 70.11 (2004), p. 115418.

[48]   EV Tsiper et al. "Electronic polarization at surfaces and thin films of organic molecular crystals: PTCDA". In: *Chemical Physics Letters* 360.1-2 (2002), pp. 47–52.

[49]   Mirko Cinchetti, V Alek Dediu, and Luis E Hueso. "Activating the molecular spinterface". In: *Nature materials* 16.5 (2017), p. 507.

[50]   A v Braun and J Tcherniac. "Über die produkte der einwirkung von acetanhydrid auf phthalamid". In: *Berichte der deutschenchemischenGesellschaft* 40.2 (1907), pp. 2709–2714.

[51]   Miles A Dahlen. "The phthalocyanines a new class of synthetic pigments and dyes". In: *Industrial & Engineering Chemistry* 31.7 (1939), pp. 839–847.

[52]   Gerd Löbbert. "Phthalocyanines". In: *Ullmann's Encyclopedia of Industrial Chemistry* (2000).

[53]   Alexander B Sorokin. "Phthalocyanine metal complexes in catalysis". In: *Chemical reviews* 113.10 (2013), pp. 8152–8191.

[54]   Avery P Yuen et al. "Photovoltaic properties of M-phthalocyanine/fullerene organic solar cells". In: *Solar Energy* 86.6 (2012), pp. 1683–1688.

[55]   Challuri Vijay Kumar et al. "Perovskite solar cell with low cost Cu-phthalocyanine as hole transporting material". In: *RSC Advances* 5.5 (2015), pp. 3786–3791.

[56]   J Blochwitz et al. "Low voltage organic light emitting diodes featuring doped phthalocyanine as hole transport material". In: *Applied Physics Letters* 73.6 (1998), pp. 729–731.

[57] Christian Wäckerlin et al. "Giant Hysteresis of Single-Molecule Magnets Adsorbed on a Nonmagnetic Insulator". In: *Advanced Materials* 28.26 (2016), pp. 5195–5199.

[58] Christian G Claessens, Uwe Hahn, and Tomas Torres. "Phthalocyanines: From outstanding electronic properties to emerging applications". In: *The Chemical Record* 8.2 (2008), pp. 75–97.

[59] Andrew Zangwill. *Physics at surfaces*. Cambridge university press, 1988.

[60] Angelika Kühnle. "Self-assembly of organic molecules at metal surfaces". In: *Current Opinion in Colloid & Interface Science* 14.2 (2009), pp. 157–168.

[61] ND Lang and AR Williams. "Theory of atomic chemisorption on simple metals". In: *Physical Review B* 18.2 (1978), p. 616.

[62] Jens K Nørskov et al. "Density functional theory in surface chemistry and catalysis". In: *Proceedings of the National Academy of Sciences* (2011), p. 201006652.

[63] Roald Hoffmann. "A chemical and theoretical way to look at bonding on surfaces". In: *Reviews of modern Physics* 60.3 (1988), p. 601.

[64] Johannes V Barth, Giovanni Costantini, and Klaus Kern. "Engineering atomic and molecular nanostructures at surfaces". In: *Nanoscience And Technology: A Collection of Reviews from Nature Journals*. World Scientific, 2010, pp. 67–75.

[65] Byron D Gates et al. "New approaches to nanofabrication: molding, printing, and other techniques". In: *Chemical reviews* 105.4 (2005), pp. 1171–1196.

[66] George M Whitesides, John P Mathias, and Christopher T Seto. "Molecular self-assembly and nanochemistry: a chemical strategy for the synthesis of nanostructures". In: *Science* 254.5036 (1991), pp. 1312–1319.

[67] Richard P Feynman. "There's Plenty of Room at the Bottom". In: *SPIE MILESTONE SERIES MS* 182 (2006), p. 3.

[68] Gerd Binnig et al. "Surface studies by scanning tunneling microscopy". In: *Physical review letters* 49.1 (1982), p. 57.

[69] Gerd Binnig et al. "7×7 reconstruction on Si (111) resolved in real space". In: *Physical review letters* 50.2 (1983), p. 120.

[70] JK Gimzewski, E Stoll, and RR Schlittler. "Scanning tunneling microscopy of individual molecules of copper phthalocyanine adsorbed on polycrystalline silver surfaces". In: *Surface Science* 181.1-2 (1987), pp. 267–277.

[71]   H Ohtani et al. "Scanning tunneling microscopy observations of benzene molecules on the Rh (111)-(3× 3)(C 6 H 6+ 2CO) surface". In: *Physical review letters* 60.23 (1988), p. 2398.

[72]   Xing Lu et al. "Scanning tunneling microscopy of metal phthalocyanines: d7 and d9 cases". In: *J. Am. Chem. Soc.* 118.30 (1996), pp. 7197–7202.

[73]   Eric I Altman and Richard J Colton. "Determination of the orientation of C 60 adsorbed on Au (111) and Ag (111)". In: *Physical Review B* 48.24 (1993), p. 18244.

[74]   AJ Mayne et al. "An STM study of the chemisorption of C2H4 on Si (001)(2× 1)". In: *Surface science* 284.3 (1993), pp. 247–256.

[75]   SD Kevan and RH Gaylord. "High-resolution photoemission study of the electronic structure of the noble-metal (111) surfaces". In: *Physical Review B* 36.11 (1987), p. 5809.

[76]   Gerd Binnig and Heinrich Rohrer. "Scanning tunneling microscopy". In: *Surface science* 126.1-3 (1983), pp. 236–244.

[77]   G Binnig et al. "Electron-metal-surface interaction potential with vacuum tunneling: Observation of the image force". In: *Physical Review B* 30.8 (1984), p. 4816.

[78]   Aidi Zhao et al. "Controlling the Kondo effect of an adsorbed magnetic ion through its chemical bonding". In: *Science* 309.5740 (2005), pp. 1542–1544.

[79]   Aparna Deshpande et al. "Spatially resolved spectroscopy of monolayer graphene on SiO 2". In: *Physical Review B* 79.20 (2009), p. 205411.

[80]   Yuqi Xia et al. "Observation of a large-gap topological-insulator class with a single Dirac cone on the surface". In: *Nature physics* 5.6 (2009), p. 398.

[81]   Rejaul Sk et al. "Enhancing the Intermolecular Interaction by Cyano Substitution in CuPc". In: *J. Phys. Chem. C* 122 (2017), pp. 429–437.

[82]   BC Stipe, MA Rezaei, and W Ho. "Single-molecule vibrational spectroscopy and microscopy". In: *Science* 280.5370 (1998), pp. 1732–1735.

[83]   Ro Wiesendanger et al. "Observation of vacuum tunneling of spin-polarized electrons with the scanning tunneling microscope". In: *Physical Review Letters* 65.2 (1990), p. 247.

[84]   L Berbil-Bautista et al. "Spin-polarized scanning tunneling microscopy and spectroscopy of ferromagnetic Dy (0001)/W (110) films". In: *Physical Review B* 76.6 (2007), p. 064411.

[85] MS Ramachandra Rao and Giorgio Margaritondo. "Three decades of scanning tunnelling microscopy that changed the course of surface science". In: *Journal of Physics D: Applied Physics* 44.46 (2011), p. 460301.

[86] Roland Wiesendanger. "Spin mapping at the nanoscale and atomic scale". In: *Reviews of Modern Physics* 81.4 (2009), p. 1495.

[87] Claude Cohen-Tannoudji, Bernard Diu, and Frank Laloe. "Quantum Mechanics, Volume 2". In: *Quantum Mechanics, Volume 2, by Claude Cohen-Tannoudji, Bernard Diu, Frank Laloe, pp. 626. ISBN 0-471-16435-6. Wiley-VCH, June 1986.* (1986), p. 626.

[88] John Bardeen. "Tunnelling from a many-particle point of view". In: *Physical Review Letters* 6.2 (1961), p. 57.

[89] J Tersoff and DR Hamann. "Theory and application for the scanning tunneling microscope". In: *Physical review letters* 50.25 (1983), p. 1998.

[90] Jerry Tersoff and DR Hamann. "Theory of the scanning tunneling microscope". In: *Physical Review B* 31.2 (1985), p. 805.

[91] April D Jewell, Heather L Tierney, and E Charles H Sykes. "Gently lifting Gold's herringbone reconstruction: trimethylphosphine on Au (111)". In: *Physical Review B* 82.20 (2010), p. 205401.

[92] S Urazhdin et al. "Scanning tunneling microscopy of defect states in the semiconductor Bi 2 Se 3". In: *Physical Review B* 66.16 (2002), p. 161306.

[93] M Zahid Hasan and Charles L Kane. "Colloquium: topological insulators". In: *Reviews of Modern Physics* 82.4 (2010), p. 3045.

[94] Lukas kormos et al. "Molecular Passivation of Substrate Step Edges as Origin of Unusual Growth Behavior of 4,4′-Biphenyl Dicarboxylic Acid on Cu(001)". In: *J. Phys. Chem. C* 122.5 (2018), pp. 2815–2820.

[95] Peter E Blöchl. "Projector augmented-wave method". In: *Physical review B* 50.24 (1994), p. 17953.

[96] Georg Kresse and Jürgen Hafner. "Ab initio molecular dynamics for liquid metals". In: *Physical Review B* 47.1 (1993), p. 558.

[97] Georg Kresse and Jürgen Furthmüller. "Efficient iterative schemes for ab initio total-energy calculations using a plane-wave basis set". In: *Physical review B* 54.16 (1996), p. 11169.

[98] John P Perdew, Kieron Burke, and Matthias Ernzerhof. "Generalized gradient approximation made simple". In: *Physical review letters* 77.18 (1996), p. 3865.

[99]   Stefan Grimme et al. "A consistent and accurate ab initio parametrization of density functional dispersion correction (DFT-D) for the 94 elements H-Pu". In: *The Journal of chemical physics* 132.15 (2010), p. 154104.

[100] Johannes V Barth, Giovanni Costantini, and Klaus Kern. "Engineering atomic and molecular nanostructures at surfaces". In: *Nanoscience And Technology: A Collection of Reviews from Nature Journals*. World Scientific, 2010, pp. 67–75.

[101] Geoffrey A Ozin et al. "Nanofabrication by self-assembly". In: *Mat. Today* 12.5 (2009), pp. 12–23.

[102] Roberto Otero et al. "Molecular Self-Assembly at Solid Surfaces". In: *Adv. Mater.* 23.44 (2011), pp. 5148–5176.

[103] Susan M Barlow and R Raval. "Complex organic molecules at metal surfaces: bonding, organisation and chirality". In: *Surf. Sci. Rep.* 50.6 (2003), pp. 201–341.

[104] Takashi Yokoyama et al. "Selective assembly on a surface of supramolecular aggregates with controlled size and shape". In: *Nature* 413.6856 (2001), pp. 619–621.

[105] Pascal Ruffieux et al. "Site-and orientation-selective anchoring of a prototypical molecular building block". In: *J. Am. Chem. Soc.* 129.16 (2007), pp. 5007–5011.

[106] Harald Brune et al. "Self-organized growth of nanostructure arrays on strain-relief patterns". In: *Nature* 394.6692 (1998), pp. 451–453.

[107] Christoph Tegenkamp. "Vicinal surfaces for functional nanostructures". In: *J. Phys: Condens. Matter.* 21.1 (2008), p. 013002.

[108] J. Kröger et al. "Self-organization of cobalt-phthalocyanine on a vicinal gold surface revealed by scanning tunnelling microscopy". In: *Surf. Sci.* 601.18 (2007), pp. 4180 –4184.

[109] Yoji Kunihashi, Makoto Kohda, and Junsaku Nitta. "Enhancement of spin lifetime in gate-fitted InGaAs narrow wires". In: *Phys. Rev. Lett.* 102.22 (2009), p. 226601.

[110] Yusuke Tanaka et al. "Highly Ordered Cobalt–Phthalocyanine Chains on Fractional Atomic Steps: One-Dimensionality and Electron Hybridization". In: *ACS Nano* 7.2 (2012), pp. 1317–1323.

[111]   Karl M Kadish, Kevin M Smith, and Roger Guilard. *The Porphyrin Handbook: Inorganic, organometallic and coordination chemistry*. Vol. 3. Elsevier, 2000.

[112]   Neil B McKeown. *Phthalocyanine materials: synthesis, structure and function*. 6. Cambridge University Press, 1998.

[113]   Jianzhuang Jiang. *Functional phthalocyanine molecular materials*. Vol. 135. Springer, 2010.

[114]   Esther Barrena et al. "2D Supramolecular Self-Assembly of Binary Organic Monolayers". In: *Chem. Phys. Chem* 8.13 (2007), pp. 1915–1918.

[115]   Lizhi Zhang et al. "Site-and configuration-selective anchoring of iron–phthalocyanine on the step edges of Au (111) surface". In: *J. Phys. Chem. C* 115.21 (2011), pp. 10791–10796.

[116]   Aidi Zhao et al. "Kondo effect in single cobalt phthalocyanine molecules adsorbed on Au (111) monoatomic steps". In: *J. Chem. Phys.* 128.23 (2008), p. 234705.

[117]   Yongfeng Wang, Yingchun Ye, and Kai Wu. "Adsorption and assembly of copper phthalocyanine on cross-linked TiO2 (110)-(1× 2) and TiO2 (210)". In: *J. Phys. Chem. B* 110.36 (2006), pp. 17960–17965.

[118]   YH Jiang et al. "Self-assembly of metal phthalocyanines on Pb (111) and Au (111) surfaces at submonolayer coverage". In: *J. Phys. Chem. C* 115.44 (2011), pp. 21750–21754.

[119]   Dieter Worle, Gunter Meyer, and Bernd Wahl. "Polymere phthalocyanine und ihre vorstufen, 1. Reaktive oktafunktionelle phthalocyanine aus 1, 2, 4, 5-tetracyanbenzol". In: *Makromol. Chem.* 181.10 (1980), pp. 2127–2135.

[120]   JV Barth et al. "Scanning tunneling microscopy observations on the reconstructed Au (111) surface: Atomic structure, long-range superstructure, rotational domains, and surface defects". In: *Phys. Rev. B* 42.15 (1990), p. 9307.

[121]   Lander Verstraete et al. "Self-assembly under confinement: nanocorrals for understanding fundamentals of 2D crystallization". In: *ACS Nano* 10.12 (2016), pp. 10706–10715.

[122]   Marta E Canas Ventura et al. "Self-Assembly of Periodic Bicomponent Wires and Ribbons". In: *Angew. Chem. Int. Ed.* 46.11 (2007), pp. 1814–1818.

[123]   PJ De Rege, Scott A Williams, and Michael J Therien. "Direct evaluation of electronic coupling mediated by hydrogen bonds: implications for biological electron transfer". In: *Science* 269.5229 (1995), pp. 1409–1413.

[124]   N Patra, P Kral, and HR Sadeghpour. "Nucleation and stabilization of carbon-rich structures in interstellar media". In: *The Astrophysical Journal* 785.1 (2014), p. 6.

[125]   Jason P Dworkin et al. "Self-assembling amphiphilic molecules: Synthesis in simulated interstellar precometary ices". In: *Proceedings of the National Academy of Sciences* 98.3 (2001), pp. 815–819.

[126]   Kyle L Naughton et al. "Self-Assembly of the Cephalopod Protein Reflectin". In: *Advanced materials* 28.38 (2016), pp. 8405–8412.

[127]   Antti-Pekka Hynninen et al. "Self-assembly route for photonic crystals with a bandgap in the visible region". In: *Nature materials* 6.3 (2007), p. 202.

[128]   Rachel C Evans. "Harnessing self-assembly strategies for the rational design of conjugated polymer based materials". In: *Journal of Materials Chemistry C* 1.27 (2013), pp. 4190–4200.

[129]   Jonathan Yeow, Odilia R Sugita, and Cyrille Boyer. "Visible light-mediated polymerization-induced self-assembly in the absence of external catalyst or initiator". In: *ACS Macro Letters* 5.5 (2016), pp. 558–564.

[130]   Aparna Deshpande et al. "Self-assembly and photopolymerization of sub-2 nm one-dimensional organic nanostructures on graphene". In: *Journal of the American Chemical Society* 134.40 (2012), pp. 16759–16764.

[131]   Jinyi Lin et al. "A π-conjugated polymer gelator from polyfluorene-based poly (tertiary alcohol) via the hydrogen-bonded supramolecular functionalization". In: *Polymer Chemistry* 4.3 (2013), pp. 477–483.

[132]   Jin-Yi Lin et al. "Understanding the molecular gelation processes of heteroatomic conjugated polymers for stable blue polymer light-emitting diodes". In: *Journal of Materials Chemistry C* 5.27 (2017), pp. 6762–6770.

[133]   Mengna Yu et al. "One-step preparation of conjugated homopolymer submicrospheres via a controllable supramolecular approach toward optoelectronic applications". In: *RSC Advances* 7.24 (2017), pp. 14688–14693.

[134]   Jin-Yi Lin et al. "Hydrogen-Bonded Supramolecular Conjugated Polymer Nanoparticles for White Light-Emitting Devices". In: *Macromolecular rapid communications* 35.9 (2014), pp. 895–900.

[135]   Kunal S Mali et al. "Frontiers of supramolecular chemistry at solid surfaces". In: *Chemical Society Reviews* 46.9 (2017), pp. 2520–2542.

[136] Maria-Eleni Ragoussi et al. "Carboxyethynyl Anchoring Ligands: A Means to Improving the Efficiency of Phthalocyanine-Sensitized Solar Cells". In: *Angewandte Chemie International Edition* 51.18 (2012), pp. 4375–4378.

[137] Paola Alippi et al. "A Ru–Ru pair housed in ruthenium phthalocyanine: the role of a "cage" architecture in the molecule coupling with the Ag (111) surface". In: *Physical Chemistry Chemical Physics* 19.2 (2017), pp. 1449–1457.

[138] Jianzhuang Jiang. *Functional phthalocyanine molecular materials*. Vol. 135. Springer, 2010.

[139] Zhenan Bao, Andrew J Lovinger, and Janelle Brown. "New air-stable n-channel organic thin film transistors". In: *Journal of the American Chemical Society* 120.1 (1998), pp. 207–208.

[140] Esther Barrena et al. "2D Supramolecular Self-Assembly of Binary Organic Monolayers". In: *ChemPhysChem* 8.13 (2007), pp. 1915–1918.

[141] Francesco Babudri et al. "Fluorinated organic materials for electronic and optoelectronic applications: the role of the fluorine atom". In: *Chemical Communications* 10 (2007), pp. 1003–1022.

[142] H Brinkmann et al. "Fluorinated phthalocyanines as molecular semiconductor thin films". In: *physica status solidi (a)* 205.3 (2008), pp. 409–420.

[143] Takashi Yokoyama et al. "Selective assembly on a surface of supramolecular aggregates with controlled size and shape". In: *Nature* 413.6856 (2001), p. 619.

[144] Kathrin Müller et al. "Cyano-Functionalized Triarylamines on Coinage Metal Surfaces: Interplay of Intermolecular and Molecule–Substrate Interactions". In: *Chemistry–A European Journal* 22.2 (2016), pp. 581–589.

[145] Dimas G de Oteyza et al. "Balancing intermolecular and molecule–substrate interactions in supramolecular assemblies". In: *Advanced Functional Materials* 19.2 (2009), pp. 259–264.

[146] KW Hipps et al. "A self-organized 2-dimensional bifunctional structure formed by supramolecular design". In: *Journal of the American Chemical Society* 124.10 (2002), pp. 2126–2127.

[147] Christian Wäckerlin et al. "Two-Dimensional Supramolecular Electron Spin Arrays". In: *Advanced materials* 25.17 (2013), pp. 2404–2408.

[148] Avijit Kumar, Kaustuv Banerjee, and Peter Liljeroth. "Molecular assembly on two-dimensional materials". In: *Nanotechnology* 28.8 (2017), p. 082001.

[149]   Karl-Heinz Ernst. "Molecular chirality at surfaces". In: *physica status solidi (b)* 249.11 (2012), pp. 2057–2088.

[150]   R Raval. "Chiral expression from molecular assemblies at metal surfaces: insights from surface science techniques". In: *Chemical Society Reviews* 38.3 (2009), pp. 707–721.

[151]   GP Lopinski et al. "Determination of the absolute chirality of individual adsorbed molecules using the scanning tunnelling microscope". In: *Nature* 392.6679 (1998), p. 909.

[152]   M Ortega Lorenzo et al. "Extended surface chirality from supramolecular assemblies of adsorbed chiral molecules". In: *Nature* 404.6776 (2000), p. 376.

[153]   Fabrice Charra and Jacques Cousty. "Surface-induced chirality in a self-assembled monolayer of discotic liquid crystal". In: *Physical review letters* 80.8 (1998), p. 1682.

[154]   Melissa L Liriano et al. "The interplay of covalency, hydrogen bonding, and dispersion leads to a long range chiral network: The example of 2-butanol". In: *The Journal of chemical physics* 144.9 (2016), p. 094703.

[155]   Matthias Böhringer et al. "Two-dimensional self-assembly of supramolecular clusters and chains". In: *Physical Review Letters* 83.2 (1999), p. 324.

[156]   J Weckesser et al. "Mesoscopic correlation of supramolecular chirality in one-dimensional hydrogen-bonded assemblies". In: *Physical Review Letters* 87.9 (2001), p. 096101.

[157]   Sigrid Weigelt et al. "Chiral switching by spontaneous conformational change in adsorbed organic molecules". In: *Nature materials* 5.2 (2006), p. 112.

[158]   NA Booth et al. "Determination of the local structure of glycine adsorbed on Cu (110)". In: *Surface science* 397.1-3 (1998), pp. 258–269.

[159]   Aitor Mugarza et al. "Orbital specific chirality and homochiral self-assembly of achiral molecules induced by charge transfer and spontaneous symmetry breaking". In: *Physical review letters* 105.11 (2010), p. 115702.

[160]   Feng Chen et al. "Chiral recognition of zinc phthalocyanine on Cu (100) surface". In: *Applied Physics Letters* 100.8 (2012), p. 081602.

[161]   April D Jewell et al. "Effect of Head-Group Chemistry on Surface-Mediated Molecular Self-Assembly". In: *Chemistry–A European Journal* 18.23 (2012), pp. 7169–7178.

[162]   Mathieu Abel et al. "Designing a New Two-Dimensional Molecular Layout by Hydrogen Bonding". In: *ChemPhysChem* 7.1 (2006), pp. 82–85.

[163] Darin O Bellisario et al. "Adsorption, assembly, and dynamics of dibutyl sulfide on Au {111}". In: *The Journal of Physical Chemistry C* 114.34 (2010), pp. 14583–14589.

[164] Stefano Gottardi et al. "Cyano-Functionalized Triarylamines on Au (111): Competing Intermolecular versus Molecule/Substrate Interactions". In: *Advanced Materials Interfaces* 1.1 (2014), p. 1300025.

[165] Paivi Jarvinen et al. "Self-assembly and orbital imaging of metal phthalocyanines on a graphene model surface". In: *The Journal of Physical Chemistry C* 118.24 (2014), pp. 13320–13325.

[166] OI Arillo-Flores et al. "Magnetic, electronic, and vibrational properties of metal and fluorinated metal phthalocyanines". In: *Physical Review B* 87.16 (2013), p. 165115.

[167] Ronald Hesper, LH Tjeng, and GA Sawatzky. "Strongly reduced band gap in a correlated insulator in close proximity to a metal". In: *EPL (Europhysics Letters)* 40.2 (1997), p. 177.

[168] KJ Franke et al. "Reducing the Molecule-Substrate Coupling in C 60-Based Nanostructures by Molecular Interactions". In: *Physical review letters* 100.3 (2008), p. 036807.

[169] W Chen et al. "Scanning tunneling microscopy observation of an electronic superlattice at the surface of clean gold". In: *Physical Review Letters* 80.7 (1998), p. 1469.

[170] Miguel Ruiz-Osés et al. "Non-Covalent Interactions in Supramolecular Assemblies Investigated with Electron Spectroscopies". In: *ChemPhysChem* 10.6 (2009), pp. 896–900.

[171] RFW Bader, W H_ Henneker, and Paul E Cade. "Molecular charge distributions and chemical binding". In: *The Journal of Chemical Physics* 46.9 (1967), pp. 3341–3363.

[172] Ju-Hyung Kim et al. "Seamless growth of a supramolecular carpet". In: *Nature communications* 7 (2016), p. 10653.

[173] M Zahid Hasan and Joel E Moore. "Three-dimensional topological insulators". In: *Annu. Rev. Condens. Matter Phys.* 2.1 (2011), pp. 55–78.

[174] Nevill F Mott. "The basis of the electron theory of metals, with special reference to the transition metals". In: *Proceedings of the Physical Society. Section A* 62.7 (1949), p. 416.

[175] Jan H de Boer and Evert JW Verwey. "Semi-conductors with partially and with completely filled 3d-lattice bands". In: *Proceedings of the Physical Society* 49.4S (1937), p. 59.

[176] Walter Kohn. "Theory of the insulating state". In: *Physical Review* 133.1A (1964), A171.

[177] Charles L. Kane and Eugene J. Mele. "A New Spin on the Insulating State". In: *Science* ().

[178] Joel E Moore. "The birth of topological insulators". In: *Nature* 464.7286 (2010), p. 194.

[179] B Andrei Bernevig, Taylor L Hughes, and Shou-Cheng Zhang. "Quantum spin Hall effect and topological phase transition in HgTe quantum wells". In: *Science* 314.5806 (2006), pp. 1757–1761.

[180] B Andrei Bernevig and Shou-Cheng Zhang. "Quantum spin Hall effect". In: *Physical review letters* 96.10 (2006), p. 106802.

[181] David Hsieh et al. "A topological Dirac insulator in a quantum spin Hall phase". In: *Nature* 452.7190 (2008), p. 970.

[182] Haijun Zhang et al. "Topological insulators in Bi 2 Se 3, Bi 2 Te 3 and Sb 2 Te 3 with a single Dirac cone on the surface". In: *Nature physics* 5.6 (2009), p. 438.

[183] David Hsieh et al. "Observation of time-reversal-protected single-Dirac-cone topological-insulator states in Bi 2 Te 3 and Sb 2 Te 3". In: *Physical review letters* 103.14 (2009), p. 146401.

[184] YL Chen et al. "Experimental realization of a three-dimensional topological insulator, Bi2Te3". In: *science* 325.5937 (2009), pp. 178–181.

[185] Pedram Roushan et al. "Topological surface states protected from backscattering by chiral spin texture". In: *Nature* 460.7259 (2009), p. 1106.

[186] Jacob Linder et al. "Unconventional superconductivity on a topological insulator". In: *Physical review letters* 104.6 (2010), p. 067001.

[187] Liang Fu and Charles L Kane. "Superconducting proximity effect and Majorana fermions at the surface of a topological insulator". In: *Physical review letters* 100.9 (2008), p. 096407.

[188] AA Burkov and DG Hawthorn. "Spin and charge transport on the surface of a topological insulator". In: *Physical review letters* 105.6 (2010), p. 066802.

[189] Yabin Fan et al. "Magnetization switching through giant spin–orbit torque in a magnetically doped topological insulator heterostructure". In: *Nature materials* 13.7 (2014), p. 699.

[190] Sankar Das Sarma, Michael Freedman, and Chetan Nayak. "Majorana zero modes and topological quantum computation". In: *npj Quantum Information* 1 (2015), p. 15001.

[191] Zhanybek Alpichshev et al. "STM imaging of impurity resonances on Bi 2 Se 3". In: *Physical review letters* 108.20 (2012), p. 206402.

[192] YL Chen et al. "Massive Dirac fermion on the surface of a magnetically doped topological insulator". In: *Science* 329.5992 (2010), pp. 659–662.

[193] Qin Liu et al. "Magnetic impurities on the surface of a topological insulator". In: *Physical review letters* 102.15 (2009), p. 156603.

[194] Mikhail M Otrokov, Evgueni V Chulkov, and Andrés Arnau. "Breaking time-reversal symmetry at the topological insulator surface by metal-organic coordination networks". In: *Physical Review B* 92.16 (2015), p. 165309.

[195] L Andrew Wray et al. "A topological insulator surface under strong Coulomb, magnetic and disorder perturbations". In: *Nature Physics* 7.1 (2011), pp. 32–37.

[196] Marco Bianchi et al. "Simultaneous quantization of bulk conduction and valence states through adsorption of nonmagnetic impurities on Bi 2 Se 3". In: *Physical review letters* 107.8 (2011), p. 086802.

[197] Mao Ye et al. "Quasiparticle interference on the surface of Bi 2 Se 3 induced by cobalt adatom in the absence of ferromagnetic ordering". In: *Physical Review B* 85.20 (2012), p. 205317.

[198] MR Scholz et al. "Tolerance of topological surface states towards magnetic moments: Fe on Bi 2 Se 3". In: *Physical review letters* 108.25 (2012), p. 256810.

[199] T Schlenk et al. "Controllable magnetic doping of the surface state of a topological insulator". In: *Physical review letters* 110.12 (2013), p. 126804.

[200] Jagadeesh S. Moodera, Bert Koopmans, and Peter M. Oppeneer. "On the path toward organic spintronics". In: *MRS Bulletin* 39.7 (2014), 578–581.

[201] Mirko Cinchetti. "Molecular spintronics: Topology communicates". In: *Nature nanotechnology* 9.12 (2014), p. 965.

[202] Nicolae Atodiresei et al. "Design of the local spin polarization at the organic-ferromagnetic interface". In: *Physical review letters* 105.6 (2010), p. 066601.

[203]   Christian G Claessens, Uwe Hahn, and Tomás Torres. "Phthalocyanines:
        From outstanding electronic properties to emerging applications". In: *The
        Chemical Record* 8.2 (2008), pp. 75–97.

[204]   Stefan Schmaus et al. "Giant magnetoresistance through a single molecule".
        In: *Nature nanotechnology* 6.3 (2011), p. 185.

[205]   A Atxabal et al. "Spin doping using transition metal phthalocyanine molecules".
        In: *Nature communications* 7 (2016), p. 13751.

[206]   Aitor Mugarza et al. "Spin coupling and relaxation inside molecule–metal
        contacts". In: *Nature communications* 2 (2011), p. 490.

[207]   Thomas Bathon et al. "Systematics of molecular self-assembled networks at
        topological insulators surfaces". In: *Nano letters* 15.4 (2015), pp. 2442–2447.

[208]   Paolo Sessi et al. "Probing the electronic properties of individual MnPc molecules
        coupled to topological states". In: *Nano letters* 14.9 (2014), pp. 5092–5096.

[209]   YR Song et al. "Magnetic anisotropy of van der Waals absorbed iron (II)
        phthalocyanine layer on Bi 2 Te 3". In: *Physical Review B* 90.18 (2014),
        p. 180408.

[210]   Marco Caputo et al. "Manipulating the topological interface by molecular
        adsorbates: adsorption of Co-phthalocyanine on Bi2Se3". In: *Nano letters*
        16.6 (2016), pp. 3409–3414.

[211]   Sebastian Jakobs et al. "Controlling the spin texture of topological insula-
        tors by rational design of organic molecules". In: *Nano letters* 15.9 (2015),
        pp. 6022–6029.

[212]   YY Zhang, SX Du, and H-J Gao. "Binding configuration, electronic struc-
        ture, and magnetic properties of metal phthalocyanines on a Au (111) sur-
        face studied with ab initio calculations". In: *Physical Review B* 84.12 (2011),
        p. 125446.

[213]   ZH Cheng et al. "Epitaxial growth of iron phthalocyanine at the initial stage
        on Au (111) surface". In: *The Journal of Physical Chemistry C* 111.6 (2007),
        pp. 2656–2660.

[214]   YH Jiang et al. "Self-assembly of metal phthalocyanines on Pb (111) and
        Au (111) surfaces at submonolayer coverage". In: *The Journal of Physical
        Chemistry C* 115.44 (2011), pp. 21750–21754.

[215]   F Sedona et al. "Tuning the catalytic activity of Ag (110)-supported Fe ph-
        thalocyanine in the oxygen reduction reaction". In: *Nature materials* 11.11
        (2012), p. 970.

[216] Shih-Hsin Chang et al. "Symmetry reduction of metal phthalocyanines on metals". In: *Phys. Rev. B* 78.23 (2008), p. 233409.

[217] Avijit Kumar, Kaustuv Banerjee, and Peter Liljeroth. "Molecular assembly on two-dimensional materials". In: *Nanotechnology* 28.8 (2017), p. 082001.

[218] Kai-Felix Braun and Saw-Wai Hla. "Probing the conformation of physisorbed molecules at the atomic scale using STM manipulation". In: *Nano letters* 5.1 (2005), pp. 73–76.

[219] Oleg V Yazyev et al. "Quasiparticle effects in the bulk and surface-state bands of Bi 2 Se 3 and Bi 2 Te 3 topological insulators". In: *Phys. Rev. B* 85.16 (2012), p. 161101.

[220] A Mugarza et al. "Electronic and magnetic properties of molecule-metal interfaces: Transition-metal phthalocyanines adsorbed on Ag (100)". In: *Phys. Rev. B* 85.15 (2012), p. 155437.

[221] Hai Wang et al. "Ultralong copper phthalocyanine nanowires with new crystal structure and broad optical absorption". In: *ACS nano* 4.7 (2010), pp. 3921–3926.

[222] Wei Wu, A. J. Fisher, and N. M. Harrison. "Theoretical modeling of the electronic structure and exchange interactions in a Cu(II)Pc one-dimensional chain". In: *Phys. Rev. B* 84 (2 2011), p. 024427.

[223] Rejaul Sk et al. "Effect of Cyano Substitution on the Step-Edge Adsorption of Copper Phthalocyanine on Au (111)". In: *The Journal of Physical Chemistry C* (2018).

[224] Juan YE et al. "Chiral Features of the Achiral Copper Phthalocyanine on a Bi(111) Surface". In: *Acta Physico-Chimica Sinica* 32.10, 2593 (2016), p. 2593.

[225] Yongfeng Wang et al. "Molecular nanocrystals on ultrathin NaCl films on Au (111)". In: *Journal of the American Chemical Society* 132.36 (2010), pp. 12546–12547.

[226] K Schönauer et al. "Charge transfer and symmetry reduction at the CuPc/Ag (110) interface studied by photoemission tomography". In: *Physical Review B* 94.20 (2016), p. 205144.

[227] H Karacuban et al. "Substrate-induced symmetry reduction of CuPc on Cu (1 1 1): an LT-STM study". In: *Surface Science* 603.5 (2009), pp. L39–L43.

[228]   Ramón Cuadrado et al. "CoPc adsorption on Cu (111): Origin of the C 4 to C
        2 symmetry reduction". In: *The Journal of chemical physics* 133.15 (2010),
        p. 154701.

[229]   Yi-Lin Wang et al. "Structural defects and electronic properties of the Cu-
        doped topological insulator Bi 2 Se 3". In: *Physical Review B* 84.7 (2011),
        p. 075335.

[230]   Rejaul Sk et al. "Enhancing Intermolecular Interaction by Cyano Substitution
        in Copper Phthalocyanine". In: *The Journal of Physical Chemistry C* 122.1
        (2018), pp. 429–437.

[231]   Yu Jie Zheng et al. "Heterointerface screening effects between organic mono-
        layers and monolayer transition metal dichalcogenides". In: *ACS nano* 10.2
        (2016), pp. 2476–2484.

[232]   Akitaka Hoshino, Yoshiko Takenaka, and Hideki Miyaji. "Redetermination
        of the crystal structure of α-copper phthalocyanine grown on KCl". In: *Acta
        Crystallographica Section B: Structural Science* 59.3 (2003), pp. 393–403.

[233]   Michele Serri et al. "High-temperature antiferromagnetism in molecular semi-
        conductor thin films and nanostructures". In: *Nature communications* 5 (2014),
        p. 3079.

[234]   Xi Chen et al. "Probing superexchange interaction in molecular magnets by
        spin-flip spectroscopy and microscopy". In: *Physical review letters* 101.19
        (2008), p. 197208.

[235]   Wei Wu, A. J. Fisher, and N. M. Harrison. "Theoretical modeling of the
        electronic structure and exchange interactions in a Cu(II)Pc one-dimensional
        chain". In: *Phys. Rev. B* 84 (2 2011), p. 024427.

[236]   LA Bumm et al. "Are single molecular wires conducting?" In: *Science* 271.5256
        (1996), pp. 1705–1707.

[237]   J Chen et al. "Large on-off ratios and negative differential resistance in a
        molecular electronic device". In: *science* 286.5444 (1999), pp. 1550–1552.

[238]   Robert F Service. "Breakthrough of the year. Molecules get wired." In: *Sci-
        ence (New York, NY)* 294.5551 (2001), p. 2442.

[239]   Leo Esaki. "Long journey into tunneling". In: *Science* 183.4130 (1974), pp. 1149–
        1155.

[240]   Marius Grundmann. *The physics of semiconductors: an introduction includ-
        ing nanophysics and applications*. Springer, 2015.

[241] In-Whan Lyo and Phaedon Avouris. "Negative differential resistance on the atomic scale: implications for atomic scale devices". In: *Science* 245.4924 (1989), pp. 1369–1371.

[242] P Bedrossian et al. "Demonstration of the tunnel-diode effect on an atomic scale". In: *Nature* 342.6247 (1989), p. 258.

[243] DDD Ma et al. "Negative differential resistance in scanning-tunneling spectroscopy of diamond films". In: *Applied physics letters* 80.7 (2002), pp. 1231–1233.

[244] Yongqiang Xue et al. "Negative differential resistance in the scanning-tunneling spectroscopy of organic molecules". In: *Physical Review B* 59.12 (1999), R7852.

[245] J Chen et al. "Room-temperature negative differential resistance in nanoscale molecular junctions". In: *Applied physics letters* 77.8 (2000), pp. 1224–1226.

[246] Changgan Zeng et al. "Negative differential-resistance device involving two C 60 molecules". In: *Applied Physics Letters* 77.22 (2000), pp. 3595–3597.

[247] Nathan P Guisinger et al. "Room temperature negative differential resistance through individual organic molecules on silicon surfaces". In: *Nano Letters* 4.1 (2004), pp. 55–59.

[248] Jin He and Stuart M Lindsay. "On the mechanism of negative differential resistance in ferrocenylundecanethiol self-assembled monolayers". In: *Journal of the American Chemical Society* 127.34 (2005), pp. 11932–11933.

[249] Steffen Rolf-Pissarczyk et al. "Dynamical negative differential resistance in antiferromagnetically coupled few-atom spin chains". In: *Physical review letters* 119.21 (2017), p. 217201.

[250] J Gaudioso, LJ Lauhon, and W Ho. "Vibrationally mediated negative differential resistance in a single molecule". In: *Physical review letters* 85.9 (2000), p. 1918.

[251] XW Tu, Gareguin Mikaelian, and Wilson Ho. "Controlling single-molecule negative differential resistance in a double-barrier tunnel junction". In: *Physical review letters* 100.12 (2008), p. 126807.

[252] M Grobis et al. "Tuning negative differential resistance in a molecular film". In: *Applied Physics Letters* 86.20 (2005), p. 204102.

[253] Lan Chen et al. "Mechanism for negative differential resistance in molecular electronic devices: local orbital symmetry matching". In: *Physical review letters* 99.14 (2007), p. 146803.

[254]   Weihua Wang et al. "Negative differential resistance in a hybrid silicon-molecular system: Resonance between the intrinsic surface-states and the molecular orbital". In: *ACS nano* 6.8 (2012), pp. 7066–7076.

[255]   Marius Toader et al. "Exploring the F16CoPc/Ag (110) interface using scanning tunneling microscopy and spectroscopy. Part 1: Template-guided ad-layer structure formation". In: *The Journal of Physical Chemistry C* 114.8 (2010), pp. 3537–3543.

[256]   Paivi Jarvinen et al. "Self-assembly and orbital imaging of metal phthalocyanines on a graphene model surface". In: *The Journal of Physical Chemistry C* 118.24 (2014), pp. 13320–13325.

[257]   Kelvin Hong Liang Zhang et al. "Control of two-dimensional ordering of F16CuPc on Bi/Ag (111): effect of interfacial interactions". In: *The Journal of Physical Chemistry C* 114.25 (2010), pp. 11234–11241.

[258]   Rejaul Sk, Imrankhan Mulani, and Aparna Deshpande. "Emergent Properties of Organic Molecule-Topological Insulator Hybrid Interface: Cu-Phthalocyanine on Bi2Se3". In: *The Journal of Physical Chemistry C* accepted (2018).

[259]   Titash Rakshit et al. "Silicon-based molecular electronics". In: *Nano Letters* 4.10 (2004), pp. 1803–1807.

[260]   Han Huang, Wei Chen, and Andrew Thye Shen Wee. "Low-temperature scanning tunneling microscopy investigation of epitaxial growth of F16CuPc thin films on Ag (111)". In: *The Journal of Physical Chemistry C* 112.38 (2008), pp. 14913–14918.

[261]   Yutaka Wakayama. "Assembly process and epitaxy of the F16CuPc monolayer on Cu (111)". In: *The Journal of Physical Chemistry C* 111.6 (2007), pp. 2675–2678.

[262]   Min-Long Tao et al. "Structural transitions in different monolayers of cobalt phthalocyanine film grown on Bi (1 1 1)". In: *Journal of Physics D: Applied Physics* 49.1 (2015), p. 015307.

[263]   Marius Toader et al. "Exploring the F16CoPc/Ag (110) interface using scanning tunneling microscopy and spectroscopy. Part 1: Template-guided ad-layer structure formation". In: *The Journal of Physical Chemistry C* 114.8 (2010), pp. 3537–3543.

[264]   Marius Toader et al. "Exploring the F16CoPc/Ag (110) interface using scanning tunneling microscopy and spectroscopy. 2. Adsorption-induced charge transfer effect". In: *The Journal of Physical Chemistry C* 114.49 (2010), pp. 21548–21554.

[265] JP Ibe et al. "On the electrochemical etching of tips for scanning tunneling microscopy". In: *Journal of Vacuum Science & Technology A: Vacuum, Surfaces, and Films* 8.4 (1990), pp. 3570–3575.

[266] ZJ Li et al. "Single crystal growth and transport properties of Cu-doped topological insulator Bi2Se3". In: *Physics Procedia* 36 (2012), pp. 638–643.